# REPORT DOCUMENTATION PAGE

*Form Approved*
*OMB No. 0704-0188*

The public reporting burden for this collection of information is estimated to average 1 hour per response, including the time for reviewing instructions, searching existing data sources, gathering and maintaining the data needed, and completing and reviewing the collection of information. Send comments regarding this burden estimate or any other aspect of this collection of information, including suggestions for reducing the burden, to Department of Defense, Washington Headquarters Services, Directorate for Information Operations and Reports (0704-0188), 1215 Jefferson Davis Highway, Suite 1204, Arlington, VA 22202-4302. Respondents should be aware that notwithstanding any other provision of law, no person shall be subject to any penalty for failing to comply with a collection of information if it does not display a currently valid OMB control number.
**PLEASE DO NOT RETURN YOUR FORM TO THE ABOVE ADDRESS.**

| 1. REPORT DATE *(DD-MM-YYYY)* | 2. REPORT TYPE | 3. DATES COVERED *(From - To)* |
|---|---|---|
| March 31, 2006 | Quarterly Report | 1 Jan. to 31 Mar. 2006 |

**4. TITLE AND SUBTITLE**
Advanced Wireless Integrated Navy Network (AWINN)

**5a. CONTRACT NUMBER**
N00014-05-1-0179

**5b. GRANT NUMBER**
N00014-05-1-0179

**5c. PROGRAM ELEMENT NUMBER**

**6. AUTHOR(S)**
Warren Stutzman and Rick Habayeb

**5d. PROJECT NUMBER**

**5e. TASK NUMBER**

**5f. WORK UNIT NUMBER**

**7. PERFORMING ORGANIZATION NAME(S) AND ADDRESS(ES)**
Virginia Polytechnic Institute and State University
Electrical and Computer Engineering Department
302 Whittemore Hall (0111)
Blacksburg, VA 24061

**8. PERFORMING ORGANIZATION REPORT NUMBER**
5

**9. SPONSORING/MONITORING AGENCY NAME(S) AND ADDRESS(ES)**
Office of Naval Research
ONR 313
875 N. Randolph St.
Arlington, VA 22203-1995

**10. SPONSOR/MONITOR'S ACRONYM(S)**

**11. SPONSOR/MONITOR'S REPORT NUMBER(S)**

**12. DISTRIBUTION/AVAILABILITY STATEMENT**
Approved for public release; distribution unlimited.

**13. SUPPLEMENTARY NOTES**
The views, opinions and/or findings contained in this report are those of the author(s) and should not be constructed as an official Department of the Navy position, policy or decision, unless so designated by other documentation.

**14. ABSTRACT**
Quarterly progress report No. 5 on AWINN hardware and software configurations of smart, wideband, multi-function antennas, secure configurable platform, close-in command and control for Sea Basing visualization of wireless technologies, Ad Hoc networks, network protocols, real-time resource allocation, Ultra Wideband (UWB) communications network and ranging sensors, cross layer optimization and network interoperability.

**15. SUBJECT TERMS**

| 16. SECURITY CLASSIFICATION OF: | | | 17. LIMITATION OF ABSTRACT | 18. NUMBER OF PAGES | 19a. NAME OF RESPONSIBLE PERSON |
|---|---|---|---|---|---|
| a. REPORT | b. ABSTRACT | c. THIS PAGE | | | Rick Habayeb |
| U | U | U | UL | | 19b. TELEPHONE NUMBER *(Include area code)* 540-231-4353 |



# *Advanced Wireless Integrated Navy Network – AWINN*

## *5th Quarterly Report*

## *Virginia Tech*

DISTRIBUTION STATEMENT A
Approved for Public Release
Distribution Unlimited

## *January 1,2006 – March 31, 2006*

## TABLE OF CONTENTS

**Executive Summary** ..... **1**

**1. TASK 1 Advanced Wireless Technologies** ..... **2**

1.1 Task 1.1 Advanced Antennas ..... 2

1.2 Task 1.2 Advanced Software Radio ..... 19

1.3 TASK 1.3 Collaborative and Secure Wireless Communications ..... 48

**2. TASK 2 Secure and Robust Networks** ..... **68**

2.1 Task 2.1 Ad Hoc Networks ..... 68

2.2 Task 2.2 Real-Time Resource Management, Communications, and Middleware ..... 77

2.3 Task 2.3 Network Interoperability and Quality of Service ..... 94

2.4 Task 2.4 Cross-Layer Optimization ..... 96

**3. TASK 3 Visualization of Wireless Technology and Ad Hoc Networks** ..... **116**

3.1 Overview ..... 116

3.2 Task Activities for the period ..... 116

3.3 Importance/Relevance ..... 119

3.4 Productivity ..... 119

**4. TASK 4 Testing and Demonstrations** ..... **122**

4.1 TIP #1 Distributed MIMO UWB sensor networks incorporating software radio ..... 122

4.2 TIP #2 Close-in UWB wireless application to Sea Basing ..... 126

4.3 TIP #3: Secure Ad Hoc Networks ..... 129

4.4 TIP #4 Integration of Close-in UWB wireless with ESM crane for Sea Basing applications ..... 132

**5. FINANCIAL REPORT** ..... **133**

## Executive Summary

The fifth quarterly report summarizes on the activities and productivity of the AWINN team at Virginia Tech. The report covers the following thrust areas:

Advanced Wireless Technology

Secure and Robust Networks

Visualization of Wireless Technology and Ad Hoc Networks

Technology Integration Projects

During this reporting period, the AWINN team continued to successfully develop advanced wireless, SDR, MANET protocols, UWB sensing and communication, and collaborative communications technologies. The positive interaction between the diverse AWINN technologies provides good insights into the integration and engineering of useful products. The Advanced Antennas group continued the development of antennas in support of the AWINN Tasks 1.2, 1.3, and 3. The group developed balun measuring methods for balanced wideband antennas. The SDR team focused on the development of prototype transceivers and algorithms to support UWB, MIMO communications, position location and ranging. The SDR initial algorithms have been developed and tested in a proof-of-concept laboratory environment. The results of UWB sensor show that ranging accuracy will be within few inches, and that position location by evaluating the multipath delay profile is possible. The algorithms will be modified to provide full 3-D ranging and positioning information. The team is ready to integrate the transceiver next quarter. Tests conducted by the group confirm that time-interleaved sampling of UWB pulses using off-the-shelf components is feasible. The Collaborative and Secure Communications team is developing a collaboration method for the wireless communications. The method focuses on how to make multiple independent transceivers work together to reinforce each other's signal. They are investigating methods for improving the communication link performance between a mobile base station and distributed mobile sensor network. The reconfigurable computers group developed a technique to enhance the processing speed of the SDR transceiver. The technique is based on creating data paths to handle high data rates using COTS FPGAs. The effort of the Cross-Layer Optimization group is focused on cross-layer design for UWB position location networks PoLoNet and collaborative radio networks. The Networking group is investigating various protocols for QoS, security, mobile routing, and cross-layer optimization. The team is integrating the routing and MAC (medium access control) protocols for ad hoc networks of multiple channel operations to support both IPv4 and IPv6. The Real-Time team is concentrating on the standard for the Distributed Real-Time Specification of Java (DRTSJ), the time utility function, and the implementation of distributed Thread Polling algorithm. The Visualization of Wireless Technology team is completing an investigation of UWB contact-less sensor for the close-in operations. Early results indicate that UWB sensor technology is compatible to the close-in environment. The Technology Integration Projects (TIP) is developing the integration of the various AWINN technologies. During this reporting period, the AWINN team formulated the Close-In Communications and Operations (CINCO) concept that supports various operational domains and briefed it to ONR on March 27, 2006.

# 1. TASK 1 Advanced Wireless Technologies

## 1.1 Task 1.1 Advanced Antennas

### *1.1.1 Overview*

Task Goal: This task investigates new antenna technologies that may be applicable to Navy missions and provide hardware for AWINN integration projects.

Organization: This task is managed by Director of Virginia Tech Antenna Group (VTAG) using the following personnel:

Bill Davis, Director
Warren Stutzman, Faculty
Randall Nealy, Engineer
Taeyoung Yang, GRA
Scott Bates, GRA
John Kim, GRA
Gaurav Joshi, GRA

Summary: This quarter progress continued in the development of antennas for Sea Basing applications and loading dock applications using UWB and small antennas. A prototype for a balun and feed network for the four-square element is progessing to make the antenna a more viable element in multi-element, planar arrays. Lastly, thoughts on modeling a ship propagation environment have been completed with techniques for measurement using UWB and issues on transient aspects of MIMO.

### *1.1.2 Task Activities for the Period*

Task objective: Investigate new antenna technologies applicable to Navy missions and provide hardware for AWINN integration projects.

Links to other tasks: Tasks 1.2, 1.3, 3, and 4

#### Subtask 1.1.2a Investigation of compact antennas for handheld and mobile terminals

Task objective: Design compact planar UWB antennas for various applications and systems.

Accomplishments during reporting period: This task develops antennas for use in handheld and mobile terminals that require compact size and robust performance for both fixed and portable systems. This task was on hold for this quarter.

Links to other tasks: This task supports Task 1.2 and Task 4

Schedule: This continued through December 2005. Some future work may still occur on this task, but not as a major effort.

Personnel: Taeyoung Yang, GRA

#### *Subtask 1.1.2b* Antenna Characterization – transient & wideband

Task objective: Provide antenna characterization methods in both frequency and time domain

Accomplishments during reporting period: This task is linked to Subtask 1.1.2a and c. This task was on hold for this quarter and the related work is reported in Subtask 1.1.2c.

Links to other tasks: This task supports Task 1.2 and Task 4

Schedule: This subtask is a major part of Task 1.1 in the spring and will continue in support of the other AWINN tasks with prototype antennas, both simulated and built.

Personnel: John Kim (GRA), Randall Nealy (Engineer), and W. Davis (PI)

## *Subtask 1.1.2c* UWB antennas in support of AWINN demonstrations, including UWB Sea-Basing technologies

Task objective: Develop antennas to support Ultra-wideband (UWB) high data rate links

### Directional Antenna for SDR Receiver

Introduction

An antenna is needed for a directional SDR receiver. The specifications for the antenna are listed in Table 1.1-1. The antenna will be mounted at a corner of cargo crate and this requirement was considered in the antenna construction to enable easy mounting to the corner.

**Table 1.1-1** Specifications of the Antenna Needed

| | |
|---|---|
| Size | Not a major constraint but an antenna dimension fitting inside a 6" x 6" x 6" is desired |
| Transmitted Pulse Width | Given a 500 ps pulse input, the transmitted pulse width should be 1000-1500ps, with minimal pulse dispersion or ringing |
| Gain | Not a major constraint |
| Weight | Not a concern |
| Absolute Frequency Range | 500 MHz – 4 GHz |

Antenna Candidates

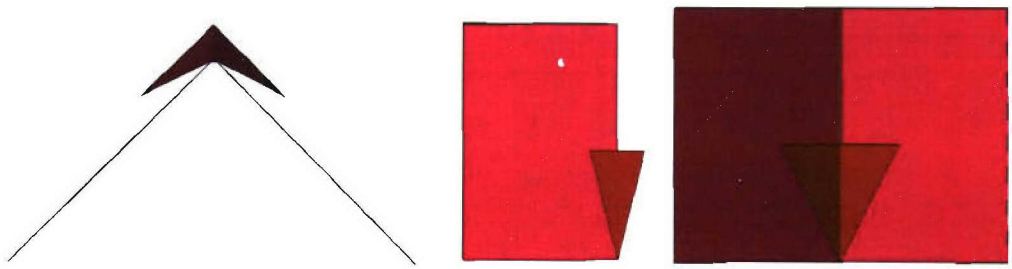
There are a couple of antennas that have been modified from their original design to fit the specifications. The two antennas suitable for UWB transmission are TEM horn and tapered slot antenna (TSA). Both were modified with a corner ground plane to be suitable for the application.

Simulation Results

Prior to constructing the antenna candidates, both were simulated using the commercial code FEKO to obtain the impedance, radiation pattern, and time domain response. The results for each antenna are presented.

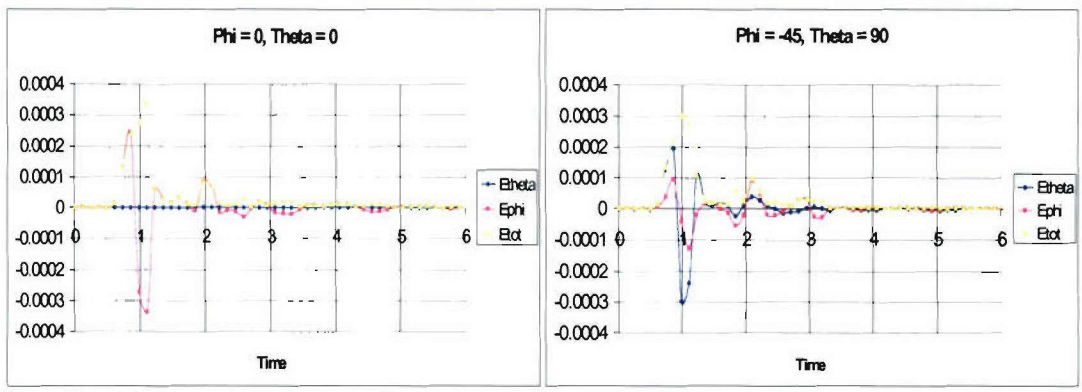
Half TEM Horn Placed Externally Over a Corner Reflector (HTEM)

A TEM horn shown in Fig. 1.1-1 has excellent UWB characteristics and a useful aperture for receiving signals. A half TEM horn over a flat ground plane shows good operating characteristics. However, for the application it is not directly suitable. Instead, the horn was folded around a corner reflector to keep a constant distance between the reflector and the horn.



a) Top View b) Side View c) Front View

**Figure 1.1-1** Half TEM horn over a corner reflector.



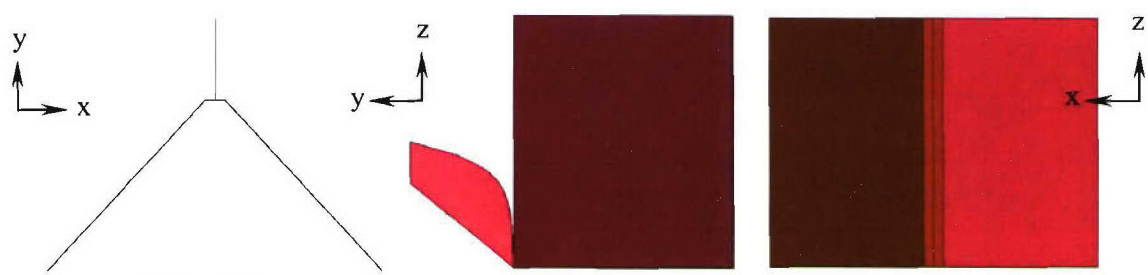

a) The Boresight Pulse Response b) Direct Link Antennas

**Figure 1.1-2** Time domain simulation result for the HTEM antenna.

The time domain simulation result for the HTEM is shown in Fig. 1.1-2. The time axis is a nanosecond scale. Both responses shows ringing after the main pulse response that lasts longer than 1.5 ns so that this antenna is less than desirable for the requirement outlined. The time domain response shows a lot of ringing so it was excluded from the possible candidate.

## Half Tapered Slot Antenna Over a Corner Reflector (HTSA)

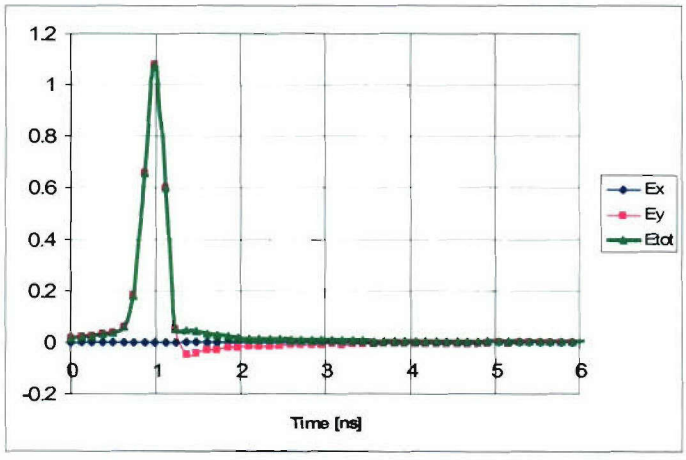
Another class of antennas that has excellent UWB characteristics is the tapered slot antenna (TSA) shown in Fgure 1.1-3. The same idea as the TEM horn is applied here, where half of a TSA antenna is placed over the corner reflector.



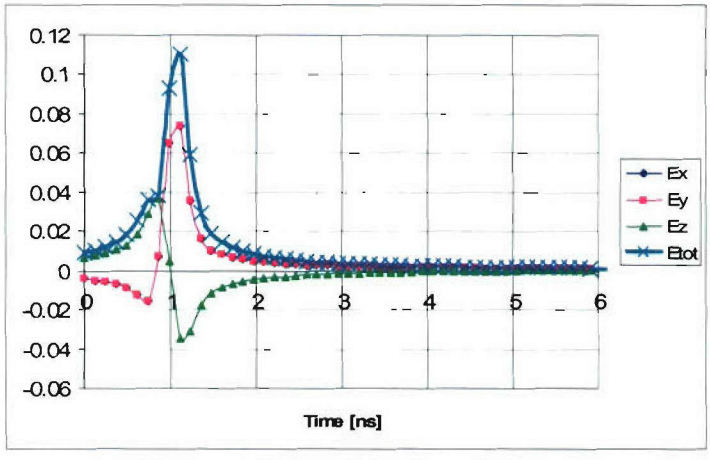

a) Top View b) Side View c) Front View

**Figure 1.1-3** Half TSA over a corner reflector.

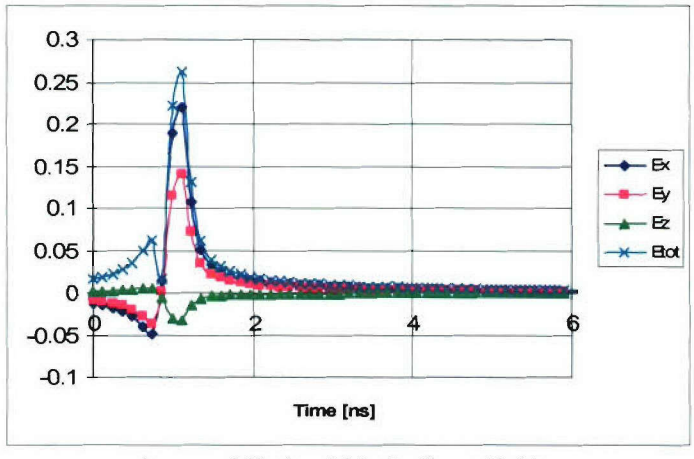
The time domain response results are very promising. The far-field pulse response for three different angles is shown in Fig. 1.1-4. As can be seen from the simulated far-field pulse responses, the produced pulses have a width less than 1.5 ns with very little ringing.




a) $\varphi = 0°$, $\theta = 0°$ (bore-sight)




b) $\varphi = -45°$, $\theta = 90°$ (direct link)



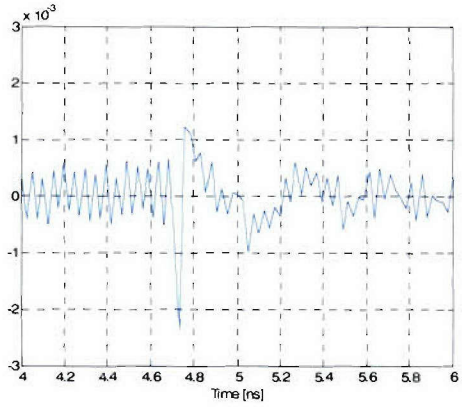

c) $\varphi = -45°$, $\theta = 30°$ (indirect link)

**Figure 1.1-4** Pulse responses at three different angles for the HTSA antenna.

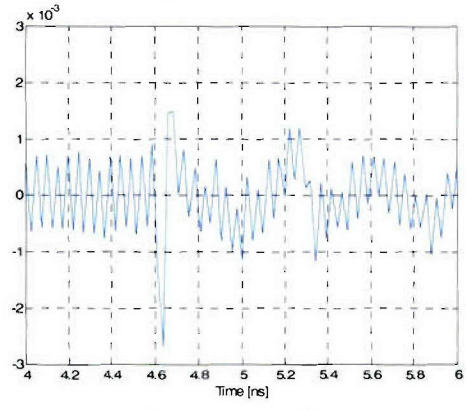
## Antenna Fabrication and Measurement

Three test antennas were made out of 16 mil thick brass sheets with SMA connector for connection with SDR receiver. The results are shown in Fig. 1.1-5. The reflection from ground

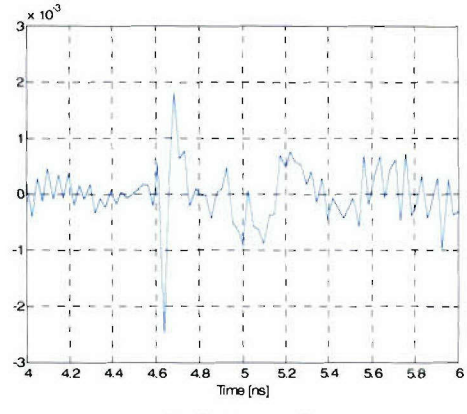
on bore sight was tested. The distance from the antenna to floor was around 70 cm so the return pulse is expected to be present at 4.6 ns.




a) Antenna 1




b) Antenna 2




c) Antenna 3

**Figure 1.1-5** Pulse response of three identically constructed half-TSA antennas.

The three half-TSA antennas were adjusted for a fixed separation from a ground plane and show distinct pulses at 4.7 ns corresponding to this separation. A transmission test between two antennas to observe reflection from the ground and direct transmission between the antennas remains to be done.

Links to other tasks: This task supports Tasks 1.2, 1.3, and 4

Schedule: This subtask is a major part of Task 1.1 in the spring and will continue in support of the other AWINN tasks with prototype antennas, both simulated and built.

Personnel: John Kim (GRA), Randall Nealy (Engineer), and W. Davis (PI)

*Subtask 1.1.2d* Antennas providing polarization, spatial, and pattern diversity – Evaluation of antennas in a MIMO environment

Task objective: Base station/access point antennas providing polarization, spatial and pattern diversity useful in supporting MIMO and space-time coding processing. Evaluation of antennas in a MIMO environment.

Accomplishments during reporting period: In continuation with the ongoing emphasis on the characterization of wideband propagation environment on the topside/upper-deck of a warship or destroyer, this month's efforts focused on the ultra-wideband (UWB) pulse measurements in an indoor environment. The first of the three scenarios evaluated for ultra-wideband communication over short distances, namely Line-of-Sight in a hallway was reported in the previous correspondence.

## Multiple-Input Multiple-Output (MIMO) UWB Measurement Setup

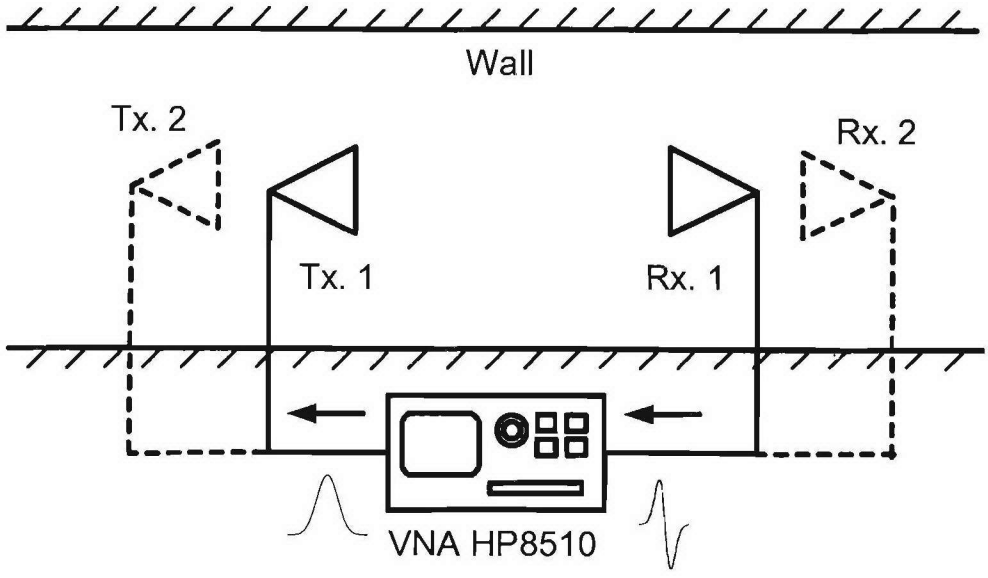
This section discusses the capacity of a UWB multiple-input multiple-output (MIMO) channel capacity based on experimental results. The UWB MIMO channel capacity is calculated for two indoor hallway scenarios: (a) line-of-sight (LOS) hallway environment, and (b) obstructed non-line-of-sight (NLOS) around a hallway corner environment.

The UWB-MIMO measurement setup for LOS condition is shown in Fig. 1.1-6(a). Fig. 1.1-6(b) shows the UWB-MIMO measurement setup for obstructed NLOS channel condition. Ultra-wideband multiple-input multiple-output (UWB-MIMO) pulse measurements were conducted in a controlled hallway environment in line-of-sight and obstructed channel conditions. The UWB pulse is a Gaussian pulse corresponding to a frequency range of 1 GHz – 13 GHz. The measurements were conducted using the vector network analyzer (VNA HP8510) inside a room with cables extending to the two planar TEM horn antennas in the hallway.

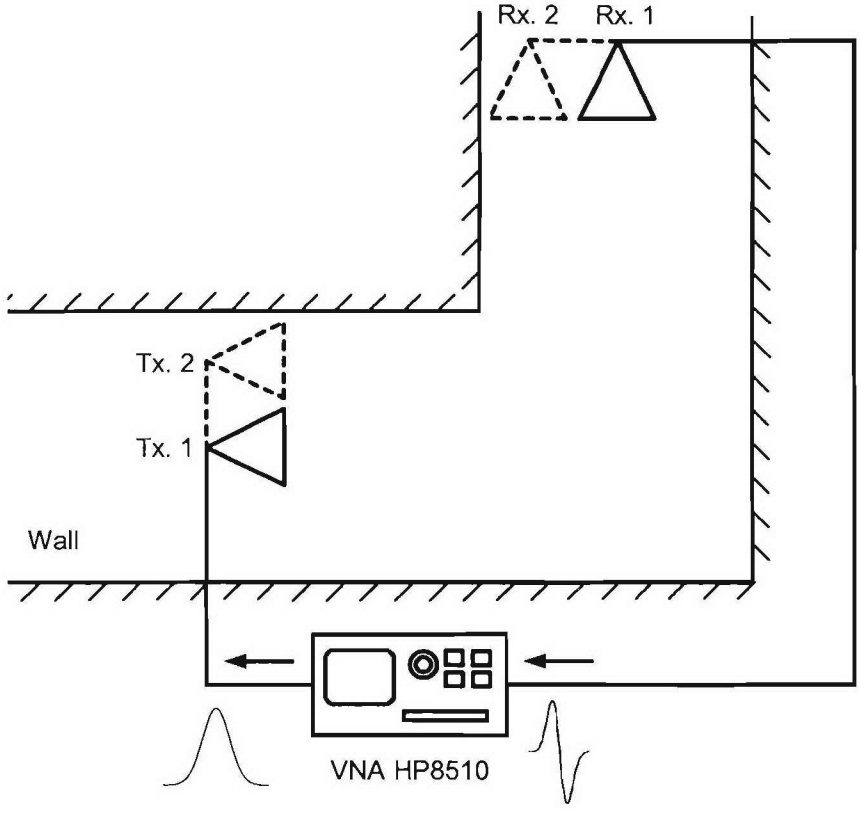
The experiment is calibrated with the response from a LOS link consisting of two planar TEM horn antennas mounted on pedestals at a height of 0.83 m and at a reference distance of 1 m, which is the separation of between the horn apertures. Four measurements corresponding to the permutation of two transmit and two receive antenna positions were recorded and post-processed as described in the next section.

## Multiple-Input Multiple-Output (MIMO) UWB Channel Analysis

Multiple-input multiple-output (MIMO) is a popular approach to improve data rate capacity using multiple antennas at the transmitter and the receiver. Achievable channel capacities are measured in terms of the number of bits transmitted per second over a unit bandwidth in bits/sec/Hz [1]. Under ideal conditions, a MIMO channel with $N$ number of transmit and receiver antennas increases the channel capacity over conventional single-input single-output (SISO) channels by a factor of $N$. Such large channel capacities are achieved when signal from each of the individual transmitter is received uncorrelated at each of the receiver. Environments rich with scatterers help achieve the true potential of a MIMO channel.




(a) Line-of-Sight (LOS) channel condition inside a hallway




(b) Non-line-of-sight (NLOS) obstructed channel condition around a corner inside a hallway

**Figure 1.1-6** Measurement setup using two planar TEM horn antennas mounted on pedestals at a height of 0.83 m. A single transmit antenna and a receive antenna is used to create a 2 x 2 MIMO channel with a separation of 0.3 m between the antenna positions numbered 1 and 2.

Channel capacities of flat faded (non-dispersive) narrowband applications have been widely reported in literature. However, no analytical expressions for channel capacity have been reported

for dispersive channel conditions. Ultra-wideband communications applications experience channel dispersion due to extremely large bandwidths in excess of 500 MHz and even as much as 7.5 GHz. Hence, channel capacity expressions developed for narrowband applications cannot be applied to UWB communications [2].

The complex base-band vector expression for the received signal in an $n_T$ x $n_R$ narrowband (non-dispersive) MIMO channel is given by

$$\begin{bmatrix} y_1 \\ y_2 \\ \vdots \\ y_{n_R} \end{bmatrix} = \begin{bmatrix} h_{11} & h_{12} & \cdots & h_{1n_T} \\ h_{21} & h_{22} & \cdots & h_{2n_T} \\ \vdots & \vdots & \ddots & \vdots \\ h_{n_R1} & h_{n_R2} & \cdots & h_{n_Rn_T} \end{bmatrix} \begin{bmatrix} x_1 \\ x_2 \\ \vdots \\ x_{n_T} \end{bmatrix} \tag{1.1-1}$$

where $x_j$ is the signal transmitted from the $j^{th}$ antenna, $y_i$ is the signal received at the $i^{th}$ antenna, and $h_{ij}$ is the complex channel gain between the $j^{th}$ transmitter and the $i^{th}$ receiver. The average capacity of a random Rayleigh faded SISO channel ($n_T = n_R = 1$) with an average transmit power constraint of $P_T$ is given by [3]

$$C = E\left\{ \log_2\left( 1+\frac{P_T}{\sigma_n^2}\left| h_{11} \right|^2 \right) \right\} \tag{1.1-2}$$

where E[•] is the expectation operator, $\sigma_n^2$ is the noise power spectral density of the receiver, and $| h_{11} |$ is random variable with a Rayleigh distribution. Avoiding the lengthy mathematical derivation, the average channel capacity of an AWGN MIMO channel with Rayleigh faded channels is given by [3]

$$C = E\left\{ \log_2\left( \det\left( I_{n_R} + \frac{P_T}{\sigma_n^2} H H^H \right) \right) \right\} \tag{1.1-3}$$

where $H$ is the channel matrix with elements as complex channel gains, and $\{\bullet\}^H$ indicates hermitian transpose.

The average channel capacity of a dispersive UWB MIMO channel is better appreciated in the z-domain due to simpler mathematical manipulations compared to the time-domain. The total MIMO system response in the z-domain is given by [4]

$$\bar{y}(z)_{n_R \times 1} = H(z)_{n_R \times n_T}\ \bar{x}(z)_{n_T \times 1} \tag{1.1-4}$$

A 2 x 2 UWB MIMO channel was measured in an indoor hallway environment with LOS and NLOS channel conditions as shown in Fig. 1.1-1. The UWB MIMO channel transfer function was measured in the frequency domain using a vector network analyzer (VNA-HP8510) and post processed to obtain $H(z)$. Hence, for a deterministic estimate of the channel capacity $C(z)$ at each frequency from 1 GHz to 13 GHz in steps of 50 MHz is given by

$$C(z) = \log_2\left( \det\left( I_{n_R} + \frac{P_T}{\sigma_n^2} H(z) H(z)^H \right) \right), \quad where\ z = e^{j\omega} \tag{1.1-5}$$

The channel capacity of a 2 x 2 UWB-MIMO channel in a LOS channel condition averaged over the frequency range of 1 GHz to 13 GHz is shown in Fig. 1.1-7. Note that the estimated channel capacities for individual UWB links is also shown for comparison. The trend shows that at low transmit power, the capacity of the 2 x 2 UWB MIMO link is only as good as the best of the four individual links. At higher transmit powers, the rate of improvement in channel capacity (given by the slope of the curve) is twice as that of the individual links.

The channel capacities of a single-input single-output (SISO) and a 2 x 2 Rayleigh faded MIMO channels are also shown for comparison. The Rayleigh fading indicates worst-case fading and hence, it presents a lower bound on the achievable channel capacity. The channel capacity of a SISO Rayleigh faded channel is given by (1.1-2) and that of a 2 x 2 MIMO Rayleigh faded channel is given by (1.1-3) with ($n_T = n_R = 2$).

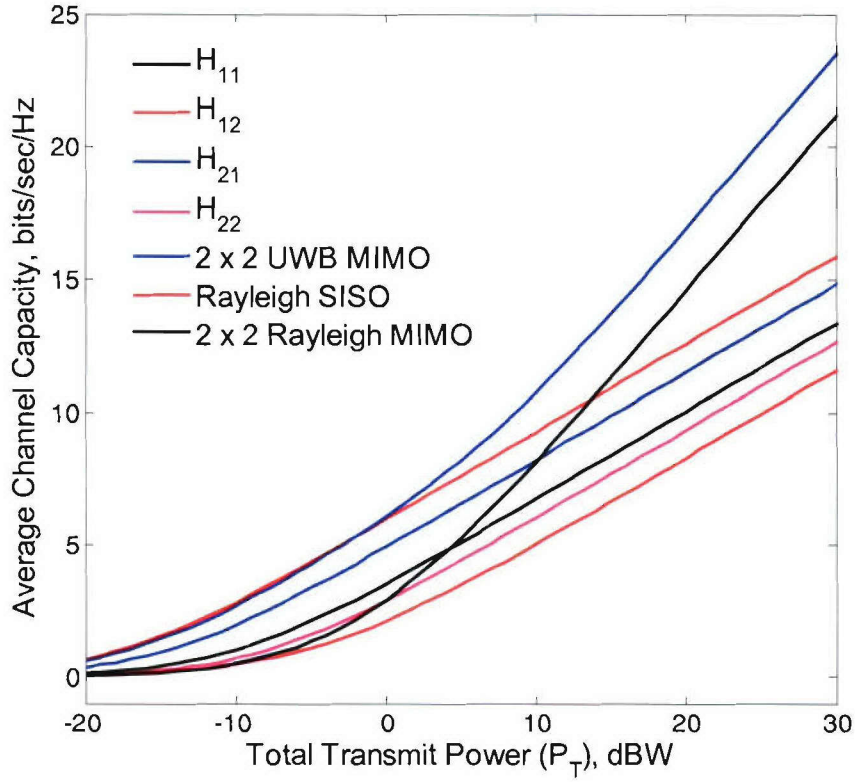



**Figure 1.1-7** The channel capacities of individually measured UWB links and a 2 x 2 UWB-MIMO channel calculated using (1.1-5) and averaged over a frequency range of 1 GHz to 13 GHz. The channel capacities of a SISO Rayleigh faded channel given by (1.1-2) and of a 2 x 2 MIMO Rayleigh faded channel given by (1.1-3) are shown for comparison.

Similar channel capacity results obtained for a 2 x 2 UWB-MIMO channel in an obstructed NLOS channel conditions are shown in Fig. 1.1-8. Fig. 1.1-8 compares the channel capacities calculated using (1.1-5) for individually measured UWB channels as well as the UWB-MIMO channel for both the LOS and NLOS channel conditions. The channel capacity is averaged over the frequency range of 1 GHz to 13 GHz. As expected, the estimated channel capacities for individual UWB links in LOS condition is much higher compared to the NLOS channel condition. At low transmit powers, the capacity of the 2 x 2 UWB MIMO link for both LOS and NLOS channel conditions is only as good as the best of the respective four individual links. At higher transmit powers, the rate of improvement in channel capacity (given by the slope of the curve) is twice as that of the individual links.

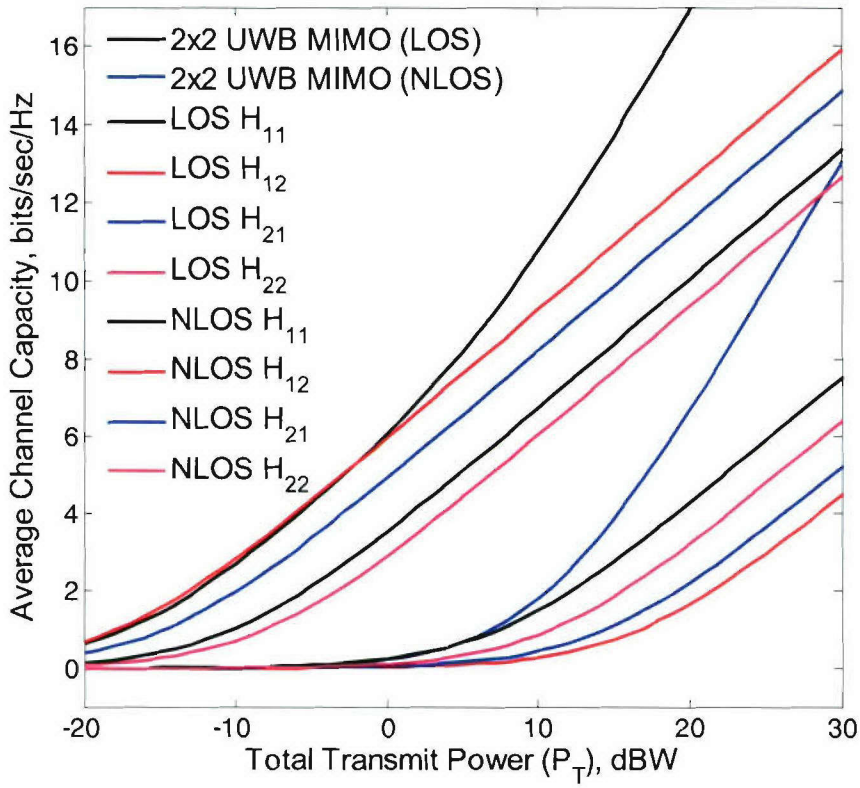



**Figure 1.1-8** The channel capacities calculated using (1.1-5) for individually measured UWB channels as well as the UWB-MIMO channel for both the LOS and NLOS channel conditions. The channel capacity is averaged over the frequency range of 1 GHz to 13 GHz.

References

[1] G. J. Foschini and M. J. Gans, "On limits of wireless communications in a fading environment when using multiple antennas," *Wireless Personal Communications*, vol. 6, pp. 311-335, 1998.

[2] S. Ray, M. Medard, and Z. Lizhong, "On MIMO capacity in the ultra-wideband regime," *Proceedings of the 38th Asilomar Conference on Signals, Systems and Computers*, vol. 2, pp. 1516-1520, Nov. 2004.

[3] B. Holter, "On the capacity of the MIMO channel - A tutorial introduction." Trondheim, Norway. 2001.

[4] K. Dietze, "Blind Identification of MIMO Systems: Signal Modulation and Channel Estimation," in *Bradley Dept. of Electrical and Computer Engineering*. Blacksburg, Ph.D: Virginia Polytechnic Institute and State University, 2005.

Links to other tasks: This topic may impact on the frequency selection and interaction of the measurements used for the Sea-Basing cargo systems being considered in Task 3.

Schedule: This was a major subtask in the Spring 2006.

Personnel: Gaurav Joshi

*Subtask 1.1.2e* Support physics/engineering-based models for Digital Ships

Task objective: Support of Task 3 to develop physics/engineering–based templates for Digital Ships for radar simulation, including EW techniques.

Accomplishments during reporting period: No requests are currently pending from Task 3 and no work was performed on this task.

Links to other tasks: In support of Task 3 on Digital Ships

Schedule: As requested by the personnel of Task 3. Some work may continue as it is felt to be useful to Task 3.

Personnel: Taeyoung Yang, GRA

*Subtask 1.1.2f* Wideband balanced antenna/array feed networks

Task objective: Development of array feed networks for wideband balanced antenna systems such as the Fourpoint antenna investigated in the NAVCIITI program

Accomplishments during reporting period: Since the last report the focus for the wideband antenna/array has been on several related tasks. One is the design of a balun network which also provides some degree of impedance transformation for a single four-square antenna element. The other task is the design, construction, and testing of a broadband balun, as well as the possessing of the impedance transformation characteristics for an impulse radiating antenna (IRA). Each task will be discussed below.

Balun Design for Four-Square Antenna

The four-square antenna is a versatile, broadband, planar antenna element which can be easily incorporated into an array configuration to facilitate beam steering. For this reason it was chosen as a good antenna for testing various balun and feed network designs. The present task is to incorporate a balun with a single four-square antenna element. Because the four-square input impedance is 100 Ω and signal feed lines are generally 50 Ω it is desired that this balun also provide an impedance transformation.

A suitable model for a four-square antenna was developed for simulation purposes. Two slightly different feed structures will be considered. A model which looks like that in Fig. 1.1-9 (a) below has been successfully simulated. The excitation of the antenna in Fig. 1.1-9(a) occurs at the location of the two opposite driven four-square elements. The two metal posts underneath the four-square element are meant to simulate the two coaxial feed lines in Fig. 1.1-9(b). The results for input impedance and VSWR match fairly well with results obtained from [1]. In the case of (a), the posts are shorted together. In case (b) the outer conductors of the two coaxial lines are shorted together. Fig. 1.1-9(c) shows an alternate feed structure consisting of parallel lines. In cases (b) and (c), the balun will be attached at the feed position underneath the ground plane.

Fig. 1.1-10 shows the simulated input impedance and VSWR for the case of Fig. 1.1-11(a). When the remaining two simulation configurations produce suitable results, comparison simulations will be run. In one simulation, the antenna will be excited using a single coaxial cable feed in an unbalanced configuration as in Fig. 1.1-11(b). A second simulation, with a configuration like that of Fig. 1.1-11 in which a balun is inserted between the feed and the antenna input was run. The pattern results are compared to determine the effectiveness of the balun.

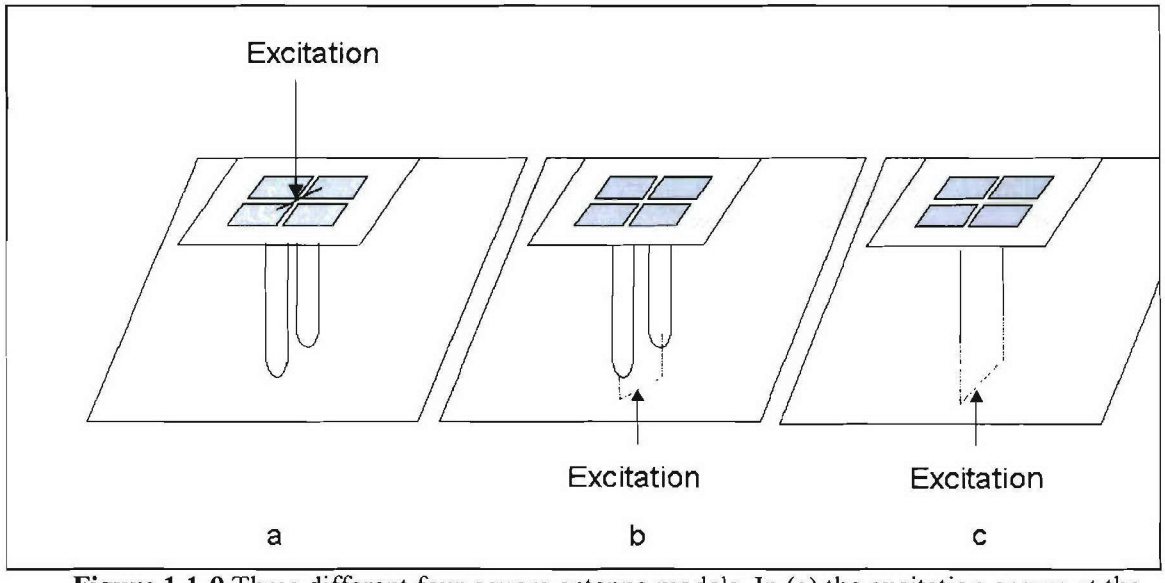



**Figure 1.1-9** Three different four-square antenna models. In (a) the excitation occurs at the two driven elements, in (b) the two coaxial feeds are modeled and excited below the ground plane, in (c) a pair of twin lines is excited below the ground plane.

Several balun geometries were considered for this task. Two of the designs in Fig 1.1-10(a) depicts a coplanar waveguide (CPW) input transitioning to a slot line (SL) structure [2]. Fig. 1.1-10(b) also has a CPW input which becomes coplanar strips (CPS) at the output. The CPW structure is unbalanced and can thus be fed with coaxial line. Both the CPW and CPS structures are well suited to feed the balanced input to the four-square antenna because they are themselves balanced.

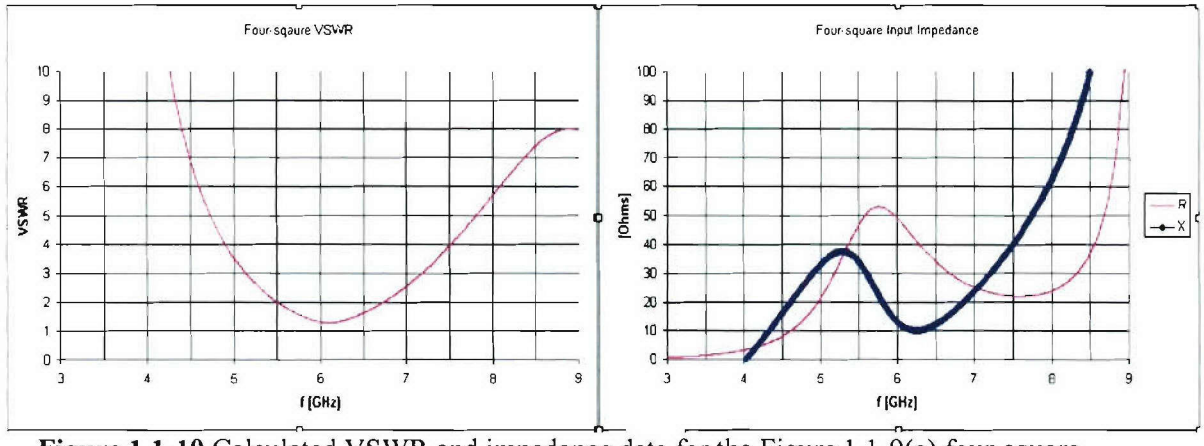



**Figure 1.1-10** Calculated VSWR and impedance data for the Figure 1.1-9(a) four-square geometry, for a 50-Ω reference.

A simple MatLab code was written to calculate the transmission line impedances of the types mentioned above. The equations were found in [3]. These two balun designs have unfortunately not yielded usable results. The dimensions of the CPW structure for a 50-Ω input impedance is prohibitively small. Various techniques were tried to overcome this problem including using high dielectric substrate ($\varepsilon_r$ = 10.8) and a thicker substrate. Unfortunately no method allowed for a workable dimension.

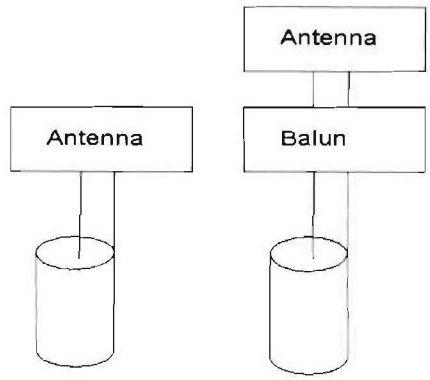



**Figure 1.1-11** (a) depicts an unbalanced feed to the four-sqaure antenna. (b) shows a balanced feed.

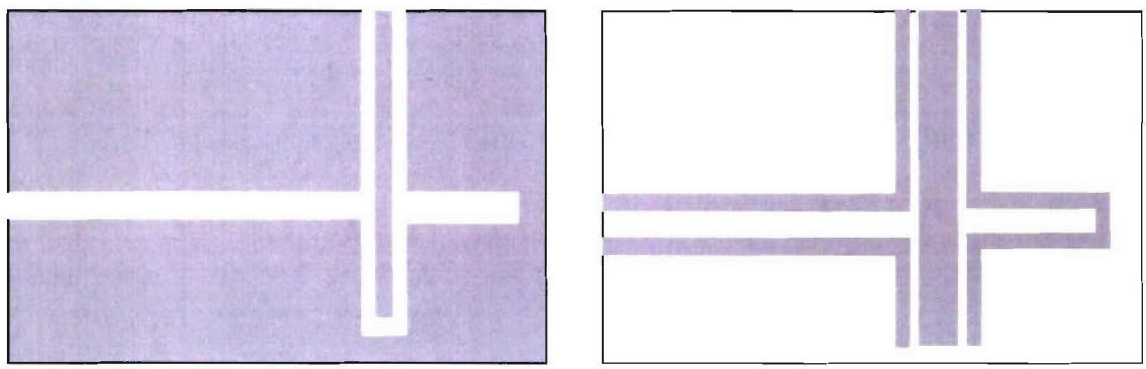



**Figure 1.1-12** Images of the cpw and cps baluns. From [2].

The balun design is now focused on using a 180° hybrid instead of one of the balun types mentioned above. Specifically a rat-race hybrid is in the design and simulation stages. If the bandwidth of this hybrid proves to not be wide enough, a tapered coupled-line hybrid design will investigated. Once we are able to show that the proposed 180° hybrid can provide a balanced feed to the input of the single four-square element a feed network, which will incorporate the needed balun structures, a small, square array of four-square antennas will be developed and simulated.

Broad band balun and balun measurements

The first iteration of a broad band balun, which will be used as the feed network for an IRA, was built and measured. It is intended to provide both a balanced output to the IRA as well as an impedance match. The desired impedance transformation is from 50 Ω unbalanced to 200 Ω balanced. The construction is copper tape over FR4 printed circuit board. The dimensions are given in Fig. 1.1-13.

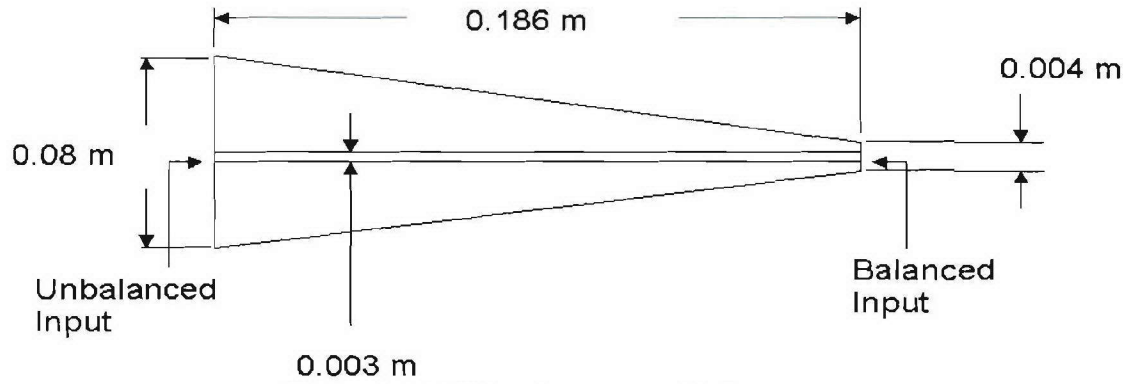



**Figure 1.1-13** Triangluar tappered balun.

It is important to be able to determine the level of balance provided by any balun. The classical method of determining the balance provided by a particular balun is to measure an antenna both with and without the device. If the balun is effective, the antenna pattern should be close to the theoretical shape of the pattern. At the very least, in general, the pattern with the balun present should be synnetric if the balun is working correctly, assuming the pattern should be symmetric.

Though the above method will work, it is desired to have a method for measuring the efficiency of a balun that does not involve measuring an antenna pattern. Because the output side of the balun is balanced it cannot be measured directly with a network analyzer because both the feed cables from the analyzer are unbalanced. There exist several alternate techniques for measurement that can be employed to determine the extent to which a balun is working correctly.

Fig. 1.1-14 depicts the two methods. Fig. 1.1-14(a) demonstrates the conversion of the balun from a two port to a three port device. Each leg of the balanced output port is connected to a short length of coaxial cable with the outer conductor of each cable shorted together. The amount of balance can be determined by looking at the magnitudes and phases of $S_{21}$ and $S_{31}$. For balance, we expect $|S_{21}| = |S_{31}|$ and $|\theta_{31} - \theta_{21}| = 180^\circ$.

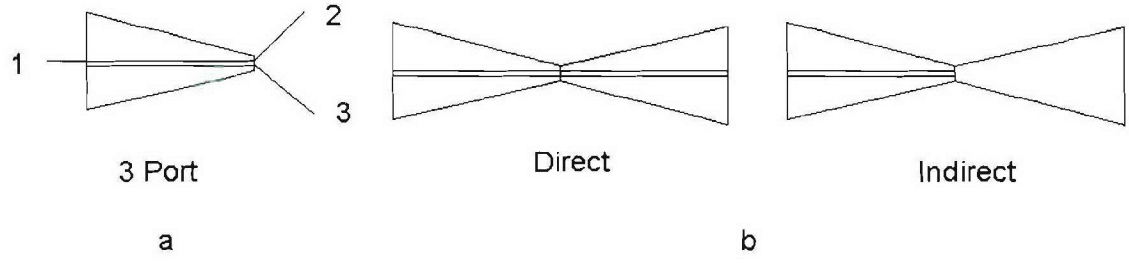



**Figure 1.1-14** Testing methods for the tapered balun. (a) depicts the three port method of verification of balance while (b) shows the direct and indirect method.

Another standard method for measuring balance is to connect two baluns under test together as in the "Direct" arrangement of Fig. 1.1-14(b). This method requires that two baluns be arranged such that the balanced output of one feeds directly into the balanced output of another balun of the same design. This configuration presents two unbalanced ports to connect to the two unbalanced ports of a network analyzer. This is generally referred to as a back-to-back measurement. We believe that by using this back-to-back data in conjunction with an indirect back-to-back measurement a more thorough assessment of balance can be obtained. Fig. 1.1-

14(b) "Indirect" depicts the indirect back-to-back geometry. In this case the balun on the right has been flipped along its horizontal axis and the ground side is facing outwards.

Data for the two port to three port measurement method is pictured below in Fig. 1.1-15 for the tapered balun design pictured above. Note that the magnitudes of $S_{21}$ and $S_{31}$ are fairly close over the frequency range. It appears to have a fairly good balance over the frequency range 0.5 GHz to 20 GHz. Note that it is also fairly lossy. This is due to the fact that the baluns were built using FR4 printed circuit board which is quite lossy above 1 GHz. Fig. 1.1-16 shows the phase difference between $S_{21}$ and $S_{31}$. They appear to be out of phase by either $-180^{\circ}$ or $180^{\circ}$ as desired. Fig. 1.1-17 shows a picture of the baluns that were measured.

A second iteration balun design will be constructed using a material with much better loss tangent and will be constructed by etching rather than applying copper tape. A model is now being developed so that the direct-indirect balance verification method can also be tested in simulation.

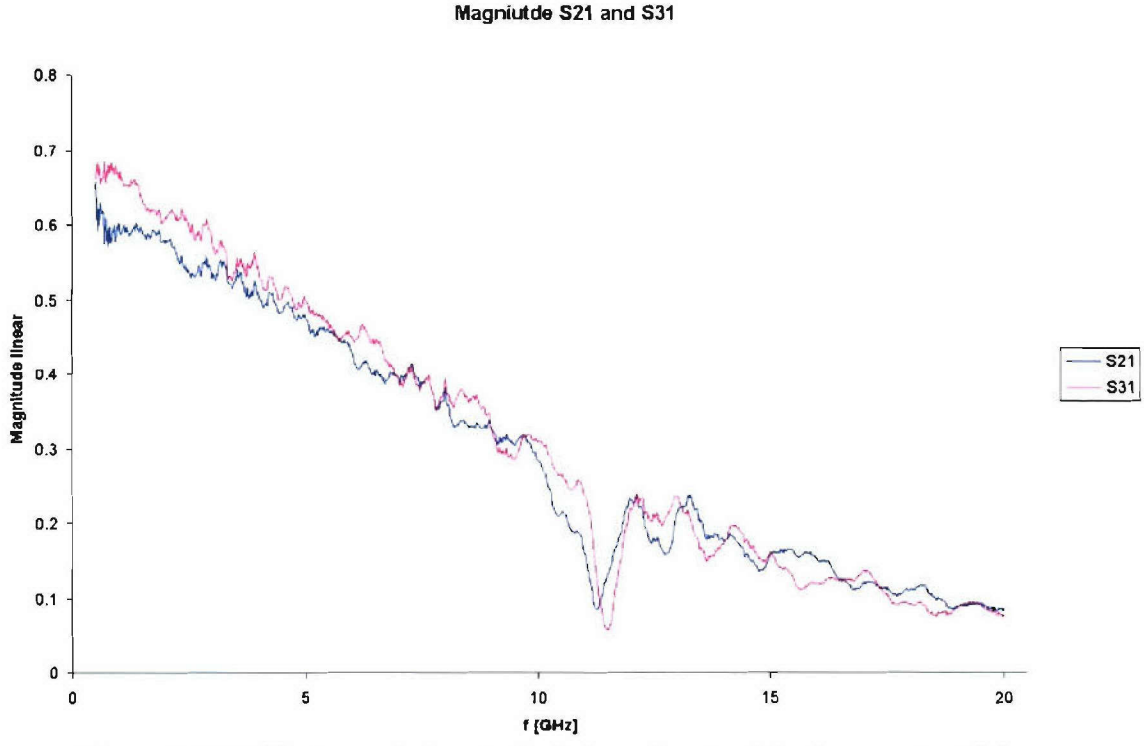



**Figure 1.1-15** The transmissions to the balanced ports of the three-port model, demonstrating the symmetry of the balun design.

Goals for the next quarter

There are several goals for the next quarter. The first is to finish the simulations models for the two different cases of feed networks (dual coaxial cable and parallel lines) for the single four-square antenna. The geometries with an unbalanced feed and with a 180 deg hybrid will be simulated. Once this is accomplished we will begin to investigate the geometry of four-square array antennas considering possible feed topologies, including matching, balancing, and phasing networks. Also, we will complete a better design of the tapered balun, and further develop and test the direct/indirect method for balun verification.

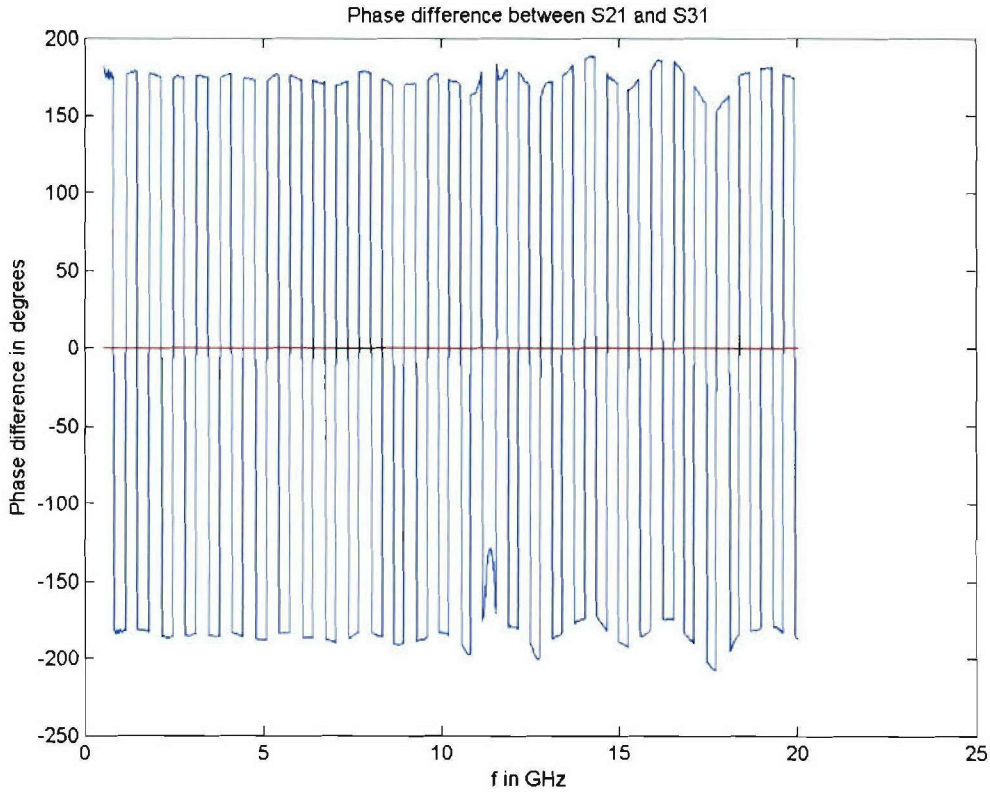



**Figure 1.1-16** Phase of the measured back-to-back system with a flip.

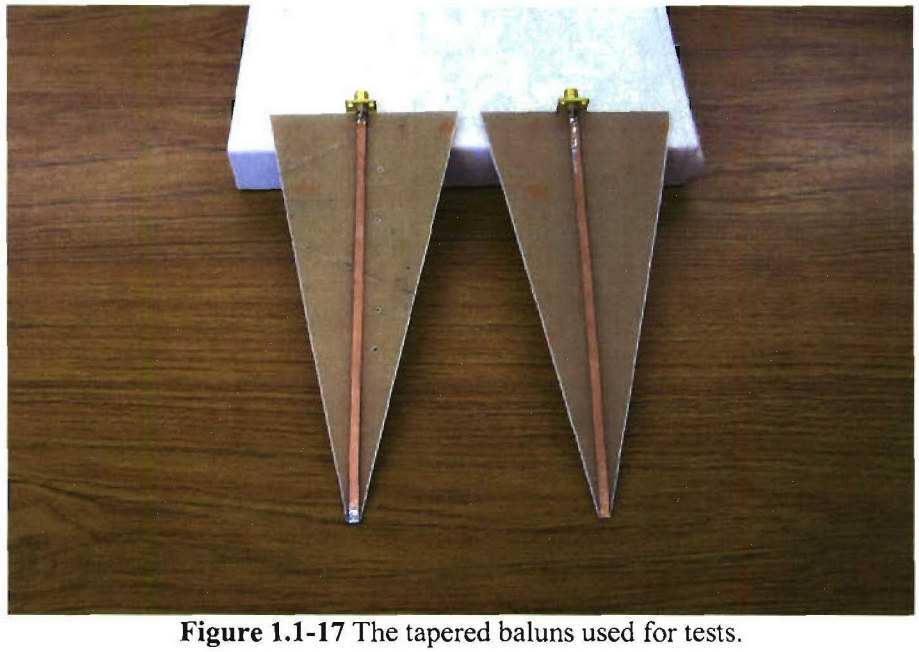


**Figure 1.1-17** The tapered baluns used for tests.

References


1. Seong-Youp Suh, "A Comprehensive Investigation of New Planar Wideband Antennas", Ph.D dissertation, July 29, 2002, Virginia Polytecnic Institute and State Univeristy, Blacksburg VA
2. Velimir Trifunovic and Branka Jokanovic, "Review of Printed Marchand and Double Y Baluns: Characteristics and Application", *IEEE Trans. Microwave Theory Tech.*, vol. 42, pp.1454-1462, August 1994.
3. Brian C. Wadell, *Transmission Line Design Handbook*, Boston, Artech House, 1991.


Links to other tasks: In support of Task 3 on Digital Ships

Schedule: This subtask will continue through Spring 2006 in support of methods of feeding antenna structures and arrays. The emphasis will continue as baluns, but feed networks will be considered also.

Personnel: Scott Bates, GRA

### *1.1.3 Importance/Relevance*

The designed compact planar UWB antennas can well accommodate the current needs for the handheld and mobile terminals. Efforts continued in this area, but were not a focus this quarter.

Specific requirements were identified to set the antenna specifications for the software defined radio and Sea Basing tasks. This is described in the task summary for this quarter. Recently, new requirements for the Sea-Basing and port antenna needs have come to light that are the direction for the next quarter.

A review of both wideband antennas and baluns was performed to provide a focus the antenna needs of the project. Techniques for measurement and comparison were presented.

The information of propagation prediction is an item of critical interest in the design of topside platform configurations. Propagation measurements to estimate performance effects were summarized and include initial concepts of applying the results to transient MIMO modeling.

### *1.1.4 Productivity*

Conference publications

1. Taeyoung Yang, William A. Davis, and Warren L. Stutzman, "Normal-Mode, Logarithmic, Ultra-Wideband Tape Helix," *IEEE International Workshop on Antenna Technology: Small Antennas and Novel Metamaterials*, ACES Conference, Miami, FL, Mar., 2006.
2. Taeyoung Yang, William A. Davis, and Warren L. Stutzman, "Some New Aspects of Fundamental-Limit Theory on Antennas," *IEEE AP-S/URSI International Symposium*, submitted, July 3-8, 2006.

Students supported

Taeyoung Yang, Scott Bates, John Kim: Aug 15, 2005 – present
Terry Vogler, Gaurav Joshi: January 1, 2006 – present

Faculty supported

Dr. William A. Davis, VTAG Director, Jan. 15, 2005 – present
Dr. Warren L. Stutzman, Faculty, Jan. 15, 2005 – present

Staff and other personnel supported

Mr. Randall Nealy, VTAG Engineer, Jan. 15, 2005 – present

## 1.2 Task 1.2 Advanced Software Radio

### *1.2.1 Overview*

Task Goal: This task investigates an advanced Software Defined Radio (SDR) which can take advantage of the unique properties of Ultra Wideband communication—such as precision position location, ranging, and low probability of intercept—for Navy applications.

Organization: This task is managed by the Deputy Director of the Mobile and Portable Radio Research Group (MPRG) using the following personnel:

Jeffrey H. Reed, director
R. Michael Buehrer, faculty
William H. Tranter, faculty
Chris R. Anderson, GRA
Swaroop Venkatesh, GRA
Jihad Ibrahim, GRA
Maruf Mohammad, GRA

Summary: This quarter we focused on the development of the final receiver. The DC Power Board and RF Front End have been fabricated and initial performance results are discussed below. The Digital Board and Transmitter will be fabricated in May and we expect to begin system integration in the May/June timeframe.

### *1.2.2 Task Activities for the Period*

*Subtask 1.2a* Develop flexible software radio platforms that includes cross-layer optimization with capabilities for UWB and ad hoc networking

Task objective: The overall goal of this subtask is to design an advanced software-defined/reconfigurable radio which is optimized for ultra wideband communication, and then implement the system using off-the-shelf components. The software-defined radio implementation provides tremendous flexibility compared to a single hardware implementation—for example, providing the capability to utilize one of several different popular UWB modulation or multiple access schemes, to operate in one of several modes (communication, ranging, or data capture), as well as to utilize more traditional broadband communication schemes.

Accomplishments during reporting period: The final phase in the development of the UWB SDR Testbed was to verify that all of the individual subsystems (DC Power Board, Transmitter Board, RF Front End, and Digital Board) met their individual performance targets, and that the Testbed as a whole was able to meet the performance and flexibility requirements discussed in previous reports. In this quarter we were able to fabricate and evaluate the DC Power Board and RF Front End, and the results are in good agreement with the expected performance.

DC Power Board

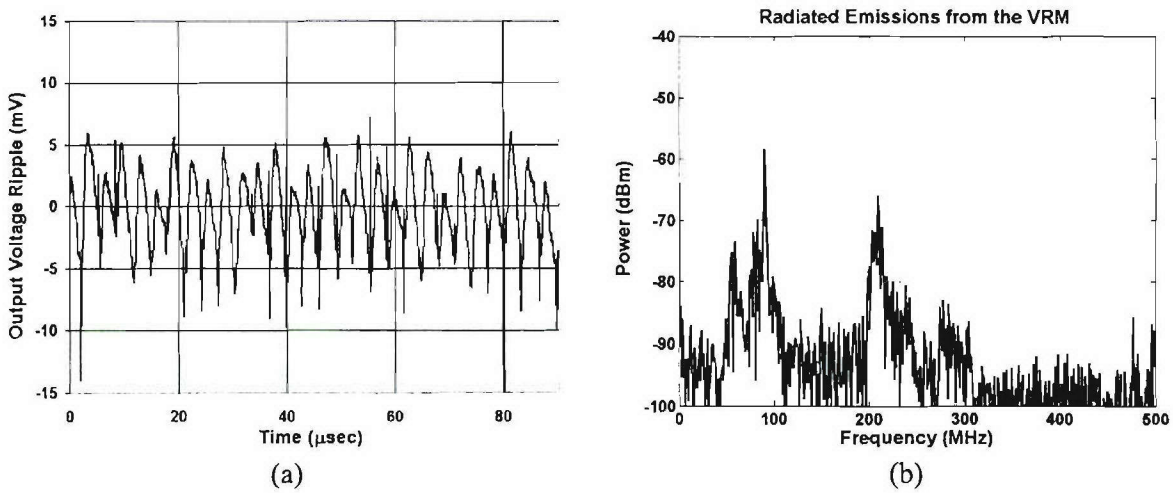
The primary purpose of the DC Power Board is providing the Transmitter Board and Digital Board with a steady, stable voltage supply that meets their current consumption requirements. In particular, the VRMs on the DC Power Board had to meet the following requirements:

- Supply up to 11 Amps of steady-state current
- Maximum 30 mV peak-peak (±15 mV) ripple in the output voltage
- Minimal radiated EMI

To evaluate the performance of the DC Power Board, the output of each VRM was connected to a specific power resistor. The value of the power resistor was set such that each VRM would be supplying approximately 10 Amps of current.

Figure 1.2-1a shows that the output voltage regulation of the VRM is approximately 20 mV, which is in line with the VRM constructed for the prototype receiver and well within the allowable limit of 30 mV peak-peak ripple. Additionally, the output voltage of all VRMs was observed to remain steady and stable under the full 10 Amp load, verifying that the VRMs were capable of delivering their full rated current.

To measure the EMI, a broadband biconical antenna was placed a distance of 1 meter away from the board. To evaluate EMI, a broadband biconical antenna was placed a distance of 0.5 meter away from a single VRM, and a sample of the background noise was captured using a Tektronix TDS 580D digitizing oscilloscope. The VRM was then powered on and a second signal (which contained the background noise plus the EMI generated by the VRM) was recorded on the oscilloscope. The spectrum of the time-domain waveforms was then generated using an FFT in Matlab. To estimate the EMI generated by the VRM, the spectrum containing only the background noise was subtracted from the spectrum containing both background noise and EMI. The result is plotted in Figure 1.2-1b. The figure shows that the total EMI generated by the DC Power Board is mostly contained within two frequency ranges: 50-100 MHz and 200-300 MHz, with a peak of -58 dBm at 90 MHz. In fact, the EMI generated by the entire DC Power Board is less than the EMI generated by a single VRM used on the Prototype Receiver, and therefore, its




performance was deemed acceptable.

**Figure 1.2-1** Performance evaluation of the DC Power Board. (a) Measured output voltage regulation of a Voltage Regulator Module, and (b) Radiated EMI from the DC Power Board when all VRMs are operating at full rated output.

RF Front End

The purpose of the RF Front End is to amplify and condition the received UWB pulse for ADC conversion, while imparting as little noise or distortion as possible. To verify the performance of the RF Front End, a series of tests were performed, including:

- Noise Figure
- Third Order Intercept
- S-Parameter
- UWB Pulse Distortion

The results of the testing are summarized in Table 1.2-1 and discussed further in the following sections.

**Table 1.2-1** Performance Summary of the RF Front End

| Parameter | Predicted Performance | Actual Performance |
|---|---|---|
| Noise Figure | 4.8 dB | 9.0 dB |
| OIP3 | 25.0 dBm | 25.4 dBm |
| Gain | 40 dB | 43 dB |
| Gain Flatness | ± 2 dB | +20 / -0 dB |
| Bandwidth | 20 – 2700 MHz | |
| Pulse Distortion | -- | 21 mV RMSE |

Noise Figure

Using the Tangential Sensitivity (TSS) technique [Tsu01, Tsu89], the RF Front End's noise figure was measured at 9.0 dB, which is almost twice the predicted value of 4.8 dB. Two possible explanations exist for the discrepancy between the measured and predicted values. First, the noise figure calculation did not take into account minor losses between stages due to cables and connectors. Adding just 0.25 dB attenuation between each stage increases the predicted noise figure to 5.0 dB. Second, the TSS technique is a narrowband measurement technique, and it is unknown how accurate the measurement results are for ultra broadband RF front ends. The 9.0 dB measured noise figure is, however, in the same ballpark as the predicted noise figure and should serve as an upper bound for the RF Front End.

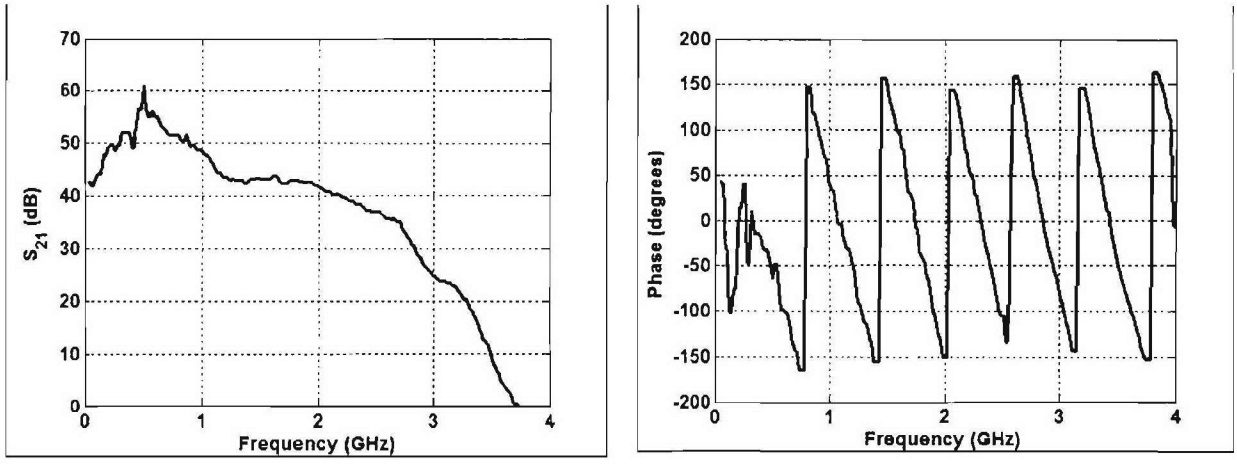
Third Order Intercept Point

The OIP3 of the RF Front End was measured using a standard two-tone test and found to be 25.4 dBm. The only components in the RF Front End that have an impact on the IP3 of the receiver are the ZX60-3018G amplifiers, which have an OIP3 of 25 dBm. Thus, the measurement is in good agreement with the predicted IP3 value.

S-Parameter Measurement

To investigate the frequency response of the RF Front End, a full 2-port S-Parameter sweep was performed using an HP 8510 Vector Network Analyzer, and the results from the S21 sweep are presented in Figure 1.2-2a. To minimize the amount of pulse distortion, the design called for a flat frequency response from DC-2.2 GHz. Unfortunately, as seen in the figure, the frequency response is not flat, with significant excess gain occurring in the frequency range of 100 MHz – 1.2 GHz. Further investigation revealed that the RF amplifiers were the cause of the problem, as they deviate significantly from their specified gain of 20-22 dB. The phase response (as shown in Figure 1.2-2b) is essentially linear over the entire operating frequency range of the RF Front End,

with the exception of the DC-500 MHz range. It is expected that the combination of significant excess gain below 1.2 GHz and nonlinear phase below 500 MHz will result in some amount of pulse distortion imparted by the RF Front End, the measurement of which will be discussed in the



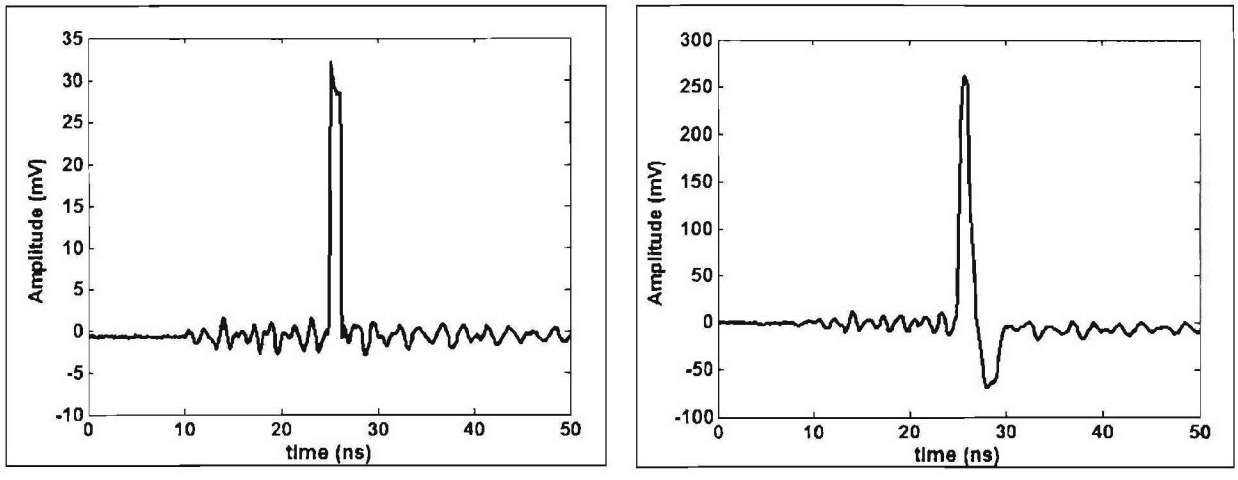

(a) (b)

following section.

**Figure 1.2-2** Measured S-Parameter data from the RF Front End. (a) S21 Magnitude data, and (b) S21 Phase data.

UWB Pulse Distortion

The final test of the RF Front End was to determine how much distortion it imparted to a received UWB pulse. To perform this test, a 1 nanosecond duration UWB pulse was generated using a Picosecond Labs 10,070A pulse generator. The pulse amplitude was set such that the amplitude at the output of the RF Front End would be equal to the maximum ADC input signal, or 250 mV. Both the input and output pulse were recorded using a Tektronix TDS694C oscilloscope




(a) (b)

operating at a sampling frequency of 10 GHz, and the results are shown below in Figure 1.2-3.

**Figure 1.2-3** Measured distortion of a UWB pulse imparted by the RF Front End. (a) 1 nanosecond duration UWB pulse input to the RF Front End, and (b) Measured output of the RF Front End—note slight amount of broadening and dispersion.

As can be seen in the figure, the RF Frond End does impart a small amount of broadening to the UWB pulse, and exhibits a small amount of pulse dispersion (evidenced by the small negative dip after the main impulse).

To gain a more quantitative insight into the impact of the RF Front End on a UWB pulse, the Root Mean Square Error (RMSE) between the amplified pulse and the ideal pulse was calculated. (For comparison purposes, the pulse input to the RF Front End was multiplied by the gain of the RF Front End. The result, therefore, is the pulse that would have been output from a perfect RF Front End.) The resulting MSE was approximately 21 mV, or roughly 8% of the maximum amplitude of the UWB pulse output from the RF Front End. These results were deemed to be acceptable performance for the UWB SDR Receiver.

References:

[Tsu01]J. B. Tsui, Digital Techniques for Wideband Receivers, Boston: Artech House, 2001.
[Tsu89]J. B. Tsui, Digital Microwave Receivers Theory and Concepts, Boston: Artech House, 1989.

Schedule:

- January - June 2006
  - Develop 8-ADC Full Receiver
  - Begin Integration of Receiver with Other AWINN Activities
- April - May 2006
  - Fabricate 8-ADC Full Receiver
  - Fabricate Transmitter Design
  - Fabricate RF Front End
  - Fabricate DC Power Board
  - Verify Operation of Receiver Hardware and FPGA Code
- May – June 2006
  - Demonstrate Transceiver Operation
  - Integrate Transceiver with Other AWINN Activities

Personnel:

Chris R. Anderson – Transmitter and Receiver Hardware Development
Matt Blanton – Receiver FPGA Code Development

*Subtask 1.2b* Software radio research applied to UWB, including design parameter space exploration.

Task objective: The objective of this task is to investigate innovative SDR architectures and algorithms for both traditional broadband and UWB communications. These algorithms will be implemented on the advanced SDR receiver developed in Subtask 1.2a.

Accomplishments during reporting period: This section presents a modified tracking algorithm for UWB pilot-assisted receivers operating in dense multipath. The UWB pilot-assisted or generalized transmitted reference receiver is a widely studied type of receiver which circumvents the low energy capture of Rake receivers by using the received pulse shape itself as a correlation template, and thus achieving complete energy capture. Performance of such a receiver is limited

by a 'noise-cross-noise' term resulting from the use of a noisy correlation template, and a large number of pilots is required to hinder its effects.

Research in UWB synchronization has mainly concentrated on the acquisition process, which aims at obtaining a coarse estimate of the symbol or frame timing. Tracking, which is an ongoing process that refines the initial timing estimate and continuously ensures correct synchronization, has received relatively little UWB research interest, and is usually based on the application of traditional spread spectrum (SS) tracking methods.

In order for traditional tracking schemes to work properly, acquisition must give a reasonably good coarse estimate of the timing delay (within a fraction of one chip duration for SS systems). This assumption is suitable for a UWB Rake receiver, where a separate tracking circuit is assigned to each Rake finger, and acquisition provides a good estimate of the delay of the multipath component corresponding to each finger.

However, the assumption is highly problematic for UWB pilot-based receivers in dense multipath, where the objective of synchronization is to detect the LOS component (which corresponds to the start of the symbol). In fact, since the UWB received energy is spread over tens or even hundreds of multipath elements, there will exist a group of delays corresponding to the different multipath components which can terminate the acquisition process. The LOS path might be severely attenuated and need not be the strongest available path. Detection of the LOS component is thus not guaranteed. Moreover, most UWB acquisition techniques assume that acquisition is successful if any of the available multipath components are detected, rather than the LOS component (see [1] and the references therein). The detected multipath might be tens of nanoseconds away from the start of the signal due to the large channel delay spread. In this case, a traditional tracking algorithm would lock on that selected multipath, and would fail in correcting the large delay error, resulting in significant energy loss, and thus unacceptable performance degradation.

The main limitation of standard tracking techniques applied to UWB in dense multipath is that they are based on the correlation of the received signal with a local stored reference matched to the transmit pulse shape. Such circuits do not take advantage of the received pulse shape, and are thus unsuitable for correcting delay errors which are large compared to the transmit pulse duration. Thus, there is a need for modified fine synchronization algorithms which converge to the LOS component even when they are fed a large delay error by the acquisition stage.

We propose a modified tracking algorithm for pilot-assisted receivers. We will assume that initial acquisition potentially results in the detection of an arbitrary multipath component, thus leading to a timing error much larger than the transmit pulse duration. The tracking method is based on a modified early-late gate approach, where the correlator uses an estimated template of the received pulse shape rather than the transmit pulse shape, thus enabling much higher energy capture during tracking. The symbol intervals preceding and succeeding the estimated delay are processed in order to measure their energy content. The symbol delay is then corrected based on the difference of energy in the two intervals. The method does not require any additional training overhead, and the algorithm is deployed iteratively, where the receiver's correlation template is re-evaluated after delay correction, and data bits are re-estimated using this new template, leading to significantly improved performance.

Proposed Algorithm

We assume a UWB frame structure consisting of $N_c$ pilot symbols followed by $N_d$ data symbols using biphase modulation. The pilot overhead is used to generate the initial system template (similar to template generation in traditional pilot-assisted receivers). Let $T_f$ be the symbol length, and $T_w$ the transmit pulse length ($T_f >> T_w$). We assume an initial acquisition error $\hat{\tau}$ such that $0 \le \hat{\tau} \le T_f$. Moreover, we assume that the error is potentially much larger than the pulse width.

A traditional tracking circuit based on the transmit pulse shape (such as the well known early-late gate) would lock into the multipath component that is in the vicinity of the estimated delay, and would not be able to track the LOS component. We propose a modified tracking algorithm which will correct such a delay error.

The algorithm is presented in Figure 1.2-4. Consider the following two intervals:

- The interval $\left[kT_f + \hat{\tau} - \Delta\tau, kT_f + \hat{\tau}\right]$ (modulated by data bit $b_k$), termed the $k^{th}$ early interval.
- The interval $\left[(k+1)T_f + \hat{\tau}, (k+1)T_f + \hat{\tau} + \Delta\tau\right]$ (modulated by data bit $b_{k+1}$), termed the $k^{th}$ late interval.

Note that $\Delta\tau$ is a system parameter. The algorithm produces two "mini-metrics" $g_k^-$ and $g_k^+$ which measure the energy content of the $k^{th}$ early and the $k^{th}$ late interval, respectively. An early metric $G^-$ and a late metric $G^+$ are then computed by summing the mini-metrics of all early and late intervals. The timing delay is modified based on the magnitude of the difference in energy $G = G^- - G^+$.

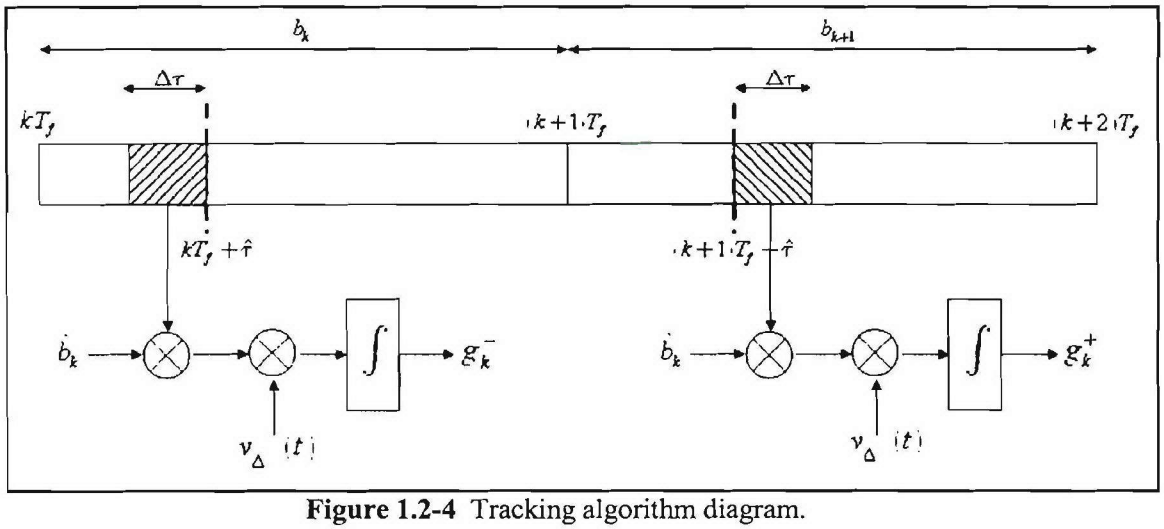



**Figure 1.2-4** Tracking algorithm diagram.

Metric Generation

The metrics $g_k^-$ and $g_k^+$ are generated as follows. First, data modulation is removed by multiplying both intervals by $\hat{b}_k$, where $\hat{b}_k$ is the available estimate of $b_k$ (obtained before timing correction). The early and late intervals are then respectively multiplied by an early and late "mini-template" and integrated.

The early "mini-template" is estimated by coherently adding the demodulated early intervals $\left[kT_f + \hat{\tau} - \Delta\tau, kT_f + \hat{\tau}\right], 0 \le k \le N_d - 1$.

$$v_{\Delta^-}(t) = \frac{1}{N_d} \sum_{k=0}^{N_d-1} \hat{b}_k r\left(t + kT_f + N_c T_f\right),$$

where *r(t)* is the received signal.

The late mini-template is likewise defined on $\left[\hat{\tau}, \hat{\tau} + \Delta\tau\right]$ as:

$$v_{\Delta^+}(t) = \frac{1}{N_d} \sum_{k=1}^{N_d} \hat{b}_{k-1} r\left(t + kT_f + N_c T_f\right).$$

Then:

$$g_k^- = \hat{b}_k \int_{\hat{\tau}-\Delta\tau}^{\hat{\tau}} r\left(t + N_c T_f + kT_f\right) v_{\Delta^-}(t)\, dt$$

$$g_k^+ = \hat{b}_k \int_{\hat{\tau}}^{\hat{\tau}+\Delta\tau} r\left(t + N_c T_f + (k+1)T_f\right) v_{\Delta^+}(t)\, dt.$$

The early and late metrics are given by:

$$G^- = \frac{1}{N_d} \sum_{k=0}^{N_d-1} g_k^-$$

$$G^+ = \frac{1}{N_d - 1} \sum_{k=0}^{N_d-2} g_k^+$$

If $G = G^- - G^+$ exceeds a pre-defined positive threshold $\psi$, then the symbol delay is decreased by a time step $\delta\tau$. If $G < -\psi$, the delay is increased by $\delta\tau$. Else, it is assumed that the intervals do not contain sufficient energy, and the delay is not modified.

In this work, the algorithm is deployed iteratively. Let $\hat{\tau}_i$ be the estimated symbol delay at the $i^{th}$ iteration. A new template $v_{\hat{\tau}_i}(t)$ is estimated based on the new timing delay

Then, new bit estimates are generated based on $v_{\hat{\tau}_i}(t)$. The decision metric $G$ is recalculated, and the delay is fixed accordingly. Note that since the iterative template estimation employs $N_d$ data symbols, the effect of the noise-cross-noise term is reduced as more bits are estimated correctly

(since $N_d >> N_c$ in general). Also, the system parameters may be dynamically modified during the iterative process to increase the tracker's time resolution.

## Simulation Results

We employ real indoor channel measurements taken at MPRG. The LOS component is not completely blocked, but is severely attenuated. A Gaussian monocycle of duration $T_w$ = 500 psec is used. The symbol duration is $T_f$ = 80 nsec, which is longer than the channel's maximum delay spread. In the simulations, we assume an initial acquisition timing error of 16 nsec. The parameters of the algorithm are $\Delta\tau = \delta\tau$ = 4 nsec, and $\psi$ = 0.035 (where the transmitted energy is normalized to 1).

The performance of the proposed system is showcased for $N_c$ = 64 and $N_d$ = 512 and displayed in Figure 1.2-5. First, note that the presence of a 16 nsec acquisition error results in a performance degradation of 3 dB compared to the perfect synchronization case. Moreover, note that the theoretical probability of error expressions derived in [2] match the simulation results. The performance of the receiver with the iterative tracking algorithm is also shown, where 5 iterations per frame are performed before a bit decision is made. Note that the tracker corrects the timing error. Moreover, the system outperforms a pilot-assisted system with $N_c$ = 64, because the improved template is iteratively estimated based on the 512 data symbols, which drastically reduces the effect of the noise-cross-noise term. In fact, at moderate SNR values, few bits errors occur, and performance converges to a traditional pilot-assisted receiver with $N_c$ = 512.

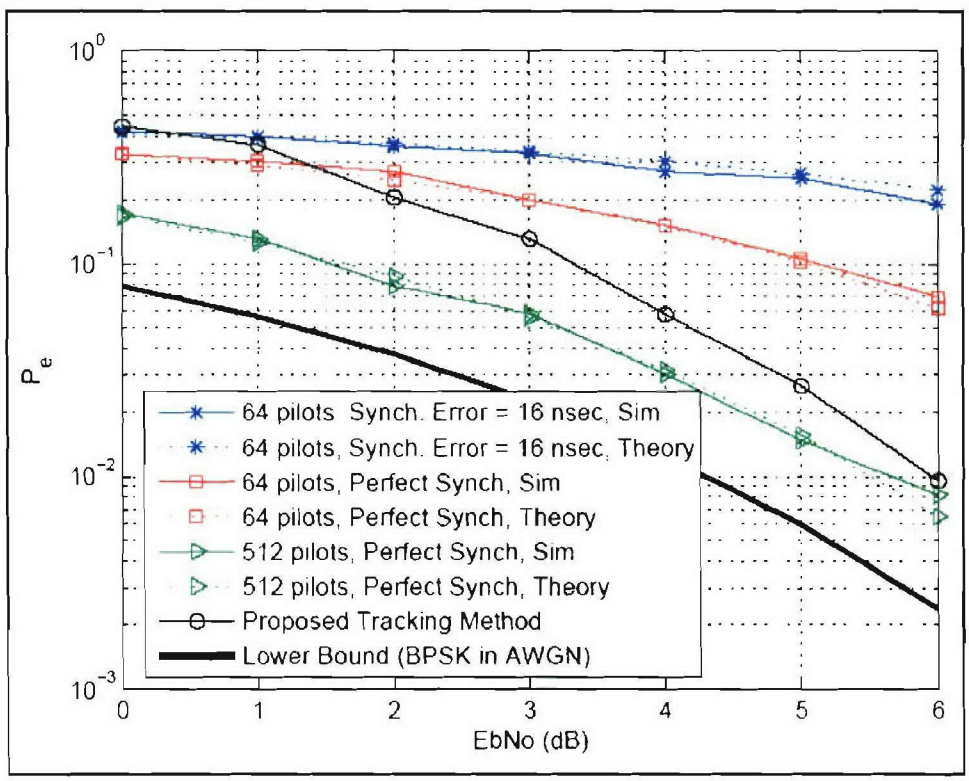



**Figure 1.2-5** Proposed system performance. $N_c$ = 64. $N_d$ = 512.

References


1. J. Ibrahim and R.M. Buehrer, Two-stage acquisition for UWB in dense multipath, *IEEE Journal on Selected Areas in Communications,* April 2006.

2. Jihad Ibrahim and R. Michael Buehrer, "A Modified Tracking Algorithm for UWB Pilot-Assisted Receivers," *submitted to the International Conference on Ultra-wideband,* September 2006.


*Subtask 1.2c* Software radio designs for collaborative systems that take advantage of this radio, particularly for interference environments.

Please refer to Task 4, TIP #1.

*Subtask 1.2d* Vector channel models, including Markov Models, and supporting channel measurements.

Task objective: The objective of this task is to find efficient ways to model error traces generated by real world wireless channels. Different discrete channel modeling methods will be implemented and their accuracy, consistency and robustness will be studied.

***Markov Channel Modeling***

We continue our study of estimating the number of hidden states of HMMs. We have previously found out that for modeling a general binary HMP, we only need two hidden states. We continue to test different binary processes and estimate the number of states of the HMMs.

***Case 1 – Five-state HMM***

In Case 1, we use a 5-state HMM to generate an error sequence. Different HMMs are then developed. Table 1.2-2 summarizes AIC and BIC results.

**Table 1.2-2** AIC and BIC results of different Markov models (original sequenceis a five-state binary HMP).

| Model | k | -l | AIC | BIC |
|---|---|---|---|---|
| 2-state HMM | 4 | 734.4950 | **$1.4656 \times 10^3$** | **$1.4895 \times 10^3$** |
| 3-state HMM | 9 | 734.4852 | $1.4753 \times 10^3$ | $1.5291 \times 10^3$ |
| 4-state HMM | 16 | 734.4815 | $1.4896 \times 10^3$ | $1.5848 \times 10^3$ |
| 5-state HMM | 25 | 734.4400 | $1.5070 \times 10^3$ | $1.6563 \times 10^3$ |

As seen from the table, the 2-state HMM is chosen to be the best model for the given binary data. We now plot different ACFs to observe the closeness of original and developed models. Figures 1.2-6 and 1.2-7 show the ACFs of original and model generated data. It can be inferred that the performance (with respect to autocorrelation) of all these models is the same.

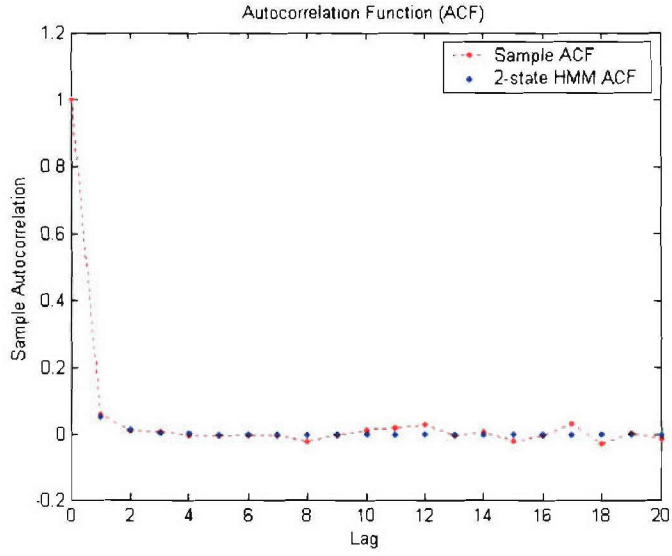



**Figure 1.2-6** First 20 lags of sample ACF and 2-state HMM ACF. Sample ACF is obtained from data generated by a five-state HMM.

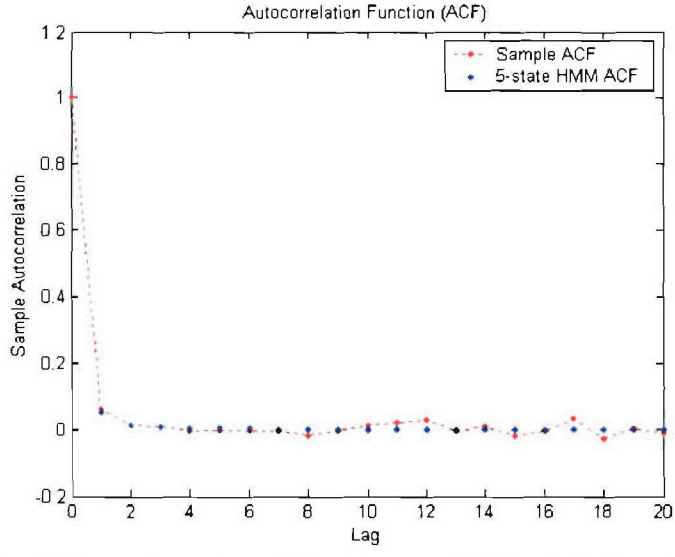



**Figure 1.2-7** First 20 lags of sample ACF and 5-state HMM ACF. Sample ACF is obtained from data generated by a 5-state HMM.

***Case2 - Six-State HMM***

BIC and AIC order estimation is performed on an error sequence that is drawn from a six-state HMM. The result is summarized in the Table 1.2-3.

| **Table 1.2-3** AIC and BIC results of different Markov models (original sequence is a six-state binary HMP). | | | | |
|---|---|---|---|---|
| Model | K | -l | AIC | BIC |
| 2-state HMM | 4 | 736.9440 | $1.4819\times10^3$ | $1.5047\times10^3$ |
| 3-state HMM | 9 | 736.8543 | $1.4917\times10^3$ | $1.5430\times10^3$ |
| 4-state HMM | 16 | 736.7852 | $1.5056\times10^3$ | $1.5967\times10^3$ |
| 5-state HMM | 25 | 736.7299 | $1.5235\times10^3$ | $1.6659\times10^3$ |
| 6-state HMM | 36 | 736.7299 | $1.5455\times10^3$ | $1.7505\times10^3$ |

It is clear from the table that both BIC and AIC choose a 2-state HMM as the best choice even though the data is generated from a six-state HMM. Now we compare the ACFs of 2-state and 6-state HMMs with the sample data ACF in Figures 1.2-8 and 1.2-9. We do not see any improvement in the model by increasing the number of states from 2 to 6.

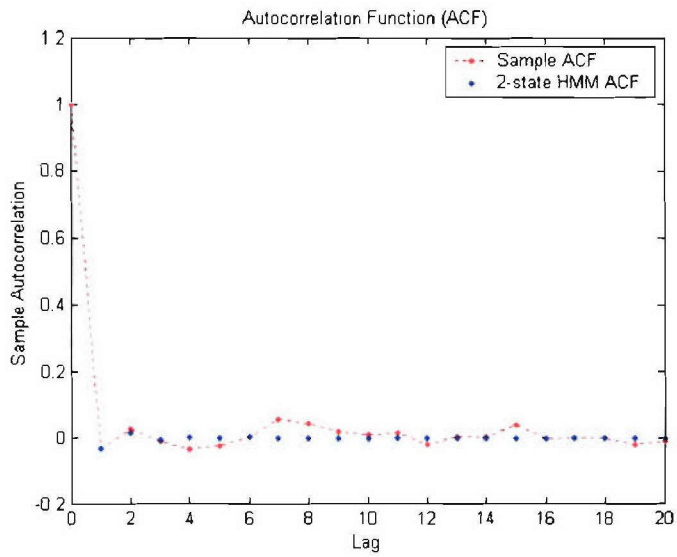



**Figure 1.2-8** First 20 lags of sample ACF and 2-state HMM ACF. Sample ACF is obtained from data generated by a six-state HMM.

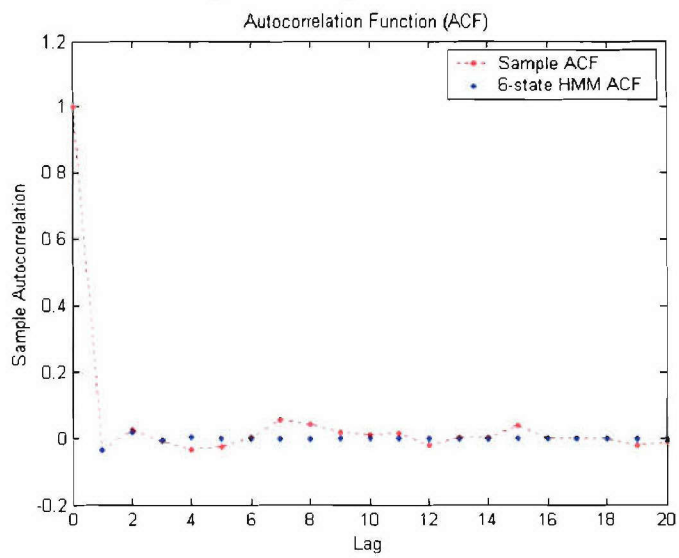



**Figure 1.2-9** First 20 lags of sample ACF and 6-state HMM ACF. Sample ACF is obtained from data generated by a six-state HMM.

***Case 5 - Seven-State HMM***

We test BIC and AIC on the data that is generated by a seven-state HMM. Table 1.2-4 summarizes the results. AIC and BIC choose a 2-state HMM as the best candidate among other HMMs. We now plot the ACFs using the HMMs developed using the original data sequence in Figures 1.2-10 and 1.2-11. There is no significant difference between the ACFs plots of 2-state and 7-state HMMs.

**Table 1.2-4** AIC and BIC results of different Markov models (original sequence is a seven-state binary HMP).

| Model | K | -l | AIC | BIC |
|---|---|---|---|---|
| 2-state HMM | 4 | 734.4950 | $1.4772\times10^3$ | $1.4974\times10^3$ |
| 3-state HMM | 9 | 734.4852 | $1.4872\times10^3$ | $1.5326\times10^3$ |
| 4-state HMM | 16 | 734.4815 | $1.5012\times10^3$ | $1.5819\times10^3$ |
| 5-state HMM | 25 | 734.4400 | $1.5176\times10^3$ | $1.6438\times10^3$ |
| 6-state HMM | 36 | 734.4232 | $1.5396\times10^3$ | $1.7213\times10^3$ |
| 7-state HMM | 49 | 734.4136 | $1.5672\times10^3$ | $1.8145\times10^3$ |
| 8-state HMM | 64 | 734.4105 | $1.5956\times10^3$ | $1.9186\times10^3$ |

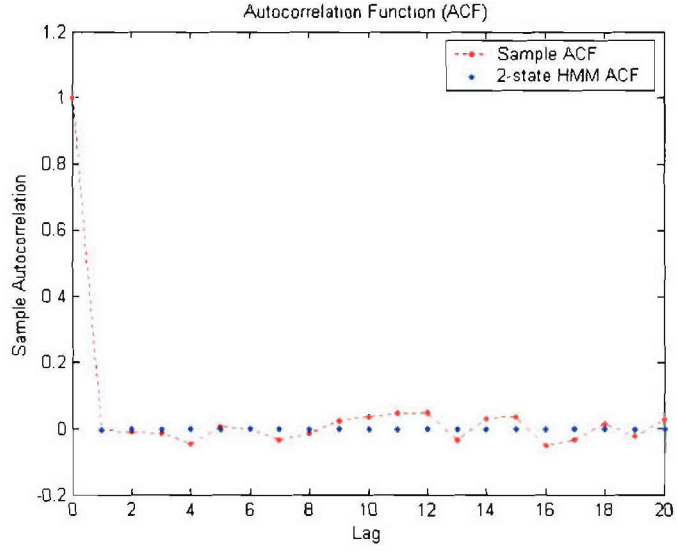



**Figure 1.2-10** First 20 lags of sample ACF and 2-state HMM ACF. Sample ACF is obtained from data generated by a 2-state HMM.

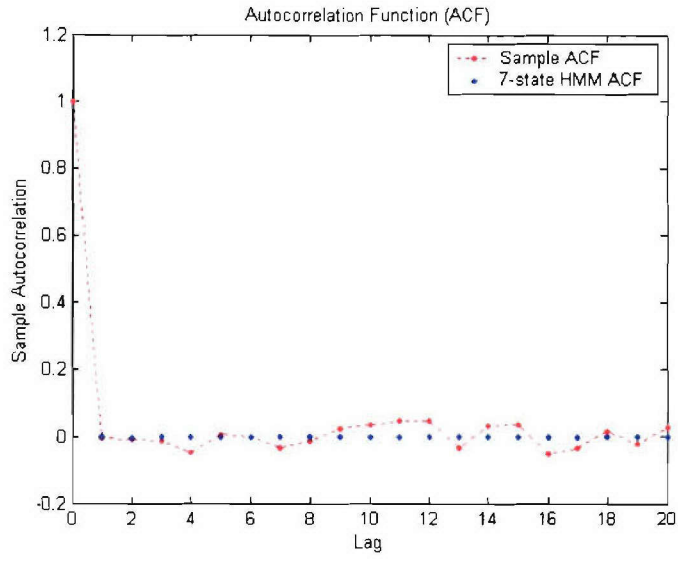



**Figure 1.2-11** First 20 lags of sample ACF and 7-state HMM ACF. Sample ACF is obtained from data generated by a 7-state HMM.

***Rayleigh Fading Error Statistics Modeling***

In this work we further test this conjecture on a Rayleigh fading channel [5] that is quantized into three levels. These levels are $(-\infty, -5\text{dB})$, $[-5\text{dB}, 0\text{dB})$ and $[0\text{dB}, \infty)$ and are represented by state 1, state 2 and state 3 respectively. The BER associated with these states is 0.5, 0.05 and 0.005. The carrier frequency is 900 MHz and the speed of the mobile is 5m/s. Now we train different HMMs by increasing the number of states and find the corresponding AIC and BIC values. Table 1.2-5 shows the results.

**Table 1.2-5** AIC and BIC results of different Markov models (original sequence is a three-state binary HMP).

| Model | K | -l | AIC | BIC |
|---|---|---|---|---|
| 2-state HMM | 4 | 718.6835 | $1.4454\times10^3$ | $1.4691\times10^3$ |
| 3-state HMM | 9 | 717.3340 | $1.4527\times10^3$ | $1.5061\times10^3$ |
| 4-state HMM | 16 | 717.3084 | $1.4666\times10^3$ | $1.5616\times10^3$ |

Next we compare the ACFs of the original error sequence obtained from the Rayleigh slow fading channel and error sequences obtained from the 2-state, the 3-state and the 4-state HMM in Figures 1.2-12, 1.2-13 and 1.2-14.. All the ACFs match very closely with the sample ACF.

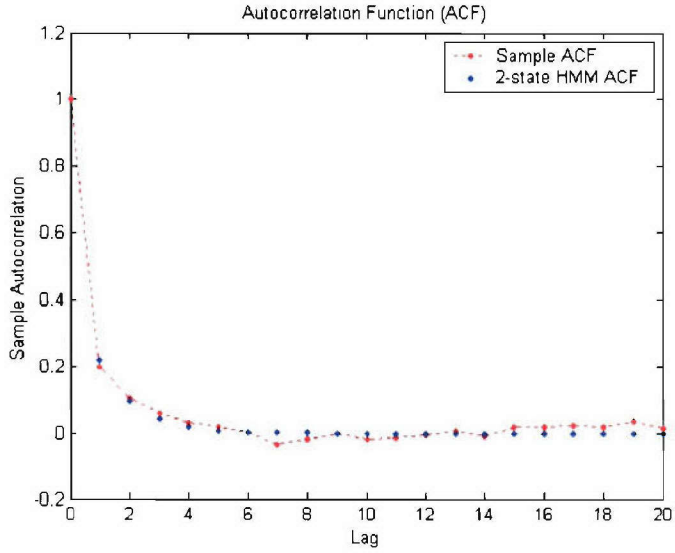



**Figure 1.2-12** First 20 lags of sample ACF and 2-state HMM ACF. Sample ACF is obtained from data generated from a 2-state Rayleigh fading envelope.

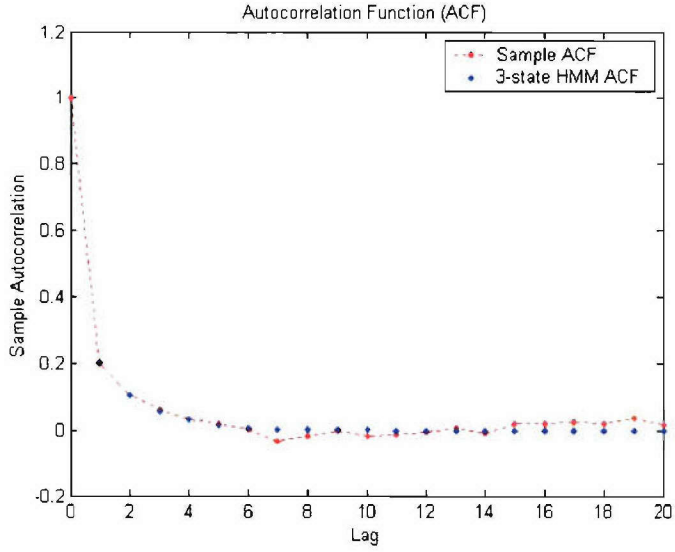



**Figure 1.2-13** First 20 lags of sample ACF and 3-state HMM ACF. Sample ACF is obtained from data generated directly from a 3-state Rayleigh fading envelope.

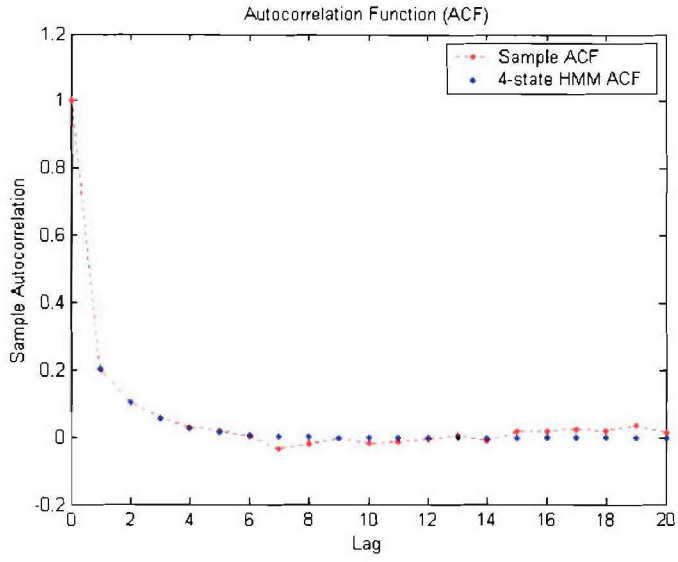



**Figure 1.2-14** First 20 lags of sample ACF and 4-state HMM ACF. Sample ACF is obtained from data generated directly from a 4-state Rayleigh fading envelope.

Table 1.2-6 shows the frequency of error intervals obtained from the original and model generated sequences. There does not seem to be any performance improvement in using 3-state or 4-state HMMs instead of a 2-state HMM. We also compare error-free intervals of the original and HMM generated data. Figures 1.2-15, 1.2-16 and 1.2-17 show that all these models match with the original data error-free intervals.

**Table 1.2-6** Frequency of error intervals observed in original and HMM generated sequences.

| | **Length 1** | **Length 2** | **Length 3** | **Length 4** | **Length 5** |
|---|---|---|---|---|---|
| **original sequence** | 442 | 74 | 32 | 14 | 1 |
| **2 state HMM** | 425 | 85 | 44 | 14 | 3 |
| **10 state HMM** | 465 | 67 | 33 | 10 | 3 |
| **15 state HMM** | 469 | 76 | 31 | 10 | 6 |

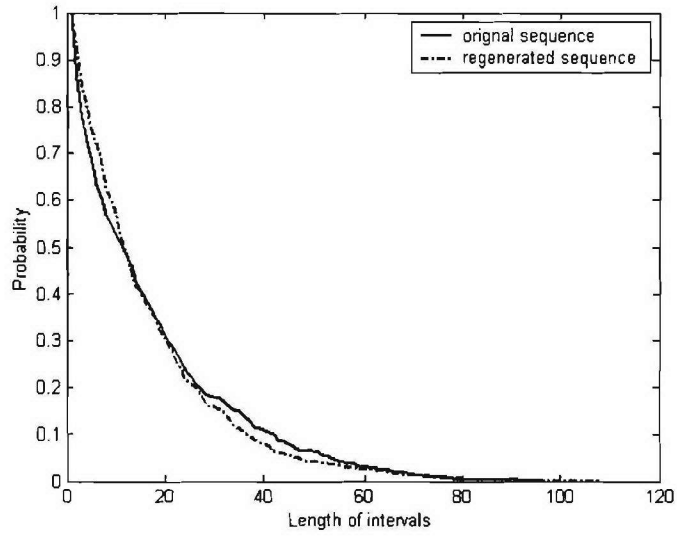



**Figure 1.2-15** Comparison of error-free intervals of the original data and 2-state HMM generated data.

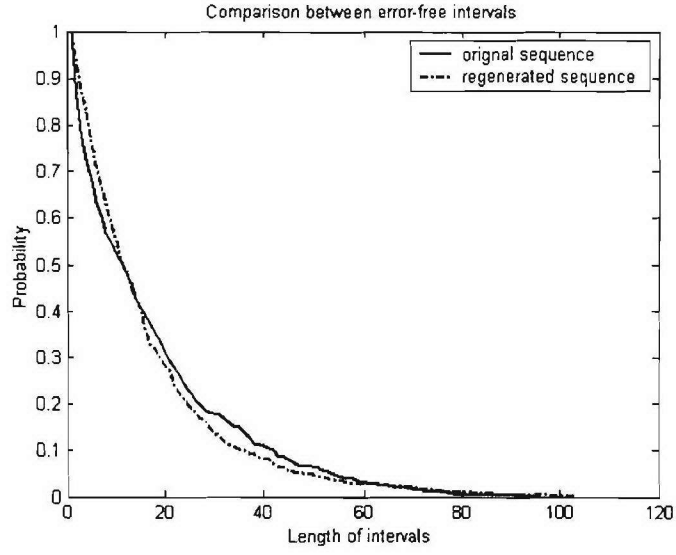



**Figure 1.2-16** Comparison of error-free intervals of the original data and 3-state HMM generated data.

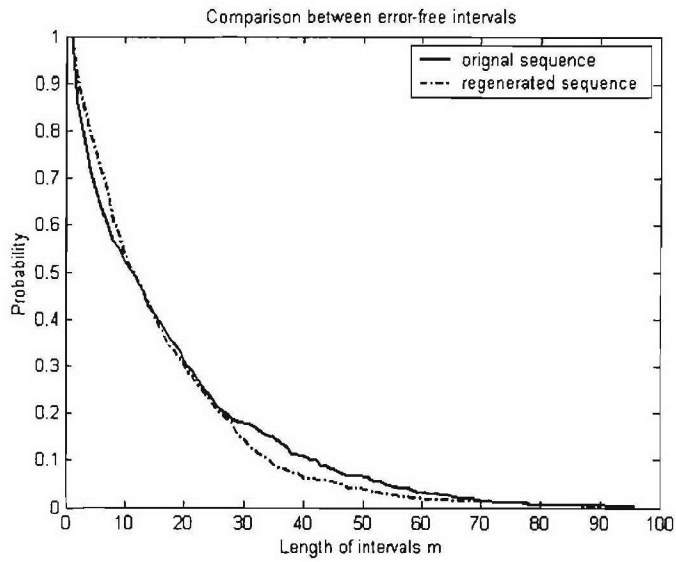



**Figure 1.2-17** Comparison of error-free intervals of the original data and 4-state HMM generated data.

***UWB Error Statistics***

We now test different HMMs on Ultra-Wideband (UWB) channel statistics which were based on channel measurements performed at MPRG. These error statistics are then used as training sequences to train different HMMs. We developed a 2-state, 10-state and 15-state HMM and evaluate the performance of these models in terms of the bit error probability and the frequency of error runs.

**Table 1.2-7** Frequency of error intervals observed in different HMMs.

| | Length 1 | Length 2 | Length 3 | Length 4 | Length 5 |
|---|---|---|---|---|---|
| **Original sequence** | 9123 | 1085 | 112 | 12 | 1 |
| **2 state HMM** | 9123 | 1067 | 136 | 15 | 3 |
| **10 state HMM** | 8801 | 1144 | 150 | 24 | 1 |
| **15 state HMM** | 8904 | 1174 | 153 | 24 | 3 |

HMMs with different number of states are developed based on random initial conditions and the FB-BWA [4] is used to train all these models. Error traces are regenerated from the resulting models and are compared with the original error statistics. From Table 1.2-7 we can observe some performance degradation as we increase the number of states of hidden Markov models. The 2-state HMM seems to be the closest match with this particular UWB error trace.

***Neural Networks and its Connection With the HMM***

In [7], Chapter 17, the authors studied some connection between Artificial Neural Networks (ANNs) [6] and HMMs. ANN, also known as a Simulated Neural Network (SNN) or just Neural Network (NN) is an interconnected group of artificial neurons that uses a mathematical or computational model for information processing based on a connectionist approach to computation. Connectionist approaches base their models upon the known neurophysiology of the brain and attempt to incorporate those functional properties thought to be required for cognition.

Connectionist systems rely on parallel processing of sub-symbols, using statistical properties instead of logical rules to transform information. In most cases the ANN is an adaptive system that changes its structure based on external or internal information that flows through the network. They are nonlinear statistical data modeling tools that can be used to model complex relationships between inputs and outputs or to find patterns in data.

ANNs, like people, learn by example. They are configured for a specific application, such as pattern recognition or data classification, through a learning process. Since ANNs work very well in identifying patterns or trends in data, they are used in variety of applications such as sales forecasting, industrial process control, customer research, data validation, risk management, and target marketing. For more details about ANN, refer to [6].

ANNs are strikingly similar to HMMs. [7] talks about the relationships between HMMs and feed-forward ANNs. The paper actually discusses some HMMs that are defined by ANNs and also certain stochastic ANNs from a hidden variables model in which a threshold logic unit is hidden along with each state of the process. ANNs are usually trained using the back propagation algorithm, which is very similar to the BWA. For further study on the similarities between back propagation and the BWA, refer to [8].

We are not aware of any mathematical proof in literature but it is a well known fact that we generally do not require more than two hidden layers to train an ANN. In our work on HMM order estimation, we have determined that we require only two hidden states to model any arbitrary binary time series. Hence there is likely a strong relationship between the number of hidden layers of ANN and the number of hidden states of HMM. We are further investigating this issue.

***Inference from the Simulation Results***

The lack of mathematical theory for HMM order estimation has led us to rely on computer simulations to estimate the order of binary HMMs. BIC and AIC seem to select the 2-state HMM as the best choice if the true source is the hidden Markov source (of any order). These results are also verified by comparing autocorrelation properties of the original sample data and different HMMs developed from the sample sequence. Rayleigh fading error statistics and simulation of a practical UWB system also support the same result.

***Signal Classification Using HMMs***

In this work, we look at a possible application of HMMs in cognitive radio environment. Cognitive radio [1, 2], often abbreviated as CR, is a wireless communication system in which network or network nodes can change their particular transmitting or receiving parameters to efficiently utilize the existing frequency spectrum. In military, CR can allow equipment to navigate and negotiate frequencies automatically whereas in a civilian environment, this intelligent radio system can use the existing frequency band for broadband communications without interfering the current users.

However, one of the major problems in cognitive radio is to detect and classify the signal present in the environment. We have studied HMM as a potential candidate to address this problem because of its powerful learning and recognition capabilities. We have used Spectral Correlation Function (SCF) and $\alpha$-domain profile of different signals to detect and classify the incoming signal.

Spectral Correlation Function (SCF) and α-domain Profile

A signal $x(t)$ has a time-variant finite-time complex spectrum $X_T(t,f)$ written as [3]

$$X_T(t,f) = \int_{-T/2}^{+T/2} x(u)e^{-i2\pi fu}du$$

Now, if we define $u(t) = x(t)e^{-i\pi\alpha t}$ and $v(t) = x(t)e^{+i\pi\alpha t}$, then we can write the correlation as

$$S_{uv_T}(t,f)_{\Delta t} = \frac{1}{\Delta t}\int_{-\Delta t/2}^{\Delta t/2}\frac{1}{T}X_T\left(t, f+\frac{\alpha}{2}\right)X_T^*\left(t, f-\frac{\alpha}{2}\right)dt$$

It is mentioned in [3] that a time domain signal $x(t)$ contains second-order periodicity with frequency $\alpha$ if and only if there exists correlation between spectral components of $x(t)$ with frequencies separated by the amount $\alpha$, namely, frequencies $f+\alpha/2$ and $f-\alpha/2$ for appropriate values of $f$.

This leads us to a convenient spectrally decomposed measure of the strength of second-order periodicity contained in a time-series for the two spectral components with frequencies $f+\alpha/2$ and $f-\alpha/2$. This is given by Spectral Coherence Function (SCF) between $x(t)e^{-i\pi\alpha t}$ and $x(t)e^{+i\pi\alpha t}$.

$$C_x^\alpha(f) = \frac{\lim_{T\to\infty}\lim_{\Delta t\to\infty} S_{uv_T}(t,f)_{\Delta t}}{[S_x^\alpha(f+\alpha/2)S_x^\alpha(f-\alpha/2)]^{1/2}}$$

$$\text{with } |C_x^\alpha(f)| \le 1.$$

The signal $x(t)$ is said to be completely coherent with the cycle frequency $\alpha$ and spectrum frequency $f$ if and only if

$$|C_x^\alpha(f)| = 1$$

and completely incoherent (contains no second-order periodicity) with the cycle frequency $\alpha$ and spectrum frequency $f$ if and only if

$$|C_x^\alpha(f)| = 0$$

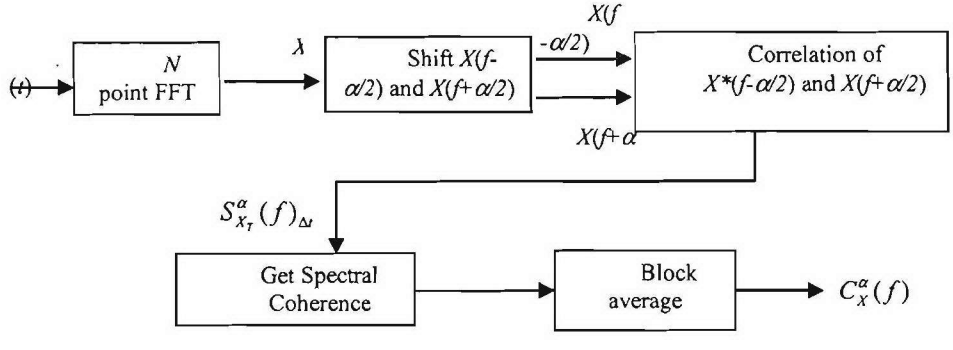



**Figure 1.2-18** Procedure for obtaining SCF.

Figure 1.2-18 shows the procedure of obtaining the SCF of signal $x(t)$. We first obtain $N$-point FFT of signal $x(t)$ and perform shift operation on it. Next the correlation between the two shifted versions is performed to obtain $S_{uv_T}(t,f)_{\Delta t}$. Then the SCF of $x(t)$ is obtained by taking limits of $S_{uv_T}(t,f)_{\Delta t}$ and dividing it by $[S_x^{\alpha}(f+\alpha/2)S_x^{\alpha}(f-\alpha/2)]^{1/2}$. For simplification, we use the maximum of SCF for different values of cycle frequency and denote it as $\alpha$-domain profile.

Signal Classification Model

We generate 100 symbols and use an over-sampling factor of 10. 2048 point FFT is used to increase the resolution for shift operation. Different number of blocks, typically between 20 to 100, are used to perform averaging.

We quantize $\alpha$-domain profile of different modulated signals and use these quantized time-series to build HMMs. These Markov models are then stored in the system's database. The Baum-Welch Algorithm (BWA) [4] is used for model training and different initial conditions are used to avoid local maxima. An incoming signal is then tested with all HMMs and the model that gives the largest value of log-likelihood is selected. The block diagram is shown in Figure 1.2-19.

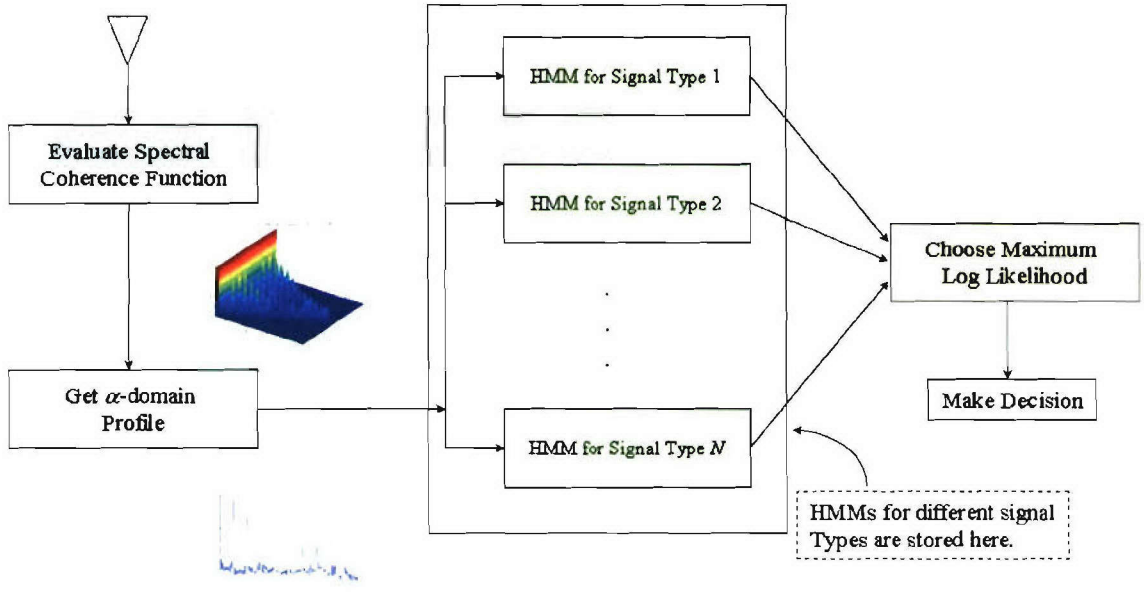



**Figure 1.2-19** Block diagram of a signal classification system using HMMs.

Simulation Results

The Spectral Coherence Function (SCF) and $\alpha$-domain profile of different signals is shown in Figures 1.2-20, 1.2-21, 1.2-22, 1.2-23, and 1.2-24. We can observe that every signal has a unique SCF and correspondingly a unique $\alpha$-domain profile.

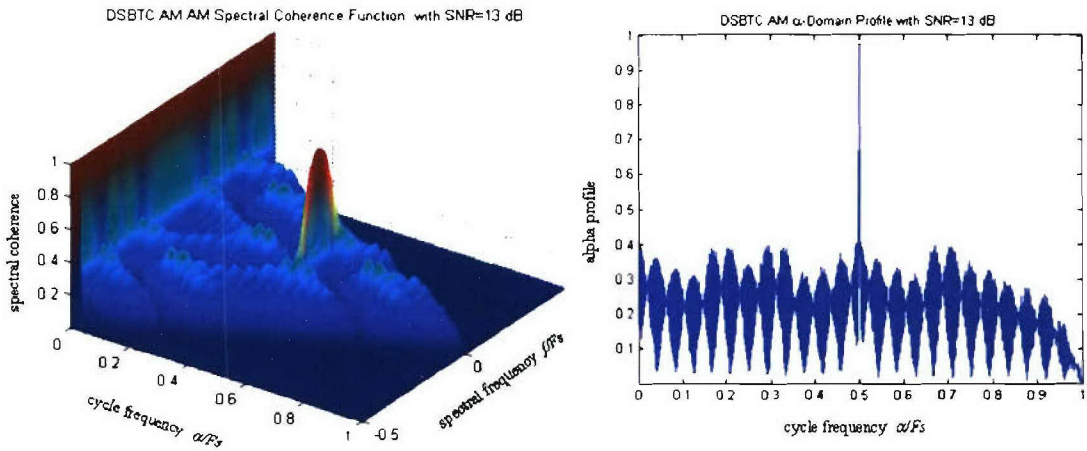



**Figure 1.2-20** SCF of DBTC AM signal and its corresponding $\alpha$-domain profile. SNR = 13dB. Number of blocks used for averaging = 100.

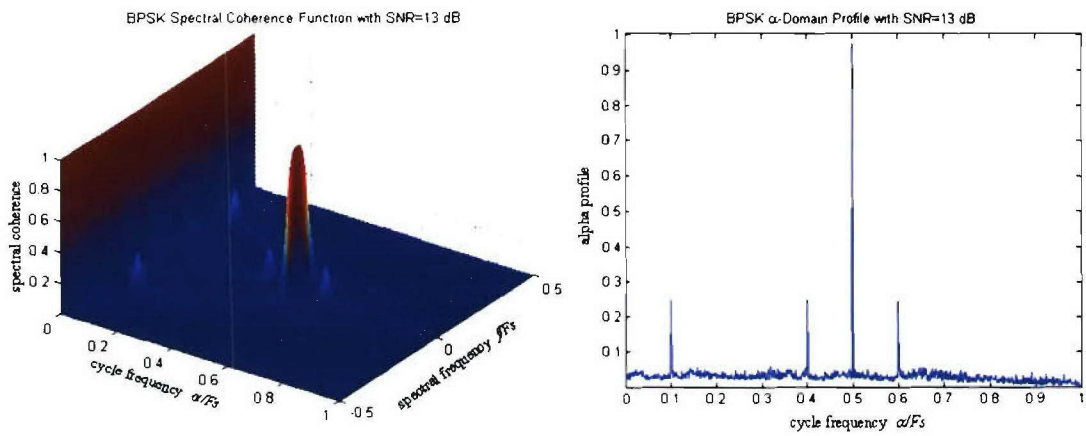



**Figure 1.2-21** SCF of BPSK signal and its corresponding $\alpha$-domain profile. SNR = 13dB. Number of blocks used for averaging = 100

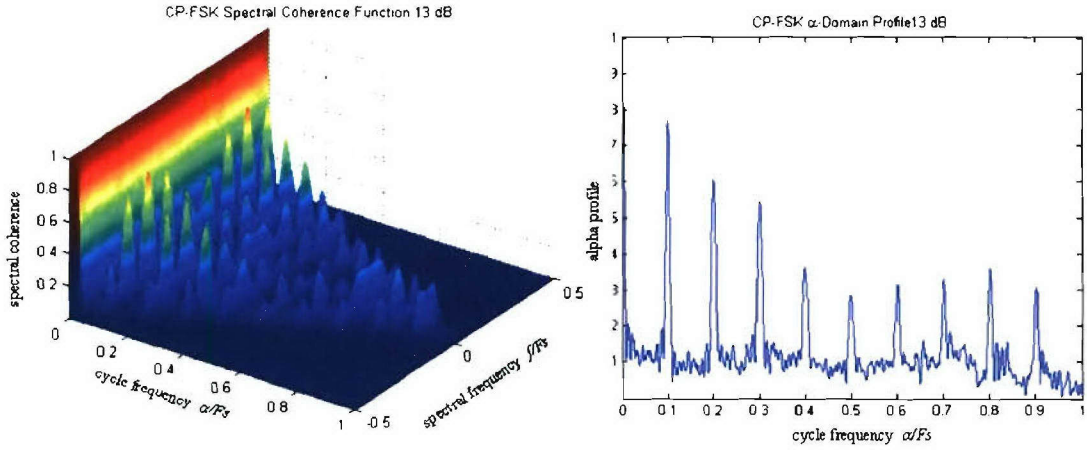



**Figure 1.2-22** SCF of CP-FSK signal and its corresponding $\alpha$-domain profile. SNR = 13dB. Number of blocks used for averaging = 100.

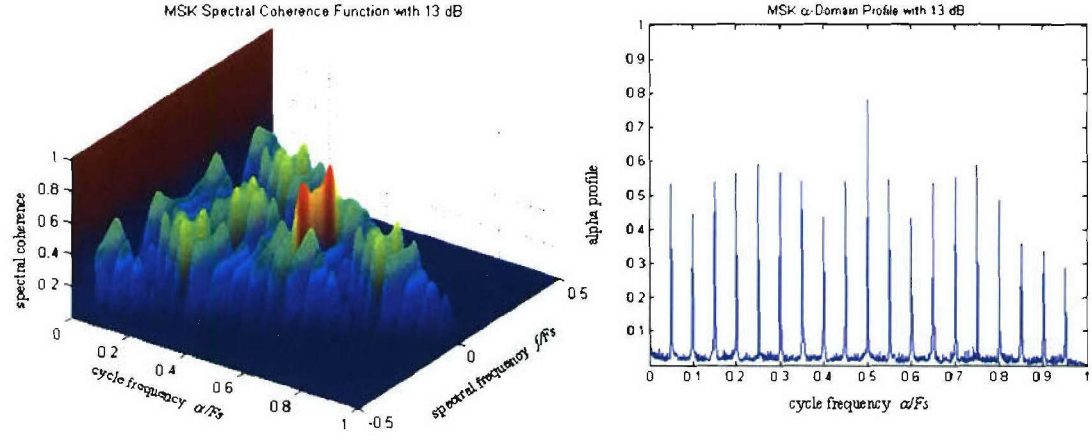



**Figure 1.2-23** SCF of MSK signal and its corresponding $\alpha$-domain profile. SNR = 13dB. Number of blocks used for averaging = 100.

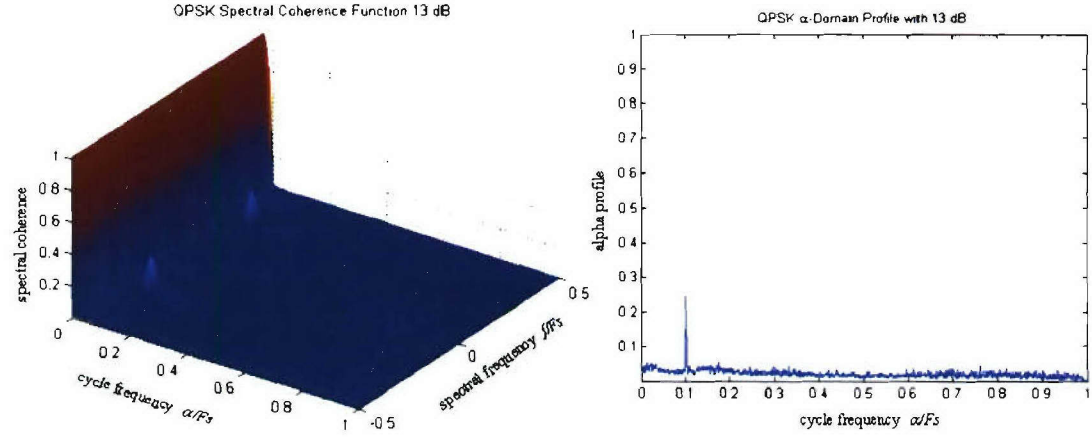



**Figure 1.2-24** SCF of MSK signal and its corresponding $\alpha$-domain profile. SNR = 13dB. Number of blocks used for averaging = 100.

Figure 1.2-25 shows the effect on $\alpha$-domain if we increase the SNR of the signal. The peaks of the signal become more prominent as they add coherently.

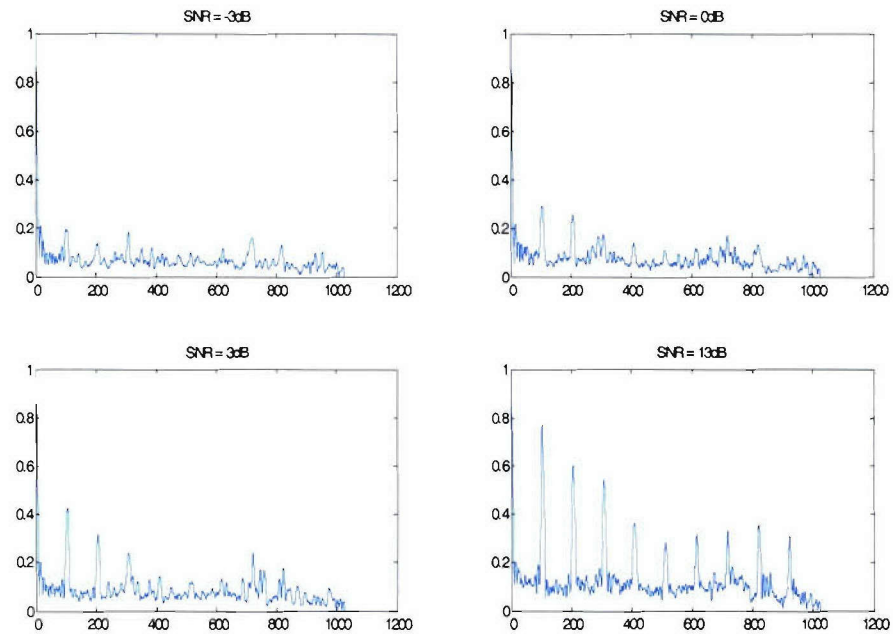



**Figure 1.2-25** Effect of varying SNR on the $\alpha$-domain profile of FSK signals. Number of blocks used for averaging = 100.

Figure 1.2-26 shows the effect of increasing number of averaging blocks from 20 to 100 in case of FSK signal. The noise component of the signal decreases as they add incoherently and the peaks become more prominent.

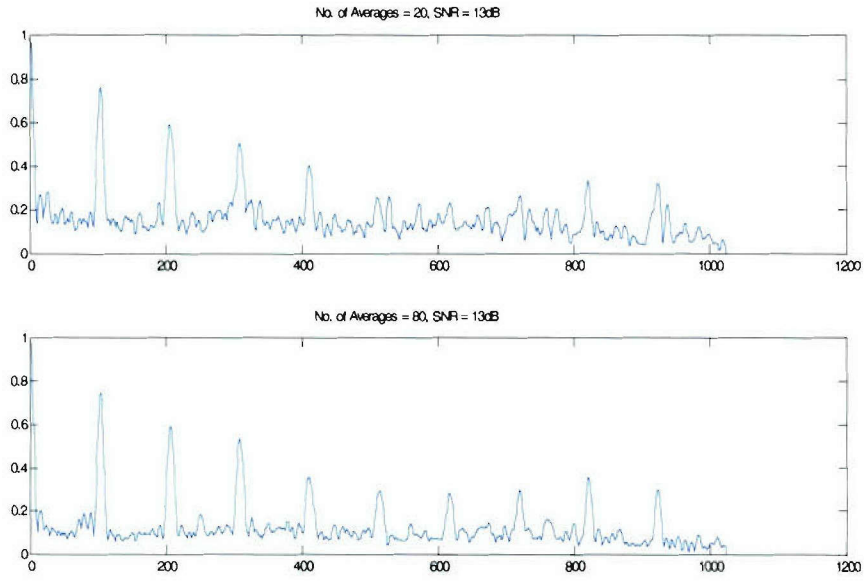



**Figure 1.2-26** Effect of varying number of block averages on the $\alpha$ -domain profile of FSK signals. Top - Number of blocks used for averaging = 20. Bottom Number of blocks used for averaging = 100.

Table 1.2-8 shows the confusion matrix for the case when the SNR of the incoming signals is the same as the SNR of the signals used for developing HMMs. The four different SNRs that we used are -3 dB, 0 dB, 3 dB and 13 dB.

**Table 1.2-8** HMM Signal classification simulation result with known SNR. Number of blocks used for averaging = 20.

| | AM | BPSK | FSK | MSK | QPSK |
|---|---|---|---|---|---|
| AM | 500 | 0 | 0 | 0 | 0 |
| BPSK | 0 | 500 | 0 | 0 | 0 |
| FSK | 0 | 0 | 500 | 0 | 1 |
| MSK | 0 | 0 | 0 | 500 | 0 |
| QPSK | 0 | 0 | 0 | 0 | 499 |
| % | 100 | 100 | 100 | 100 | 99.8 |

Next, we performed simulation using the signal having unknown SNR. BPSK seems to perform worst (miss-classified as FSK 25 times) with 95% accuracy. QPSK is miss-classified 10 times as FSK and 2 times as BPSK giving an overall accuracy of 99.8%.

| **Table 1.2-9** HMM Signal classification simulation result with unknown SNR. Number of blocks used for averaging = 20. | | | | | |
|---|---|---|---|---|---|
| | AM | BPSK | FSK | MSK | QPSK |
| AM | 494 | 0 | 0 | 0 | 0 |
| BPSK | 6 | 475 | 0 | 0 | 2 |
| FSK | 0 | 0 | 500 | 0 | 10 |
| MSK | 0 | 25 | 0 | 500 | 0 |
| QPSK | 0 | 0 | 0 | 0 | 488 |
| % | 99.2 | 95 | 100 | 100 | 99.8 |

| **Table 1.2-10** Effect on signal classification by varying number of blocks. The SNR of the incoming signal is unknown. | | | | | |
|---|---|---|---|---|---|
| | BPSK | BPSK | BPSK | BPSK | BPSK |
| AM | 20 Avgs | 40 Avgs | 60 Avgs | 80 Avgs | 100 Avgs |
| BPSK | 0 | 0 | 0 | 0 | 0 |
| FSK | 475 | 482 | 494 | 497 | 499 |
| MSK | 0 | 0 | 0 | 0 | 0 |
| QPSK | 0 | 18 | 6 | 3 | 1 |

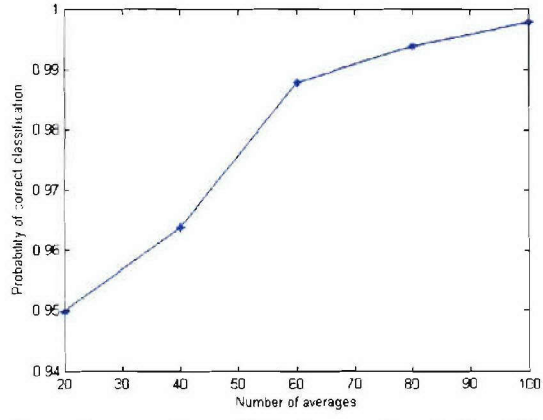



**Figure 1.2-27** Effect of varying number of blocks on signal classification. The incoming signal is a BPSK signal with unknown SNR.

We have also studied the effect of increasing the number of blocks used for averaging in case of BSPK signal with unknown SNR. Table 1.2-10 summarizes the result and the graphical illustration of its accuracy is shown in Figure 1.2-27. It can be seen that increasing number of blocks from 20 to 100 can increase the system performance significantly.

Conclusion and Future Work

We can conclude that HMMs can be successfully used to detect and classify the unknown signal present in the environment. We are studying the effect of having unknown carrier frequency and bandwidth on signal classification.

References


[1] J. Mitola (2000), *Cognitive Radio An Integrated Agent Architecture for Software Defined Radio*. PhD thesis, Royal Institute of Technology.

[2] S. Haykin (2005), "Cognitive radio: brain-empowered wireless communications," *IEEE Journal on Selected Areas in Communications*, Vol.23, Iss.2, Pages: 201- 220.

[3] W. A. Gardner (1988), *Statistical Spectral Analysis*, Prentice Hall Information and System Sciences Series.

[4] I. A. Akbar (2003), *Markov Modeling of Third Generation Wireless Channels*, M.S. Thesis, Virginia Tech.

[5] T. S. Rappaport (1996), *Wireless Communications: Principles and Practice*. Prentice-Hall.

[6] M. Gupta, L. Jin, N. Homma (2003), *Static and Dynamic Neural Networks: From Fundamentals to Advanced Theory*, John Wiley & Sons, Inc.

[7] P. Smolensky, M. C. Mozer, D. E. Rumelhart (1996), *Mathematical Perspectives on Neural Networks*, Lawrence Erlbaum Associates.

[8] J.S. Bridle (1990), "Training stochastic model recognition algorithms as networks can lead to maximum mutual information estimation of parameters," In D. Touretzky, editor, *Advances in Neural Information Processing Systems 2*, pages 211–217, San Mateo, CA.


*Subtask 1.2e* Software radio integration into the AWINN demonstrations.

Task objective: The goal of this subtask is to integrate the software radio developed in Subtask 1.2a into AWINN activities. To achieve this objective, the software radio is being designed with two distinct modes of operation: a communication mode and a data capture mode. The communication mode is currently optimized for impulse UWB signals, however, it is capable of operating using any broadband communication technique (such as DSSS or OFDM). The only limitations on the types of signals that the receiver can handle are: (1) the 2.2 GHz analog input bandwidth limitation of the MAX104 ADCs, (2) the 8 GHz effective receiver sampling frequency, and (3) the processing power of the FPGA.

In the data capture mode, the receiver will simply capture ADC samples and store them in the FPGAs RAM memory. The data can then be processed in non-real time using one of the FPGAs PowerPC processors, or the sample values can be transmitted to a host computer via the USB interface. The number of samples that can be captured is limited by the amount of high-speed RAM memory that can be allocated, but is currently estimated to be around 256,000-512,000 samples—corresponding to about 32-64 μsec of captured data. A trigger signal input allows the

receiver to estimate the time of arrival of received samples for ranging, and the ability to synchronize multiple receivers to a common clock signal allows for precise position location.

Accomplishments during reporting period: Several provisions for integrating the software radio into the AWINN activities have been included in the design of both the prototype and full receiver. To facilitate synchronization of several receivers, the clock distribution network was modified to allow for several receivers to be synchronized to a single clock source. A trigger signal input allows the receiver to operate in the data capture mode and measure the time of arrival for UWB pulses. A trigger output allows the FPGA to control an external UWB pulse generator, to facilitate evaluation of the communication system, ranging, and position location algorithms. Finally, FPGA code for the data capture mode is under development and will be implemented on the prototype receiver board.

Schedule:

- August/September 2005 – Evaluate Prototype Receiver
  - Verify the Receiver Operates in All Modes
  - Verify FPGA Code for Data Capture as well as PowerPC Processing
- October-December 2005 – Refine FPGA/PowerPC code for ranging and/or position location
  - Support Code Development with Measurements either from Lab Equipment or the Prototype Receiver
- Spring 2006 – Integrate Full Receiver into AWINN Activities
  - Crane Demonstration
  - Position Location
  - Imaging
  - Channel Measurements

Personnel:

Chris R. Anderson – Transmitter and Receiver Hardware Development
Matt Blanton – Receiver FPGA Code Development

*Subtask 1.2f* UWB applications to technology development applicable to Sea-Basing: position location, ranging, and imaging.

Please refer to Task 4, TIP #2

*1.2.3 Importance/Relevance*

The simulation results from the SDR testbed simulations demonstrate that the time-interleaved sampling approach is a viable hardware architecture. The use of TI-Sampling with digital demodulation provides a tremendous amount of flexibility in the receiver operation. Even though the receiver is optimized for impulse UWB communication, it should be capable of using almost any broadband communication scheme.

The UWB SDR algorithm design is investigating ways of improving signal acquisition and tracking, as well as operation in multipath environments. Ship-based environment tend to generate a large number of multipath signals and represent a tremendous amount of energy available for the receiver to capture. Using a pilot-based matched filter topology, the receiver can

capture a large percentage of the available energy without resorting to the complex tracking algorithms required by Rake receivers.

The distributed MIMO architecture investigated in this task will allow a number of UAVs to coordinate their transmissions and take advantage of space-time coding performance gains. These performance gains are available even if the various UAVs are not perfectly synchronized—an important consideration if the transmission involves a UWB signal. Combining UWB with distributed MIMO, we believe that long-range transmissions should be possible while still maintaining the LPI properties of UWB signals.

Finally, UWB signals have been demonstrated to have precision ranging and position location properties. Combining 3D ranging information with the crane control system should allow for sea-based ship-ship cargo transfer. Additionally, the position location abilities of UWB will allow for inventory control and tracking, as well as the precision maneuvering required to establish the ship-ship cargo transfer.

### *1.2.4 Productivity*

Students supported

Chris R. Anderson, Jan. 15, 2005 – present
Jihad Ibrahim, Jan. 15, 2005 – present
Swaroop Venkatesh, Jan. 15, 2005 – present
Maruf Mohammad, Jan. 15, 2005 – present

Faculty supported

Jeffrey H. Reed, Jan. 15, 2005 – present
R. Michael Buehrer, Jan. 15, 2005 – present
William H. Tranter, Jan. 15, 2005 – present

## 1.3 TASK 1.3 Collaborative and Secure Wireless Communications

### *1.3.1 Overview*

The Task 1.3 research team was given the duty of deriving an approach to allow independent mobile transceivers to reinforce each other's signal in order to reach a distant base station. This technique spreads the power consumption burden among all nodes so that a single node does not have the full burden of transmitting a message a long distance. Unlike the store-and-forward approach, our approach doesn't require that there be any nodes that are close enough to the base station to individually relay a message to it. Unlike the clustering approach, ours does not require a high-energy local base station to forward messages.

Organization: This task is managed by Directors of Virginia Tech Configurable Computing Lab using the following personnel:

Peter Athanas, Co-Director
Mark Jones, Co-Director
Todd Fleming, PhD student
Tingting Meng, PhD student
Matthew Blanton, MSEE student
Lael Matthews, MSEE student

### *1.3.2 Task Activity Summary*

This section summarizes the activities over the past quarter.

#### 1.3.2.1 High-level Collaborative Communication (Cricket Repeater)

We described a modulation scheme (Random On-Off Keying) in the previous quarterly report that allowed two or more transceivers to reinforce each others' signal, provided that the transceivers are transmitting identical symbols at the same time. In this report, we describe another such modulation scheme (Collaborative Frequency Division Multiplexing) in Section 1.3.2.2 of this report. This section describes *Cricket* – a scheme for synchronizing multiple transceivers. Cricket, when combined with an appropriate modulation scheme, allows multiple transceivers to work together to reinforce each others' signals.

Existing approaches

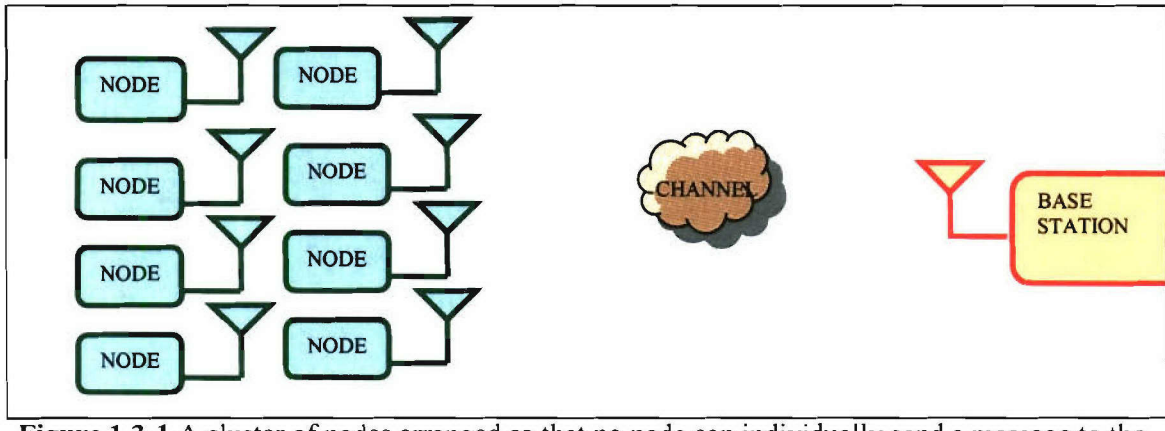



**Figure 1.3-1** A cluster of nodes arranged so that no node can individually send a message to the base station.

Consider the situation where several nodes are clustered together but no node is close enough to the basestation to individually send a message due to power constraints (Figure 1.3-1). The store-and-forward approach will not work in this case because none of the nodes are close enough to the base station to complete a path. If the scenario is modified slightly by adding intermediate nodes (Figure 1.3-2), then the store-and-forward approach will work. However, nodes along the path will relay more traffic than other nodes and thus consume more energy [1].

Another common approach is clustering (Figure 1.3-3). A local base station forwards messages from nearby nodes directly to the global base station. The nodes save energy because they only transmit a short distance, but the local base station consumes more energy than the nodes [2]. A variant of clustering (LEACH) randomly chooses nodes to act as local base stations, but this requires that individual nodes have transmitters strong enough to send messages to the base station [2].

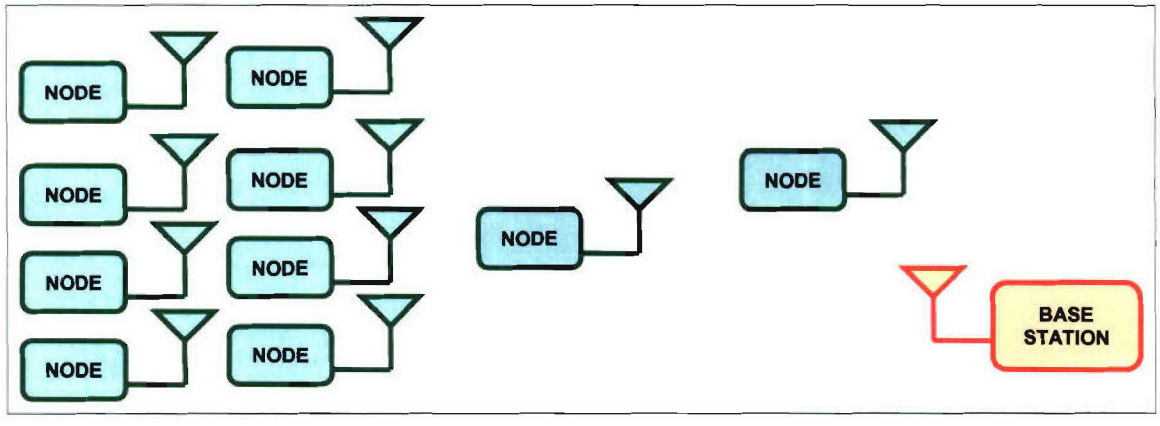



**Figure 1.3-2** Intermediate nodes complete a path to the base station.

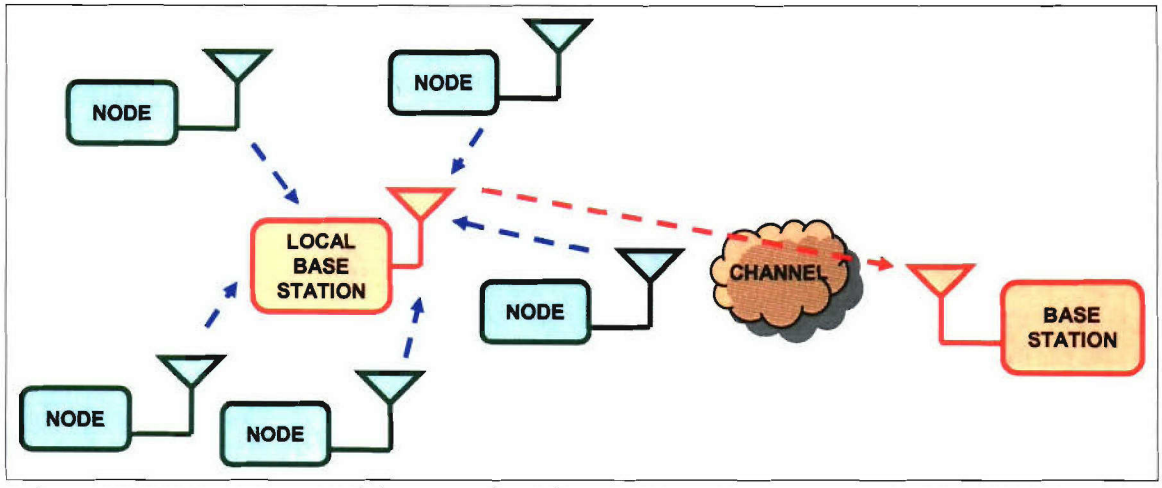



**Figure 1.3-3** Clustering: A high-energy local base station relays messages to the global base station.

Cricket Description

Cricket relies on a wireless communication channel that allows transmissions to reinforce each other. If two or more nodes simultaneously transmit a symbol $X$, then the receiver receives a stronger $X$ than if just one node sends it. The channel must also have the property that nearby nodes can detect a symbol in less time than it takes for a far away node to detect it (fading channel). For example, if the symbol period is 1 μs and nearby nodes are able to reliably detect the symbol after 0.1 μs, then this requirement is met. We described a transmission scheme that meets these requirements in the previous quarterly report and describe another in Section 1.3.2.2 below.

When a node needs to transmit a message a long distance, it first enlists the aid of its nearby neighbors. The source node then switches to transmit mode and the neighbors switch to repeater mode (Figure 1.3-4). The source node transmits symbols sequentially. The repeaters listen for activity on the channel. When they detect a symbol on the channel, they immediately start transmitting that same symbol for a fraction of the symbol period (Figure 1.3-6). They remain silent for the rest of the symbol period (Figure 1.3-7) then start monitoring the channel for further activity.

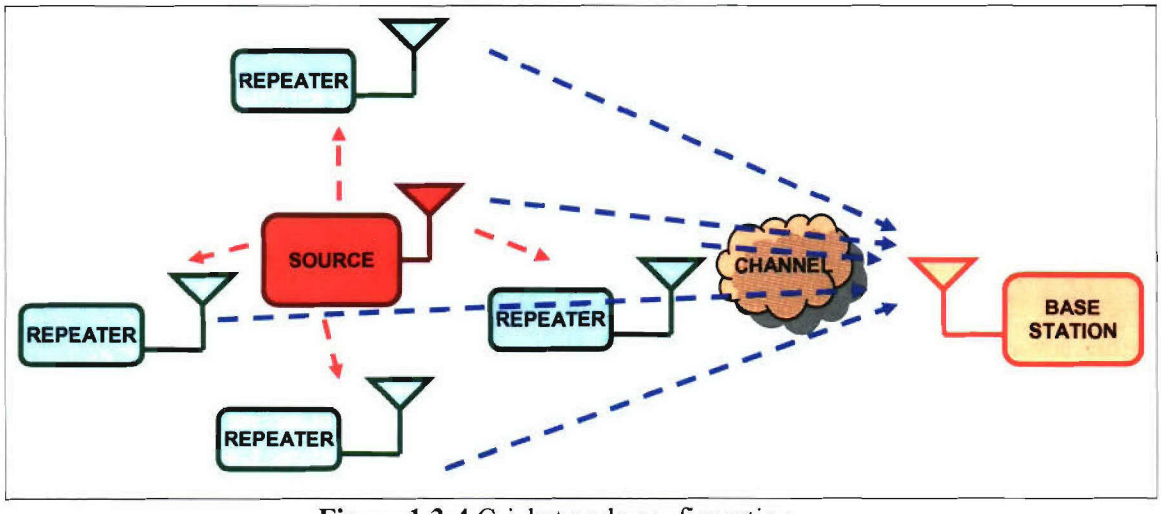



**Figure 1.3-4** Cricket node configuration.

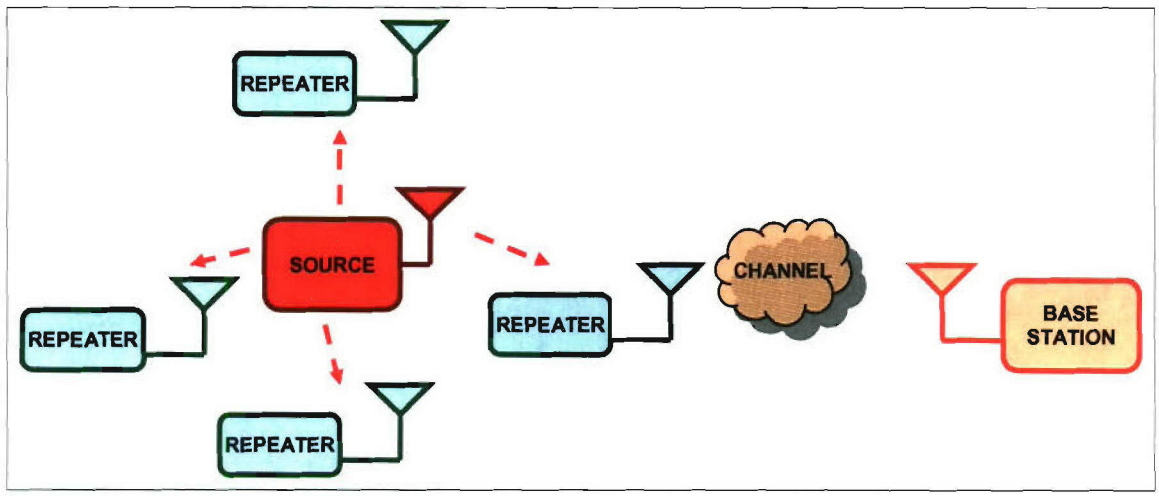



**Figure 1.3-5** Source transmits a symbol $X$; repeaters detect signal.

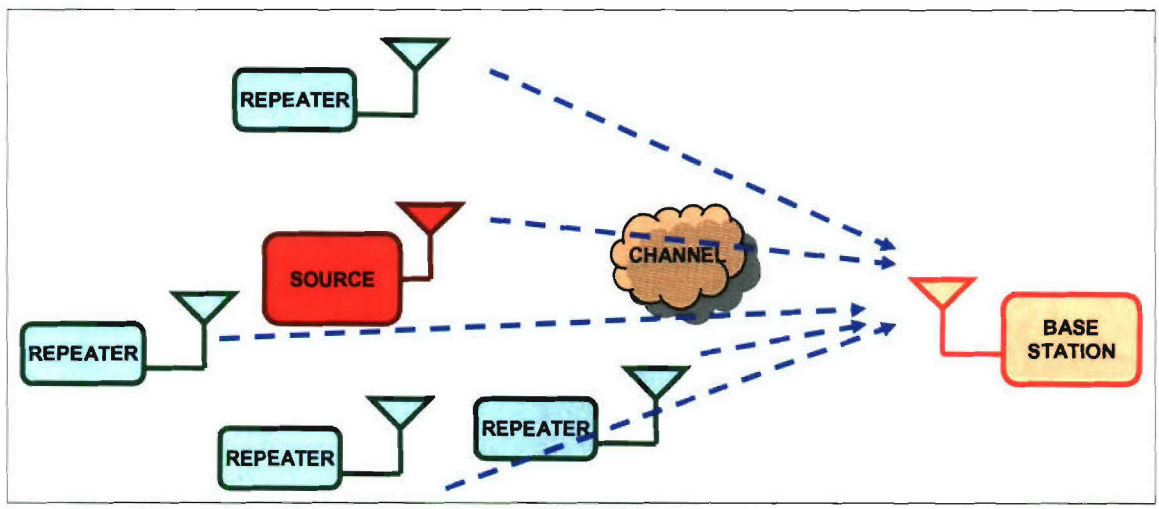



**Figure 1.3-6** Repeaters transmit $X$ while source continues transmitting $X$.

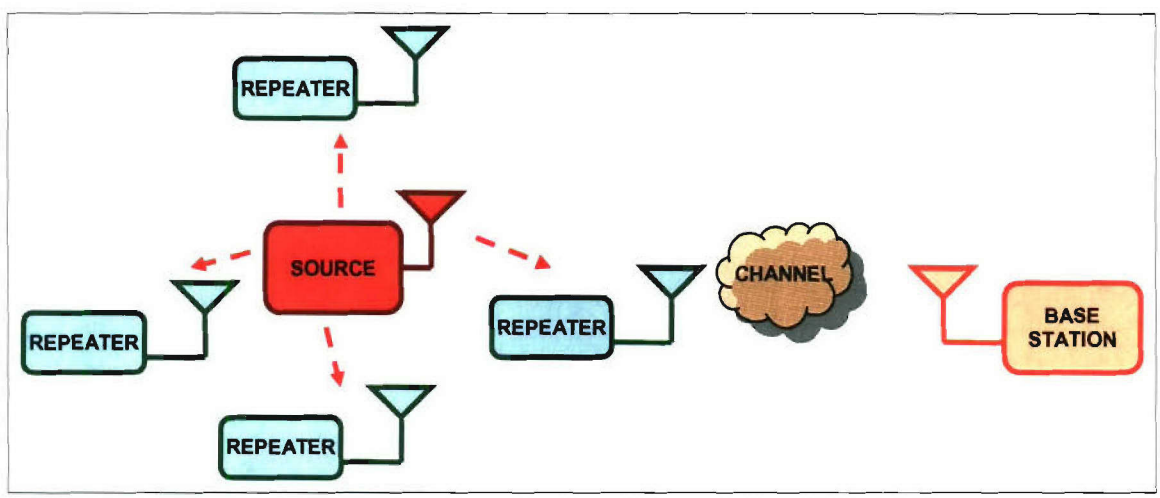



**Figure 1.3-7** Repeaters remain silent for remainder of bit period.

Repeat Duration

The duration that the repeaters send a symbol is based on their positions relative to the source node. The farther the repeaters are from the source node, the shorter the duration must be to prevent inter-symbol interference. When the repeaters are close to the source, the repeat duration is longer and the combined signal is stronger.

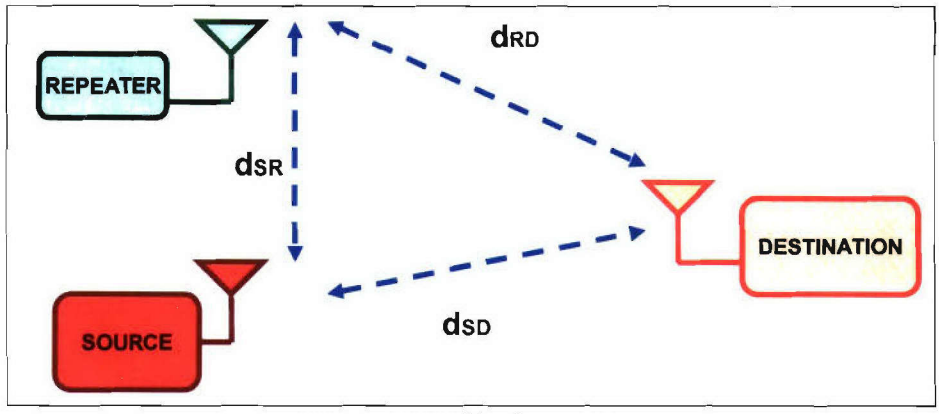



**Figure 1.3-8** Single repeater.

Consider the case where there is only one repeater (Figure 1.3-8). Let $d_{SR}$ be the distance between the source and repeater antennas, $d_{SD}$ be the distance between the source and destination antennas, and $d_{RD}$ be the distance between the repeater and destination antennas. Let $t_S$ be the symbol duration. Let $t_D$ be the time it takes a repeater to detect a symbol and begin repeating it after the symbol's rising edge reaches the repeater. Let $t_R$ (repeat duration) be the amount of time the repeater transmits a symbol.

The source starts transmitting a symbol at Time 0. The repeater detects the symbol and starts transmitting it at time $d_{SR}/c+t_D$, where $c$ is the speed of light. The repeater keeps transmitting the symbol until time $d_{SR}/c+t_D+t_R$. The destination receives the falling edge of the symbol from the source at time $d_{SD}/c+t_S$. It receives the falling edge of the symbol from the repeater at time $d_{SR}/c+t_D+t_R+d_{RD}/c$. To prevent inter-symbol interference, the falling edge from the repeater must arrive at the receiver no later than the falling edge from the source. Thus, $d_{SR}/c+t_D+t_R+d_{RD}/c \leq d_{SD}/c+t_S$, which yields $t_R \leq (d_{SD}-d_{SR}-d_{RD})/c+t_S-t_D$. This can be simplified by assuming a worst-case position of the repeater; $d_{RD} = d_{SR}+d_{SD}$. This yields $t_R \leq t_S-t_D-2d_{SR}/c$. If the positions of all repeaters are within $r_{max}$ of the source and all repeaters have the same $t_R$, then $t_R \leq t_S-t_D-2r_{max}/c$. $t_R$ must be positive; this places an upper bound on $r_{max}$.

Repeater Feedback

The repeaters must not be allowed to get into a feedback loop; that would interfere with the source node's transmission. There are two approaches to prevent this from happening. The first approach is to separate the channel into two bands. The source transmits data on the first band. The repeaters listen on the first band and transmit on the second. The destination would listen on the second band. The repeaters thus would not be able to mistake their transmissions for the source's. The source could optionally transmit on both the first band and on the second so that it contributes to the signal received by the destination.

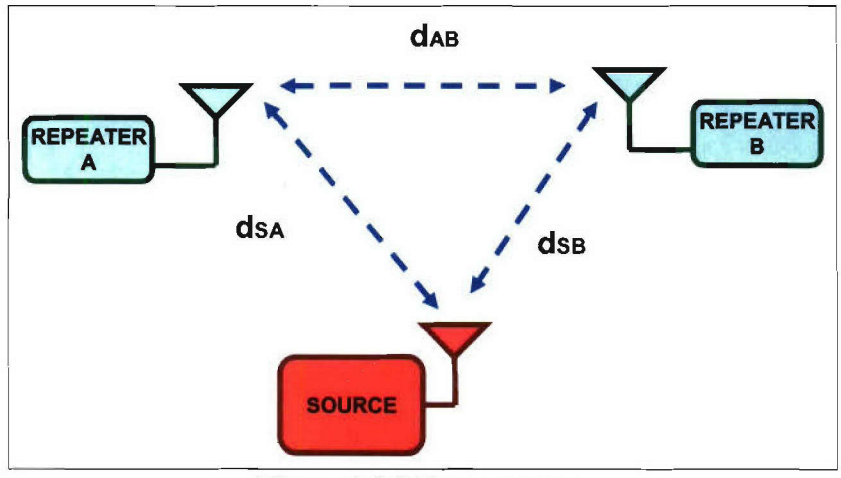



**Figure 1.3-9** Two repeaters.

Another approach would be to restrict the repeat duration ($t_R$) so that no repeater ($A$) transmits at a time that would cause its transmission to arrive at a second repeater ($B$) while the second repeater is listening for a different symbol from the source (Figure 1.3-9).

Let $t_R$ be the repeat duration for Repeater $A$. Referring to Figure 1.3-9 for definitions of $d_{SA}$, $d_{SB}$, and $d_{AB}$, the source begins transmitting a symbol $X$ at Time 0. The falling edge of the repeated signal $X$ from $A$ arrives at $B$ at time $(d_{SA}+d_{AB})/c+t_D+t_R$. The source begins transmitting a second symbol $Y$ at time $t_S$. Repeater $B$ starts listening for $Y$ at time $d_{SB}/c+t_S$. To prevent feedback, the falling edge of $X$ from $A$ must arrive at $B$ no later than $B$ starts listening for $Y$; thus, $(d_{SA}+d_{AB})/c+t_D+t_R \le d_{SB}/c+t_S$, which yields $t_R \le (d_{SB}-d_{SA}-d_{AB})/c+t_S-t_D$. If the positions of all repeaters are within $r_{max}$ of the source, then the minimum value of $d_{SB}-d_{SA}-d_{AB}$ is $-2r_{max}$. Thus, $t_R \le t_S-t_D-2r_{max}/c$. If all repeaters have the same value of $t_R$, then this is the same result as before.

Power Gain

This derivation adopts the following channel model to predict the power gain from multiple transmitters. The energy received ($E_{r,i}$) for a single bit at the base station from transceiver $i$ is $aE_{t,i}/d_i^m$, where $a$ and $m$ are constants, $E_{t,i}$ is the transmitted energy, and $d_i$ is the distance between the transceiver and the base station. This derivation assumes that the energy received at the base station from multiple transceivers is additive.

Let $E_b$ be the energy per bit that a transceiver produces when it transmits a full bit period. Let node 0 be the source node and assume it transmits the full bit period; $E_{t,0} = E_b$. Let repeater nodes all have the same repeat duration ($t_R$); $E_{t,i} = E_b t_R/t_S$, $i \ge 1$. Let $E_r$ be the total energy per bit received at the base station, then

$$E_r = \sum_{i\ge 0} E_{r,i} = \sum_{i\ge 0} \frac{aE_{t,i}}{d_i^m} = \frac{aE_{t,0}}{d_0^m} + \sum_{i\ge 1} \frac{aE_{t,i}}{d_i^m} = \frac{aE_b}{d_0^m} + \sum_{i\ge 1} \frac{aE_b t_R}{t_S d_i^m} = \frac{aE_b}{d_0^m} + \frac{aE_b t_R}{t_S} \sum_{i\ge 1} \frac{1}{d_i^m}$$

A lower bound for $E_r$ has a simpler form. Let $d_{max}$ be the maximum distance between any repeater and the base station. Let $n$ be the number of repeaters, then

$$E_r \geq \frac{aE_b}{d_0^m} + \frac{aE_b t_R}{t_S} \sum_{i \geq 1} \frac{1}{d_{\max}^m} = \frac{aE_b}{d_0^m} + \frac{naE_b t_R}{t_S d_{\max}^m}$$

Assume a worst-case maximum distance between the repeaters and the base station ($d_{max}=d_0+r_{max}$) and pick the repeat duration ($t_R=t_S-t_D-2r_{max}/c$), then

$$E_r \geq \frac{aE_b}{d_0^m} + \frac{naE_b t_R}{t_S d_{\max}^m} = \frac{aE_b}{d_0^m} + \frac{naE_b\left(t_S - t_D - 2\frac{r_{\max}}{c}\right)}{t_S\left(d_0 + r_{\max}\right)^m}$$

The power gain $g$ from using multiple nodes is

$$g = \frac{E_r}{E_{r,0}} \geq \frac{\frac{aE_b}{d_0^m} + \frac{naE_b\left(t_S - t_D - 2\frac{r_{\max}}{c}\right)}{t_S\left(d_0 + r_{\max}\right)^m}}{\frac{aE_b}{d_0^m}} = 1 + \frac{n\left(t_S - t_D - 2\frac{r_{\max}}{c}\right)}{d_0^m t_S\left(d_0 + r_{\max}\right)^m}$$

Since $t_R$ must be positive, $t_S-t_D-2r_{max}/c$ must be positive; therefore, the gain is always greater than 1.

Repeater Selection

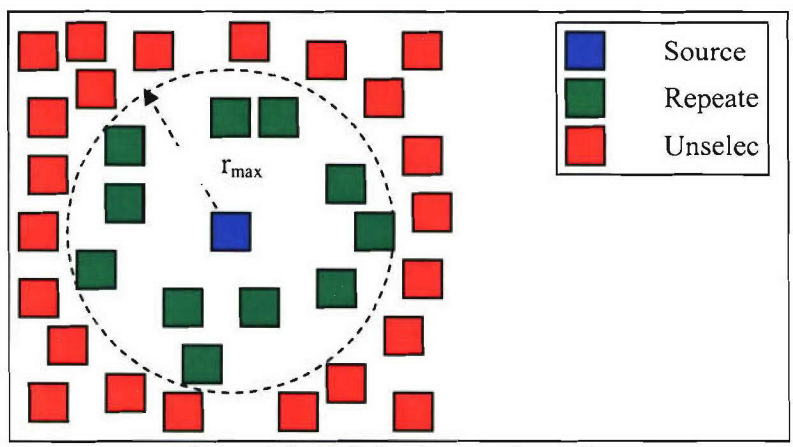



**Figure 1.3-10** Selecting nearby nodes.

A source node needs to pick nearby nodes to be repeaters in order to send a message to the base station (Figure 1.3-10). The lower bound for $E_r$ indicates a tradeoff. If the number of repeaters selected ($n$) is too low, then the energy received by the base station will be too low. However, if $r_{max}$ is too high, then the repeat duration ($t_R$) must be reduced to prevent inter-symbol interference; this will also cause the energy received by the base station to be too low. If the source selects more neighbors than necessary but not so many as to make $r_{max}$ too big, then more nodes will expend energy than necessary. The source needs to select as many nodes as possible to repeat its signal without selecting too many.

The most direct way to select nodes to be repeaters is to select them by their distance to the source. Start with an empty set. If the current set of nodes will not produce a signal strong enough to reach the base station, then add the nearest unselected node to the set and repeat. Future work may consider other selection approaches. For example, the source might avoid picking nodes that have low batteries; this may extend the average node lifetime.

### 1.3.2.2 Low-level Collaborative Communication

Introduction

The collaborative method for the wireless communications focuses on the problem of how multiple independent transceivers can work together to reinforce each other's signal. In our scenario, the sensor network is composed of homogeneous nodes where each transmitter node is able to work independently, for example, a node can move about to perform a given sensing task independent of other nodes. All nodes participate collectively to transmit a message to make it more reliable and robust for distant wireless communications. When a message needs to be sent, a node conveys a local message to all of the other nodes. Then, all nodes transmit this message cooperatively and the combined reinforced waveform reaches the distant receiver node. The proposed scenario makes collaboration among nodes and the signal combination of the nodes incredibly simple, secure, and efficient.

In our previous laboratory work, the waveform combination became a big concern because the resulting waveform that reaches the receiver antenna will be composed of contributions from all nodes in the network. In our previously reported work, we found two solutions to this problem, precise synchronization and a new signal waveform, which we referred to as a band-limited random signal. In this past quarter, we have been experimenting with a new solution to waveform combination, which can be easily implemented. Furthermore, precise synchronization comes for free. This new strategy is based upon the idea of frequency-division multiplexing (FDM). When the sensor network has a message to send to the basestation, signals are sent from multiple nodes at the same time, but on different frequencies. The conventional motivation behind multiple-access FDM is to minimize interchannel interference. We have extended this concept one step further: instead of minimizing interchannel interference, we strive to maximize this. By utilizing our collaborative wireless communication method, each transmitter encodes a bit of data with two temporally separated predetermined frequencies as in Binary Frequency Shift Keying (BFSK). The predetermined two frequency values used by each transmitter are different and chosen carefully. Assume two transmitter nodes *A, B* work together. Each one has a transmitter (TX END) as shown in Figure 1.3-11. The first chip $f_0$ of the transmitter *A* is different and well spaced to the $f_0$ of the transmitter B, and they are grouped at the lower frequency band. Similarly, the $f_1$ of the transmitter *A* is different and well spaced to the $f_1$ of the transmitter $B$,. By choosing the $f_0$ and $f_1$ appropriately, we can differentially detect the data so as to recover the transmitted data more easily and efficiently as shown in the Figure 1.3-12.

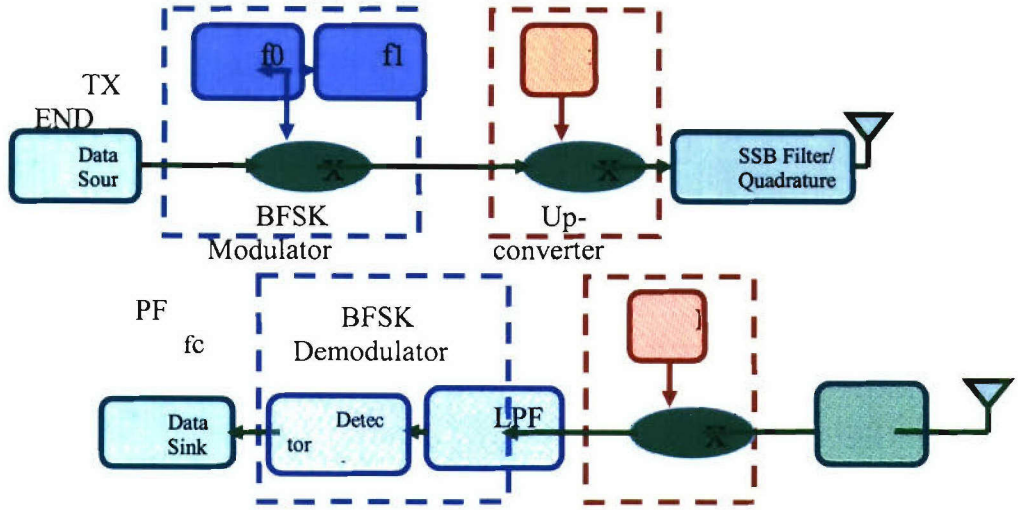



**Figure 1.3-11** The transmitter end and receiver end of the new scenario.

Since every frequency is unique and carefully placed in this scenario, we do not need to worry about the cancellation and the interference between the narrowband sinusoidal waveforms. The more nodes added, the stronger the power would be obtained. Moreover, the differential detection scheme of this scenario is able to lessen the effect of interference. Since we detect the data depending on the power comparison of the different frequency bands, noise will affect the frequency bands of both symbol '0' and symbol '1', the differential comparison result will not be distorted.

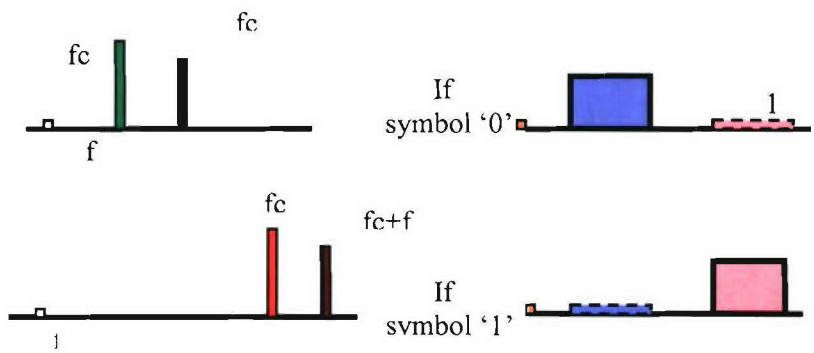



**Figure 1.3-12** The decision scheme in the detector & receiver of receiver end.

Figure 1.3-13 shows the bit error rate performance of the collaborative FDM communications system of this new scenario.

It can be observed from the simulation results in Figure 1.3-13 that when more frequency pairs are used, better performance for the system is expected. Compared to the BER performance of the band-limited random signal scheme we mentioned in the last report, the new scenario has better performance under Additive Gaussian White noise (AWGN), especially in the weak noise environments. We will continue studying both of the two new scenarios under various other interferences in the wireless communication channel.

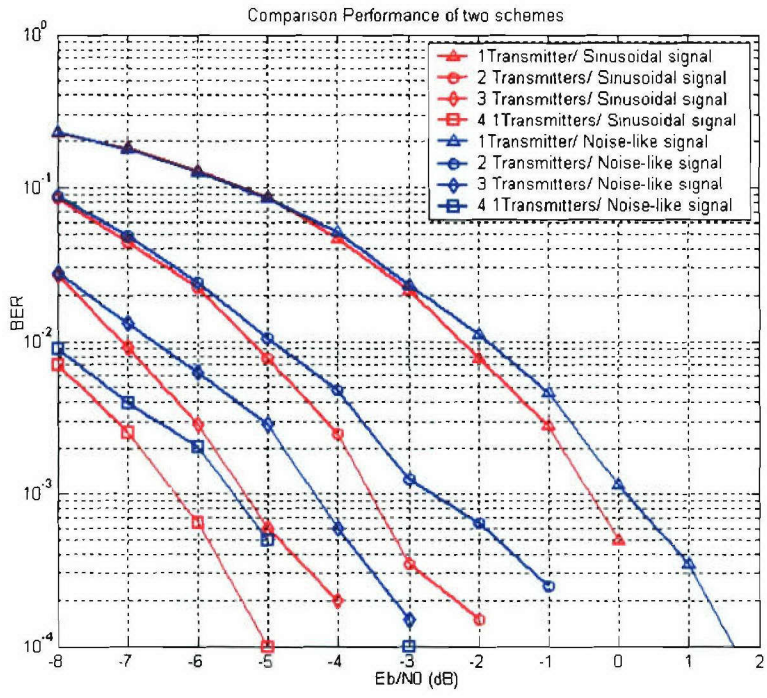



**Figure 1.3-13** The BER performance comparison of the collaborative FDM scenario system and the noise-like signal system.

Bit Synchronization in Receiver

Most of the system simulations and analyses assume bit synchronization is done perfectly, i.e. the receiver knows the beginning of each bit; however, in a real system, signals are transmitted and received sample by sample, and the bit start is ambiguous. Therefore, bit synchronization must be carefully considered to make the real system work properly.

Bit synchronization is an inevitable problem. Basically, bit synchronization is a timing problem that can be understood as the recognition and determination of when a bit starts. Currently, methods are available to achieve bit synchronization for current main-stream communication system products; however, none of these fit our system well. Hence, a specific bit synchronization scheme must be created in the receiver, and can be accomplished in software.

So far, we have designed two different receivers to achieve the bit synchronization. As shown in Figure 1.3-14, we divide the total samples of one bit period into two groups (red and blue in the figure). Each group has half the number of samples per bit. No matter when one bit starts, there is always one group of the two that contains the samples of specific bits and the other group crosses the bit boundary.

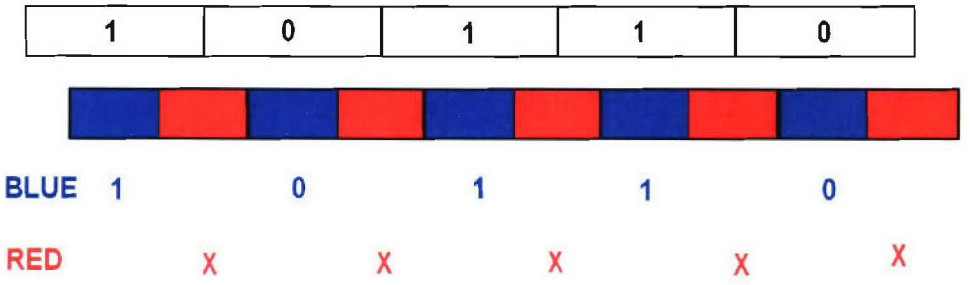



**Figure 1.3-14** Receiver with group scheme.

In Figure 1.3-14, the red group crosses the boundary of two neighboring bits, i.e. the samples in the red group do not belong to any specific bit, and the decision also does not reflect any specific bit value. The samples chosen by the blue group are loyal to the specific bits, and we make the decision with higher confidence. By framing messages with an appropriate header, synchronization can be readily achieved. The red group is judged as a bad group, and the samples of the red group are ignored. The blue group will be recognized as a good group and we will make decisions only depending on the samples of this group.

The smart receiver scheme in Figure 1.3-15 cannot only detect the boundary of the bits but also align the beginning of the bits. There are three steps to this process. Firstly, the samples of one bit are also divided into two different groups. Secondly, a comparison is made between the detected messages of each group and the transmitted header massage. The group that obtains the correct sequence is called *good*; the group that has errors exceeding a threshold is deemed *bad*; and the group between good and bad is called *okay*. Thirdly, depending upon the group conditions (good, okay, or bad) of the current two groups and the previous two groups, we can differentiate eight different modes of bit synchronization as shown in the Figure 1.3-15. For instance, *MOD 1* in the figure indicates that the start of the group is aligned to the start of the bit. We simulated this receiver scheme in Simulink using the model shown in Figure 1.3-16. The simulation result for *MOD 2* is shown in Figure 1.3-187.

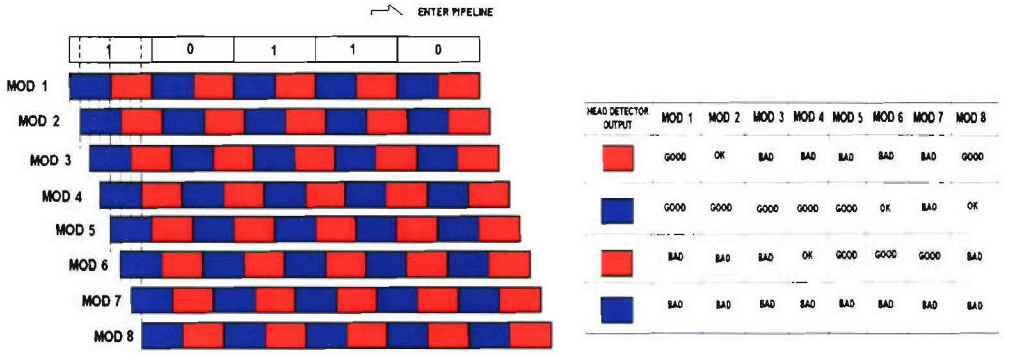



**Figure 1.3-15** Receiver with smart group scheme.

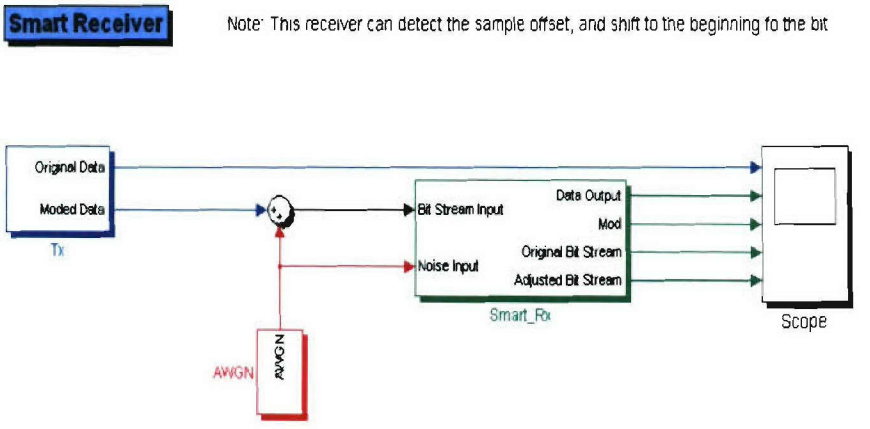



**Figure 1.3-16** Simulink system of smart group scheme receiver.

Figure 1.3-17 shows that how this receiver detects and aligns to the start of a bit. The first top sub-plot presents the transmitted bits, the second sub-plot denotes the received bits, the third sub-plot shows the detected mode, the fourth sub-plot shows the modulated received message without bit synchronization, and the last sub-plot presents the modulated received message with bit synchronization.

In the third sub-plot, a constant value of 2 is produced after a certain time. This "2" produced by *MOD 2* means that $1/8^{th}$ of the samples of one bit happen before expected as shown in the left most red circle. When the receiver produces the constant number, the bit boundary detection is complete, and the sample alignment is started. The start of the group will be postponed so as to align the start of the received bit, as shown in the second and third red circle. Finally the received bit and transmitted bit will be aligned.

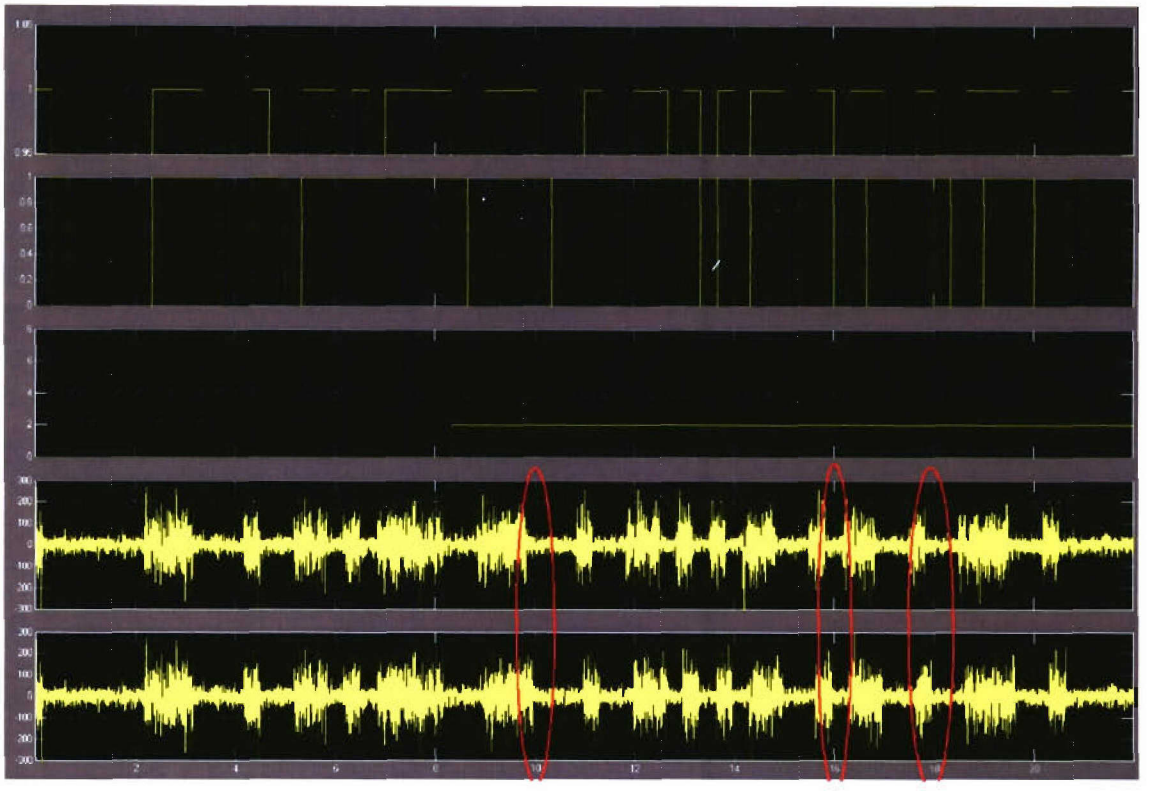


**Figure 1.3-17** Performance results of the smart group scheme receiver in Simulink.

### 1.3.2.3 Position Estimation (for prototyping)

Introduction to the Umbra development package

The Umbra robotics software package developed by Sandia National Laboratories has several features of interest to our ongoing research. One of its most desirable features is its unique capability of mixing virtual environments and components with actual hardware, allowing the developer to perform experiments and analysis on virtual elements before investing in the required hardware. The Umbra framework is software based utilizing C++ as the language for designing modules and also includes and interactive script level interface which facilitates experimentation and deployment of the developed code. A key feature of Umbra is its ability to represent and integrate many items at once. This includes hardware, virtual elements and other simulation programs. Most functions can be broken down into individual modules witch interact through umbra's sophisticated module-to-module interface. This allows the developer to focus on specific phenomena or interactions before integrated them into the full system.

The Umbra package comes with an extensive core set of libraries for representing, displaying and analyzing 3D geometries. In particular, the geometry feature allows the developer to create realistic physical behavior between geometric elements. For example friction can be modeled between wheels and the terrain and obstacles can be modeled to analyze the effects on robot movement. An important feature which is somewhat intuitive is that systems can be modeled in a course sense and then progressively refined to become more realistic. This helps the developer work on one aspect without being concerned with all the details. Control of a robot can be tested

to ensure it moves properly before adding obstacle avoidance or other physical features, which may cause variations in its behavior.

Recent Work

At this point three main features have been explored and demonstrated with the desired response. The first aspect of Umber effectively uses the geometry data bases, Umbra libraries, and script commands to produce an animated vehicle. The second was creating a user defined module in C++ that can be called from the umbra scripting language. Third, elements of a hardware device were successfully connected with the Umbra environment.

**Successful animation**: As mentioned earlier, Umbra has a large set of geometries that can be called to create a virtual robot module. The key element used in this program is known as a *node*. After declaring a node, it can be assigned an offset from the center grid coordinate and connect with other nodes. A node can be an actual shape or simply a point in space which receives input movement commands. In the first demo the original node is simply a point in space with several other nodes connected to it. The other nodes are assigned a shape, size, color, and offset from the original node. By using these simple construction commands a variety of geometric bodies can be created. Once all the shapes are created they must be connected to the main node. Umbra connects modules though their connection ports. Every module that is established within the umbra library contains several member functions ranging from offsets, to updating the module to connections or even status of connections. Most of these members are unimportant for the purposes of this project, however the connect function is essential. It allows the interaction between modules. For the nodes mentioned above we want to connect the output of the base node to the inputs of all the dependant nodes. Commands can now be issued to base node which passes it along to all of its dependants.

The other heavily utilized method in the demo program is the position interpolator. This is another Umbra defined module that essentially takes a starting point at a certain event time and an ending point at an other event time and outputs an interpolated result to move the object between the two points in a smooth and consistent manner. As with all modules this one has input and output connectors. The input connection is tied to the simulation clock while the output `currentValue` is tied to the input of the geometric body. For this demonstration, the event times were set in the script file prior to run time. As simulation time progresses the position interpolator is able to calculate a velocity for the object between the last scheduled event and the next event and output a position vector to the geometric node which is then displayed on the GUI that Umbra utilized for a graphics interface. It should be noted that event times do not necessarily need to be established prior to run time. The TCL scripting language allows the user to insert common "for" loops and "if" statements to guide the program in establishing new event times during run time. A second demonstration involves a simple object which randomly moves about its environment. Future event times and positions are determined every few seconds in a manner which always keeps one event ahead of the interpolator ensuring it always has a start and end point. The triggering device for the loop is simply the `onUpdate` command provide by Umbra. Umbra modules are updated at about 20 Hz, so every time an update occurs the script file will re-evaluate the `proc` call and establish a new event if certain conditions are met. Figure 1.3-18 shows a simple diagram of the interconnection between modules.

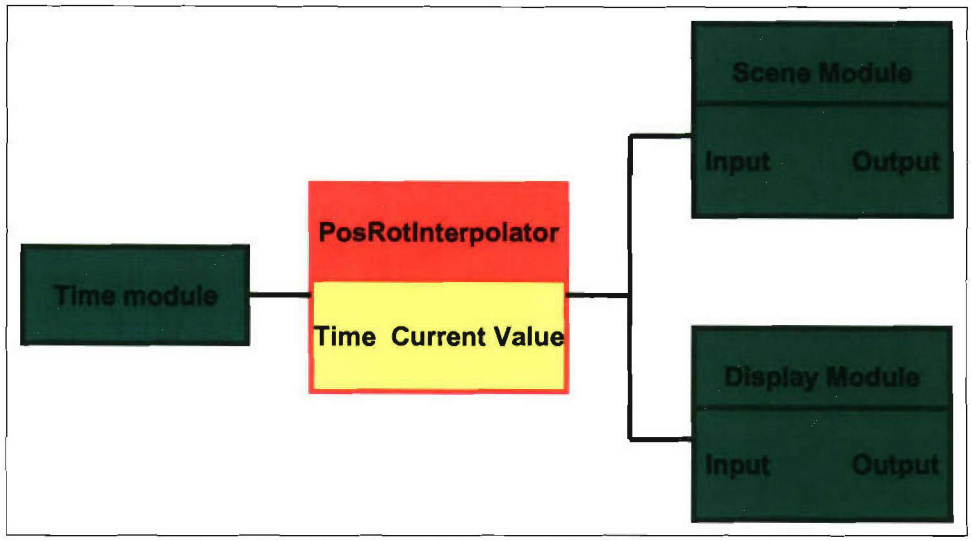



**Figure 1.3-18** Simple diagram of module connection.

Both of the previous demos are easy methods to move a robot or robots in a virtual environment and have their exact position available for analysis. One of the original reasons for implementing this software was to perform analysis on the effects position may play when attempting to perform a beamforming operation. With the environment, virtual robots, and position accuracy ready for utilization, the next step is to make this data available to the simulation tools which are currently being used to examine beam forming capabilities using position as an input.

**User defined Modules:** Two possibilities exist which will provide a valid interface between the Umbra program and the simulator performing the analysis on beamforming. The first method still requires extensive exploration and may involve the use of a *High Level Architecture* and the federation process. Sandia National Laboratories is currently looking into an interface between Umbra and Matlab/Simulink, which is the same program we would like to interface with our Umbra programs. The second method is a work-around that involves creating a new Umbra module in C++ that saves position data to a common file, which the Simulink program can access. Umbra provides a shell for developers to create their own modules. The key part of this shell is establishing the input and output ports to interface with other modules. Variables can be defined as input or output connectors, and functions can be established within the module or with the help of a wrapper, can be accessed from outside the module. An update function is also established which performs the majority of the applicable code. The first module created simply takes an input and returns the same value as the output. It also saves the current position value to a file. Although this module is simple in nature it establishes all the of the basic concepts for building more elaborate modules and can easily be modified without affecting any other modules which may reside in the current system.

**Connecting Hardware:** An important extension to the creation of new modules was the implementation of hardware components. Eventually, research will move beyond the virtual environment and actual robots will need to be tested to validate beamforming results. Utilizing real robots will allow us to examine how well accurate position can be maintained and may help in forming a more realistic virtual robot that behaves in a similar manner. By supplying inaccurate position to the beam forming simulator we will be able to test what effect this will have on the accuracy of the data being transmitted and determine the level at which the signal is degraded in comparison with the deviation of the reported position with the actual position.

Connecting hardware at the most basic level was fairly trivial. Once Umbra has access to all the library files and drivers of the hardware device, connecting it into the Umbra environment is as simple as creating a new module. The ER1 Evolution robot was connected as our hardware device. It utilizes the ERSP robotics software. Umbra was given a path to libraries in this package and was able to make calls to the various resources contained in the ERSP software through a wrapper function. The wrapper essentially allows inputs from within the umbra module to be passed as arguments for the resource call. For the ERSP software to work properly it was necessary to follow their protocol in first initializing the hardware interfaces, making the call to the hardware function, and then cleaning up the interface before exiting. In the demo various calls were implemented in Umbra to the ERSP drive system resource. The device can be controlled from Umbra's script interface by making calls to the various functions in the created module and providing the appropriate arguments. Alternately the device resource functions could be called from within the module's update function using time or some other input as a controller to determine what direction, speed, or distance the robot should move.

Problems and Future Work

The two problem areas of focus at the present time are interfacing the actual robot's motion with the virtual environment and finding a smoother interface between Umbra and Matlab/Simulink. As mentioned previously this is currently under work with Sandia National Laboratories. Once an interface is established, position data will be easier to transmit to the beam forming simulator and feedback data from the simulator can be interpreted by Umbra to influence future robot decisions.

Interfacing the robot's motion with the virtual environment can be achieved by accessing the robots odometer encoders, converting this data to a position and angle value and then converting those values into the position rotation vectors that Umbra uses to plot geometric shapes. Transferring data to the Umbra module has already been achieved; however, there appears to be a problem on the ERSP software side. In the past, most robotic development using the ERSP package utilized a higher abstraction of behavioral level control. Now we are trying to utilize the base resource calls which create a problem if two resources are in use at the same time. The two resources that provide the most interest are the drive system commands and the odometer commands. Since the odometer command initializes at zero, it must constantly be in use while the robot moves around in order to produce valid position data. Of course the behavioral level can produce valid position data and move the robot, so there has to be a solution. Finding this solution will be the thrust of future work along with the Umbra interface with Matlab/Simulink.

### 1.3.2.4 Signal Processing for the Software-Defined UWB Radio

Clock Management Testing

In the previous quarter, design decisions concerning which FPGA device to use in the ultra wideband software-defined radio system were being performed. Those tests have been concluded and an FPGA device has been chosen. It was found that the clocking resources available on the lower-capacity device will be ample for the application. To create all the clocks necessary for the system with given number of clocking resources, several system clocks will need to be generated using the same clock manager used to manage an ADC clock. Tests showed that this is possible, allowing the use of the lower-capacity device in the full system.

SDR FPGA Digital Design

We are currently working on the implementation of the digital hardware for the UWB SDR. Several components of the full system have been tested on the test platform. The test platform is a scaled-down version of the system currently in development, so anything tested on the test platform will be easily ported to the final system.

Matched filter based data demodulation is easily implemented in hardware in a FPGA-based software-defined radio system. In the most basic and most efficient implementation a specific waveform to be matched is hard-coded in the matched filter. This type of matched filter can be implemented in a small amount of FPGA hardware fabric, allowing many matched filters to fit in a device. In the UWB SDR test platform, eight samples are received from the ADCs each clock cycle. This means that instead of one pipelined matched filter, eight matched filters working in parallel were used to perform data demodulation. Each cycle, the eight matched filters performed correlations on combinations of the new samples and the samples received last cycle. This allowed each possible starting sample number to be tested in real time. Figure 1.3-19 illustrates this demodulation system.

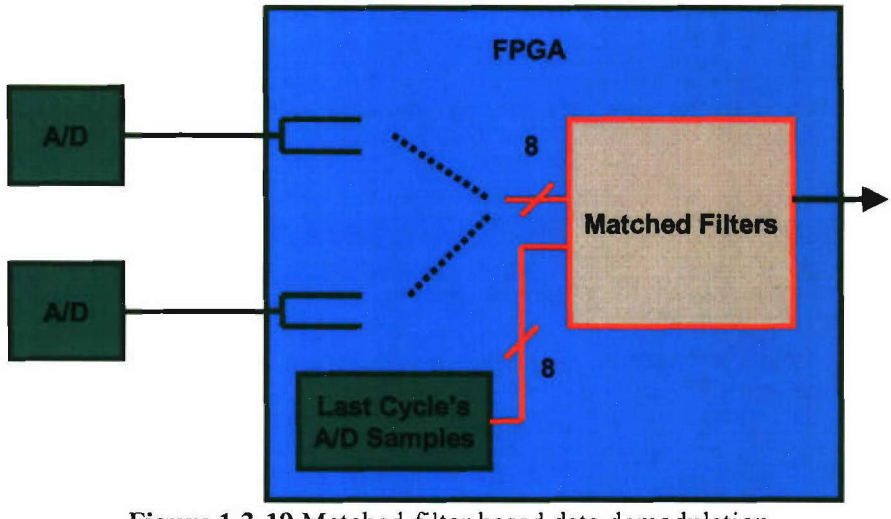



**Figure 1.3-19** Matched-filter based data demodulation.

This system performed well given the input waveform to be matched. The input waveform that was matched in the test which was performed was only two to three ADC samples wide. If the ADCs were not aligned in phase with the input waveform, it could be partially missed. This problem is overcome in the full system by oversampling the input waveform so that a matched filter will still report a strong correlation even if the phase of the input does not perfectly align with any of the ADC clocks. As was stated, the matched filter-based demodulation test showed good results even given the limitations of the input data. The graph in Figure 1.3-20 shows the matched filter correlation value for each starting index for a set of data with a periodic pulse input.

The matched filter correlation value output shows a clear peak with the same frequency with which the input pulses are being sent to the receiver. With more samples per pulse, this peak will be even more pronounced and data demodulation using a matched filter can be performed reliably.

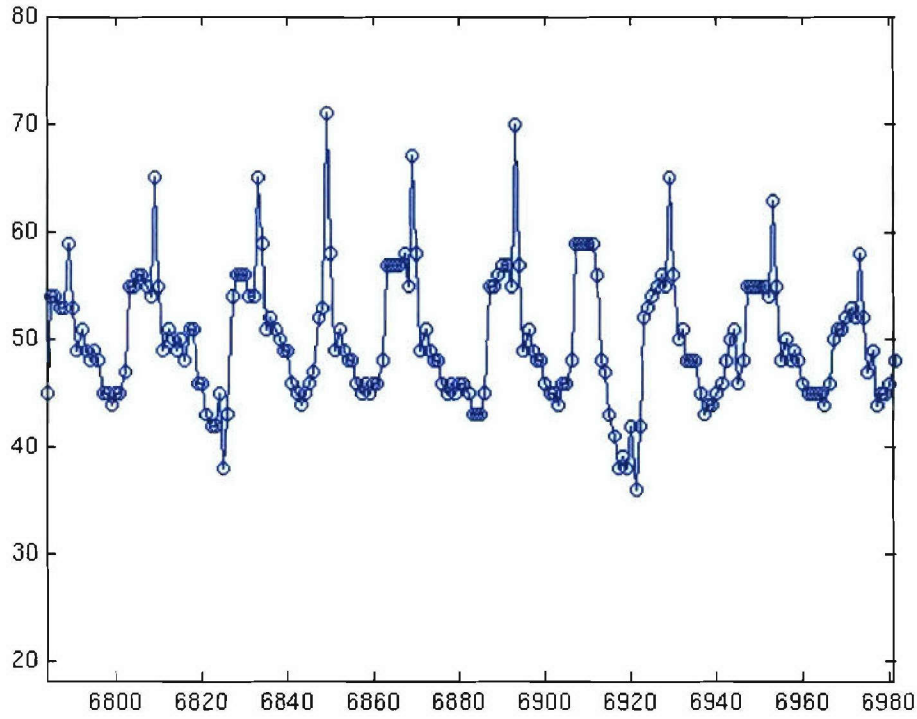



**Figure 1.3-20** Matched filter output variation with time.

Another part of the full system which is being tested on the test system is synchronization of the input data. Without synchronization, input samples can be deinterleaved out of order. A sine wave input could end up looking like the waveform in Figure 1.3-21. With the input data synchronized the rest of the digital system will be able to perform data demodulation reliably.

Eventually the full system will be used with a pilot-based matched filtering demodulation scheme. In this scheme, the receiver will acquire the starting time of the payload pulses sent by the transmitter by way of a set of pilot pulses that are known a priori. The matched filtering for this acquisition phase could be performed in hardware, but we have decided to take advantage of the embedded Power-PC processors available in the Virtex 2 Pro FPGA. We will be running the matched filter algorithm in software on the Power-PC. We are currently testing the software version of the algorithm on the test platform.

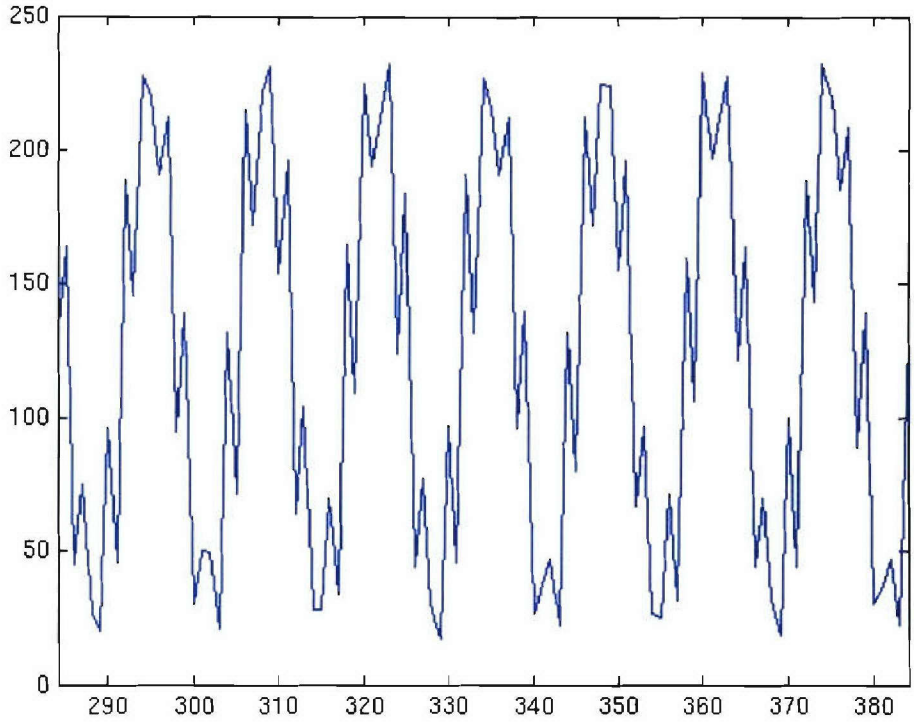



**Figure 1.3-21** Unsynchronized sine wave input.

Future Plans

The full UWB SDR system will soon be fabricated. After the system is ready, many tests will need to be performed to ensure the correct operation of the fixed hardware in the system. These tests will ensure that the FPGA and the ADCs are operational and that the FPGA receives the correct raw data from the ADCs. After the system passes these operational tests the data demodulation system will be made to work on the full system.

References

1. V. Srinivasan, P. Nuggehalli, C. F. Chiasserini, and R. R. Rao, "Energy Efficiency of Ad Hoc Wireless Networks with Selfish Users," European Wireless Conference 2002.
2. W. R. Heinzelman, A. Chandrakasan, and H. Balakrishnan, "Energy-Efficient Communication Protocol for Wireless Microsensor Networks," Proceedings of the 33rd Hawaii International Conference on System Sciences – 2000.

### *1.3.3 Productivity*

Conference publications

1. Anthony J. Mahar, Peter M. Athanas, Stephen D. Craven, Joshua N. Edmison, and Jonathan Graf, "Design and Characterization of a Hardware Encryption Management

Unit for Secure Computing Platforms", Proceedings of the 39th Hawaii International Conference on System Sciences, HICSS 2006 / MOCHA 2006, Kauai, HI, Jan 2006.

2. Stephen Craven, Cameron Patterson, and Peter Athanas, "A Methodology for Generating Application-Specific Heterogeneous Processor Arrays", Proceedings of the 39th Hawaii International Conference on System Sciences, HICSS 2006 / MOCHA 2006, Kauai, HI, Jan 2006.

Invited Talks

1. P. Athanas, "Signal Processing for an 8-GHz UWB Software Defined Radio," at the Dagstuhl Conference on Dynamically Reconfigurable Systems, Dagstuhl, Germany, April 2006.

Students supported

Todd Fleming, PhD student
Tingting Meng, PhD student
Yousef Islander, PhD student
Matthew Blanton, MSEE student
Lael Matthews, MSEE student

# 2. TASK 2 Secure and Robust Networks

## 2.1 Task 2.1 Ad Hoc Networks

### *2.1.1 Overview*

Task goal: This task investigates core network capabilities for quality of service (QoS), security, and routing in ad hoc networks, especially mobile ad hoc networks (MANETs).

Organization: This task is managed by Scott Midkiff and involves or has involved the following personnel:

Scott F. Midkiff, faculty (task director)
Luiz A. DaSilva, faculty
Nathaniel J. Davis, IV, faculty (1/15/05-8/14/05)
Y. Thomas Hou, faculty
Shiwen Mao, post-doctoral research associate
George C. Hadjichristofi, GRA (1/15/05-5/14/05), post-doctoral associate (7/25/05-present)
Waltemar M. de Sousa, GRA (5/15/05-present)
Unghee Lee, GRA (33% for 4/1/05-5/14/05, 100% for 5/15/05-present)
Xiaojun Wang, GRA (06/01/05-01/01/06)

Summary: During this quarter, we continued work on integration of routing and medium access control (MAC) protocols for ad hoc networks to support multiple channel operation, implementation of test bed conversion to support both Internet Protocol (IP) version 6 (IPv6) and IP version 4 (IPv4) including with IP Security (IPsec) and key management. We enhanced the utility of the Optimized Link State Routing (OLSR) protocol by developing an application program interface (API) to provide network information to support integration with higher layer protocols and programs. We defined steps to implement a topology control (TC) mechanism and started the development of the required components. In addition, we began integration of our video communication software with the routing protocol to dynamically obtain network information, using the API cited previously, and exploit path diversity in an ad hoc network. We are also extending our video communication modules to operate in an IPv6 environment. The accomplishments and other details are provided in Section 2.1.2 below.

### *2.1.2 Task Activities for the Period*

*Subtask 2.1(a):* Policy-based Quality of Service

Task objectives: The objectives of this subtask are to investigate and develop quality of service mechanisms that provide differential bandwidth allocation and scheduling based on traffic type, node type, and the current network environment. We seek to increase the adaptability of the QoS mechanisms to operate more robustly in a variety of environments. We will also explore automatic adaptation at the physical and data link layers in response to application and network-layer demands, as an initial exploration of cognitive networks as an approach to cross-layer optimization.

Accomplishments during reporting period: Investigation and planning for this task continued during this quarter. We focused on developing a topology control (TC) mechanism and analyzing existing TC algorithms. We also continued to investigate relevant literature in the field. TC aims

to increase network capacity by means of controlling the physical topology of heterogeneous ad hoc networks, composed of nodes with different capabilities (e.g., different antenna subsystems) and resources (e.g., varying energy supplies). The TC algorithm coordinates nodes' decisions regarding their transmitting ranges with the objective of reducing interference and generating a network topology with desired properties (e.g., higher effective network capacity).

Substantial theoretical and simulation-based work has been performed in the area of TC, but to this date there is a lack of experimental demonstration of the usefulness of TC techniques in reducing node energy consumption and radio interference. We defined an implementation structure for a TC mechanism in the Linux operating system and are currently working on detailed design and implementation. We have also refined the required modifications for our test bed to allow for the evaluation and demonstration of TC.

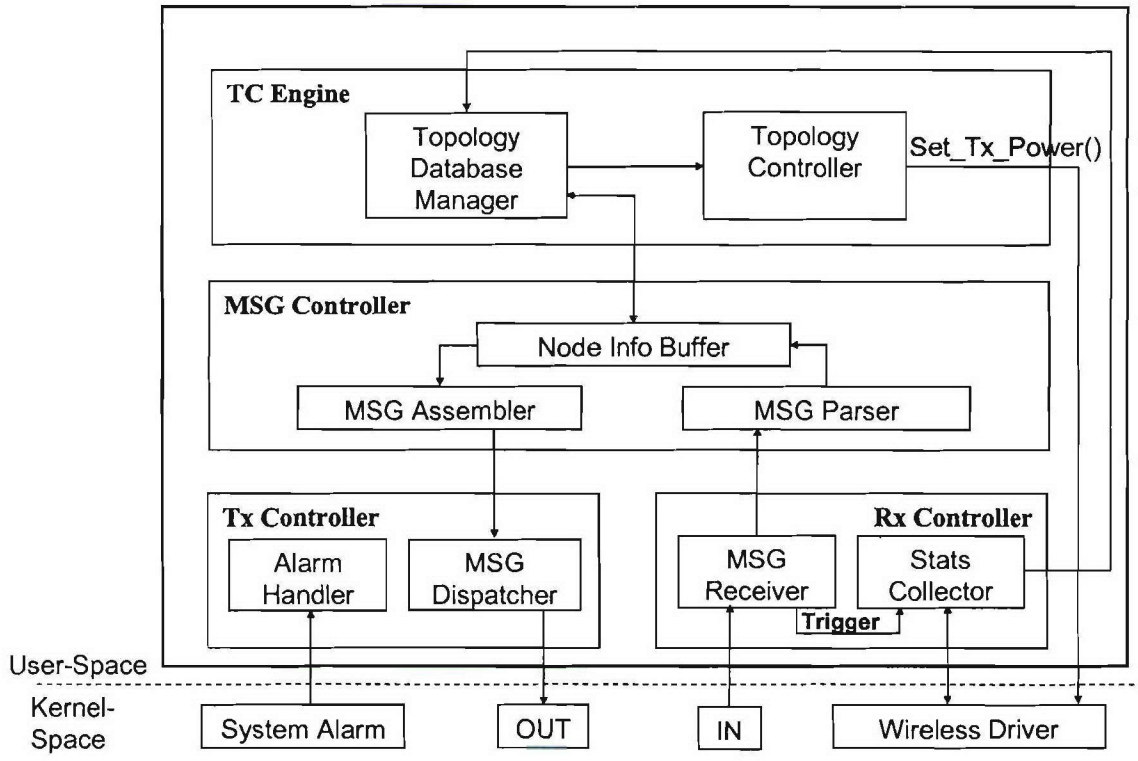



**Figure 2.1-1** Implementation structure of the topology control mechanism.

Figure 2.1-1 shows the implementation structure of the TC mechanism. It is composed of four main modules: (i) the TC Engine; (ii) the MSG Controller; (iii) the Tx Controller; and (iv) the Rx Controller. The TC Engine is made up of the topology database manager and the topology controller. The topology database manager maintains information about the local neighborhood (node-related information, including a node's capabilities, and link information, such as directionality and weight). The topology controller implements the distributed TC algorithm based on data collected from the topology database manager. It calculates a localized topology graph and control a node's transmit power level by issuing commands directly to the wireless device driver. The MSG Controller temporarily stores node information exchanged between the TC Engine and the MSG Controller, and generates and analyzes TC messages. The TC messages hold information regarding a node's visible neighborhood and its TC capabilities. The Tx

Controller periodically broadcasts TC messages based on the operating system alarm handler. The Rx Controller processes TC messages and communicate the power level statistics of incoming packets to the TC Engine. The statistics are extracted from the wireless device driver.

The development of this mechanism requires a number of adjustments to interact dynamically with the wireless device driver. The Library of Efficient Data types and Algorithms (LEDA) will initially provide an existing implementation of a TC algorithm for the Topology Controller. We intend to assess its limitations and improve its performance. In addition, this investigation will enable us to identify generic issues based on observations of specific problems and provide useful guidance regarding topology control to the research community.

Links to other tasks: This subtask has natural synergies with Task 2.4 (Cross-Layer Optimization), as the mechanisms that support QoS in mobile ad hoc networks span the physical, data link, network, and application layers. It also integrates with Task 2.2 (Real-Time Resource Management, Communication, and Middleware) as some of the QoS mechanisms developed here will support real-time applications and must integrate with the real-time middleware developed in Task 2.2.

Schedule: The updated schedule for this subtask is as follows.

- Develop extended policy-based QoS mechanism (April-November 2005)
- Explore adaptability methods (July-December 2005)
- Demonstrate potential benefits of topology control in test bed (July-December 2005)
- Realize and integrate protocols using test bed (January-March 2006)
- Refine protocols based on performance evaluation and demonstrations (April-June 2006)

Personnel: The following personnel were assigned to this subtask during the quarter.

Luiz A. DaSilva, faculty (subtask leader)

Scott F. Midkiff, faculty

Waltemar de Sousa, GRA

*Subtask 2.1(b):* Security Mechanisms for Ad Hoc Environments

Task objectives: The objectives of this subtask are to investigate and, where feasible and deemed appropriate, develop security mechanisms that are efficient for ad hoc network environments. Our initial emphasis considers a distributed key management system (KMS) and associated shared trust schemes.

Accomplishments during reporting period: During the quarter, we continued testing and integration work of Key Management System (KMS), Openswan (which implements user space IPsec), and Linux kernel IPsec mechanisms with other network functions. The KMS dynamically distributes the certificates of the nodes throughout the network by utilizing Delegated Certificates Authorities (DCAs) and trusted peers. Any node in the network can establish security associations (SAs) by utilizing IPv4 and/or IPv6 addresses.

Links to other tasks: This subtask has synergies with Subtask 2.1(c) and Task 2.4 (Cross-Layer Optimization) as link layer and, especially, network layer information can be employed to improve key management and other security functions. We are working to deploy a prototype for evaluation in the test bed developed in Subtask 2.1(e) and use tools of Subtask 2.1(f).

Schedule: The schedule for this subtask is as follows. There is no change from the previous quarter.

- Develop DCA and trust management system (January-June 2005)
- Integrate cross-layer design features (July-September 2005)
- Realize prototype implementation (July-December 2005)
- Integrate protocols using test bed (January-March 2006)
- Refine protocols based on performance evaluation and demonstrations (April-June 2006)

Personnel: The following personnel were assigned to this subtask during the quarter.

Scott F. Midkiff, faculty (task leader)

George C. Hadjichristofi, post-doctoral associate

*Subtask 2.1(c):* Ad Hoc Routing Optimization

Task objectives: The objectives of this subtask are to investigate schemes to improve routing and to use network layer functionality to improve other network services.

Accomplishments during reporting period: We have extended and continue to extend the existing Naval Research Laboratory (NRL) implementation of OLSR by adding network-wide information dissemination capabilities. Information includes connectivity of every node and link quality metrics, such as packet drop rate. In addition, we developed a network information API that can access local routing information as well as information disseminated by the routing protocol. The API can extract topology and other link and node state information and provide the information to protocols and applications, typically at or above the networking layer. It can be accessed both locally and remotely via a client-server application that we developed.

Information that is of special immediate interest for the purpose of the AWINN integration task (Task 2.4) is connectivity to a particular node (i.e., reachability information) in a Boolean form and the path length (hop count) to a particular destination. Other information includes one-hop neighbor information for topology control calculations in Subtask 2.1(b), and network-wide topology and packet drop rate information for video applications in Subtask 2.1(d). Additional functionality may be added to the API and routing protocol based on needs and time and resources available.

Links to other tasks: This subtask has direct ties to Task 2.4 (Cross-Layer Optimization) as our focus makes the network layer a key part of our cross-layer optimization schemes. In addition, we will explore synergy with Task 2.2 (Real-Time Resource Management, Communication, and Middleware). We are deploying a prototype for evaluation in the test bed developed in Subtask 2.1(e) and use tools of Subtask 2.1(f).

Schedule: The updated schedule is as follows.

- Extend DSDV to support multi-channel MAC (January-March 2005)
- Extend OSPF-MCDS to support multi-channel MAC (April-June 2005)
- Extend Optimized Link State Routing (OLSR) to support multi-channel MAC (May-June 2005)
- Realize prototype implementation in Linux, including IPv6 support (July-November 2005)
- Provide enhanced support for policy-based network management (PBNM) (November-January 2005)
- Provide enhanced support for security services (October-December 2005)
- Integrate additional cross-layer enhancements (October-December 2005)
- Integrate protocols using test bed (January-March 2006)
- Refine protocols based on performance evaluation and demonstrations (April-June 2006)

Personnel: The following personnel were assigned to this subtask during the quarter.

Scott F. Midkiff, faculty (subtask leader)

Unghee Lee, GRA

George C. Hadjichristofi, post-doctoral associate

*Subtask 2.1(d):* Cross-Layer Approach for Routing of Multiple Description Video over Ad Hoc Networks

Task objectives: The objectives of this subtask are to investigate a theoretical foundation for cross-layer approaches for carrying video using Multiple Description (MD) coding over ad hoc networks and to build on this foundation to demonstrate key concepts via a prototype implementation.

Accomplishments during reporting period: We continued to investigate how to exploit path diversity in ad hoc networks to better support video communications. The video coding that we employ is called Multiple Description coding, a new video coding technique that is uniquely suitable for video transport over wireless ad hoc networks. We consider the problem of how to support video multicast with MD-coded video in ad hoc networks. Instead of just finding multiple paths in the network, we follow an application-centric, cross-layer routing approach with the objective of minimizing the overall video distortion. We propose an MD-coded video multicast scheme where multiple source trees are used. Furthermore, each video description is coded into multiple layers to cope with diversity in wireless link bandwidths. Based on this multicast model, we formulate cross-layer multicast routing as a combinatorial optimization problem and propose an efficient solution procedure.

During the quarter, we developed a strategy for integrating the video application with the test bed developed in Subtask 2.1(e). We are currently designing modules to enable this integration and upgrading our prototype implementation to operate in an IPv6 environment. The video application will obtain network information from the API developed as part of Subtask 2.1(c) and utilize accessed topology information to improve video quality through an innovative form of multi-path routing. Figure 2.1-2 shows how the video application will be deployed in the test bed. The video server and client are notebook computers, each connected to Gateway (GW) 1

and GW12, respectively. The default routes for these two notebooks are set to the corresponding GW's IP address. The topology and link parameters, controlled by the Dynamic Switch, are extracted by the routing protocols developed in Subtask 2.1(c) and are distributed to the video server. The video server utilizes a routing algorithm based on a genetic algorithm (GA) to take advantage of mesh connectivity and find a pair of paths from GW1 to GW12 for the video sessions.

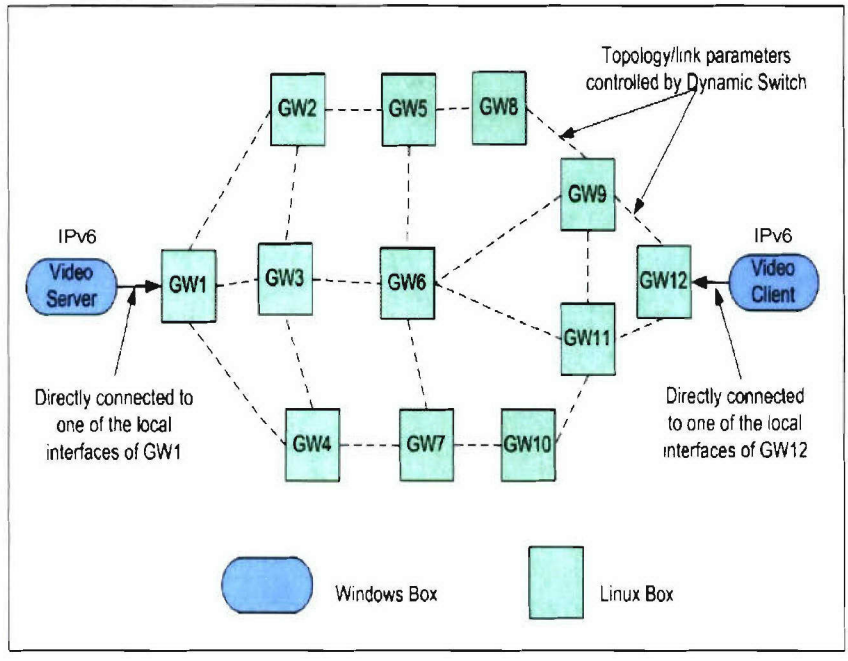



**Figure 2.1-2** Integration of the prototype video application integration in the test bed.

Links to other tasks: This subtask has direct ties to Task 2.4 (Cross-Layer Optimization) as it considers cross-layer optimization schemes that involve applications, in this case, video. We are deploying a prototype for evaluation and this will be integrated into the test bed developed in Subtask 2.1(e).

Schedule: The updated schedule is as follows.

- Develop foundation for cross-layer optimization (January-July 2005)
- Develop prototype system (June-November 2005)
- Integrate prototype system into interoperability test bed (December 2005-January 2006)
- Conduct experiments with interoperability test bed (February-April 2006)
- Refine protocols based on performance evaluation and demonstrations (May-June 2006)

Personnel: The following personnel were assigned to this subtask during the quarter.

Y. Thomas Hou, faculty (subtask leader)

Shiwen Mao, post-doctoral associate

Xiaojun Wang, GRA

*Subtask 2.1(e):* Test Bed Evaluation and Demonstration

Task objectives: The objectives of this subtask are to integrate and demonstrate through research prototype implementations key ideas from Subtasks 2.1(a), 2.1(b), 2.1(c), and 2.1(d) and, as feasible and appropriate, from Task 2.2 (Real-Time Resource Management, Communication, and Middleware), Task 2.3 (Network Interoperability and Quality of Service), and Task 2.4 (Cross-Layer Optimization). The objective includes exploring interactions between different components and functions and to evaluate and demonstrate both functionality and performance.

Accomplishments during reporting period: As noted in descriptions of Subtasks 2.1(a) though 2.1(d), we continued to deploy and test components to support the evolution of the test bed. We are extending the OLSR protocol to disseminate network information over the entire network and we have developed an API to extract this information dynamically and provide it to software components in Subtask 2.1(a), 2.1(d), and Task 2.2.

Links to other tasks: The test bed evaluation and demonstrations rely on results from Subtasks 2.1(a), 2.1(b), 2.1(c), and 2.1(d), as well as Tasks 2.2, 2.3, and 2.4.

Schedule: The updated schedule for this subtask is as follows.

- Identify and clarify needs (July-September 2005)
- Acquire and deploy test bed hardware (October 2005-January 2006)
- Deploy technologies in test bed (October 2005-April 2006)
- Final performance evaluation and demonstrations (May-June 2006)

Personnel: The following personnel were assigned to this subtask during the quarter.

Scott F. Midkiff, faculty (subtask leader)

George C. Hadjichristofi, post-doctoral associate

Unghee Lee, GRA

*Subtask 2.1(f):* Configuration and Monitoring Tools

Task Objective: The objectives of this subtask are to investigate and develop software configuration and monitoring tools to facilitate network testing and demonstration.

Accomplishments during reporting period: There was no activity in this subtask. We intend to continue our investigation of non-SNMP network monitoring. A promising approach that we will investigate is the capability to execute specific monitoring through information that can be extracted from functionalities developed in Subtask 2.1(c). This would allow the test bed monitor to collect network information with little or no additional network overhead.

Links to other tasks: The tools support the test bed described above for Subtask 2.1(e).

Schedule: The updated schedule for this subtask is as follows.

- Identify and clarify needs (April-September 2005)
- Implement and test tools (October 2005-January 2006)
- Utilization and refinement of tools (February-June 2006)

Personnel: The following personnel were assigned to this subtask during the quarter.

Scott F. Midkiff, faculty (subtask leader)

George C. Hadjichristofi, post-doctoral associate

### *2.1.3 Importance/Relevance*

Ad hoc networks are of particular importance to the Navy and other Department of Defense (DoD) units because of their ability to be quickly configured and operate without infrastructure. Research in ad hoc networks to date has been dominated by solutions to particular, specific problems and not to general system and network infrastructure issues. This task focuses on making ad hoc network operate successfully as a system with efficient routing, the ability to offer quality of service, and the robustness and security required of military networks. We also examine the challenging problem of delivering video, specifically Multiple Description video, in an ad hoc network.

### *2.1.4 Productivity*

Journal publications (appeared during the quarter)

1. S. Mao, S. S. Panwar, and Y. T. Hou, "On minimizing end-to-end delay with optimal traffic partitioning," *IEEE Transactions on Vehicular Technology*, vol.55, no.2, pp.681-690, March 2006.
2. S. Mao, S. Kompella, Y. T. Hou, H. D. Sherali, and S.F. Midkiff, "Routing for concurrent video sessions in ad hoc networks," *IEEE Transactions on Vehicular Technology*, vol.55, no.1, pp.317-327, Jan. 2006.
3. S. Mao, X. Cheng, Y. T. Hou, and H. D. Sherali, "Multiple description video multicast in wireless ad hoc networks," *ACM/Kluwer Mobile Networks and Applications Journal (MONET)*, vol.11, no.1, pp.63-73, Jan. 2006.
4. Y. Shi, Y. T. Hou, H. D. Sherali, S. F. Midkiff, "Cross-layer optimization for routing data traffic in UWB-based sensor networks," *IEEE Journal on Selected Areas in Communications*.

Journal publications (accepted during the quarter)

1. Y. T. Hou, Y. Shi, J. Pan, A. Efrat, and S. F. Midkiff, "Maximizing lifetime of wireless sensor networks through optimal single-session flow routing," *IEEE Transactions on Mobile Computing*, to appear.
2. S. Mao, Y.T. Hou, X. Cheng, H.D. Sherali, S.F. Midkiff, and Y.-Q. Zhang, "Multi-path routing for multiple description video over wireless ad hoc networks," *IEEE Transactions on Multimedia*.
3. M. X. Gong, S. F. Midkiff, and S. Mao, "A cross-layer approach to channel assignment in wireless ad hoc networks," to appear, *ACM/Kluwer Mobile Networks and Applications Journal (MONET)*, to appear.

Conference publications (appeared during the quarter)

1. U. Lee, S. F. Midkiff, and T. Lin, "OSPF-MCDS-MC: A routing protocol for multi-channel wireless ad-hoc networks," *Proc. IEEE Communications and Networking Conference (CCNC)*, Jan. 2006, Las Vegas, NV, pp. 426-430.

Conference publications (accepted during the quarter)

None.

Book Chapters (accepted during the quarter)

1. M.X. Gong, S. Mao, S.F. Midkiff, and B. Hart, "Medium access control in wireless mesh networks," in *Wireless Mesh Networking: Architectures, Protocols and Standards*, Y. Zhang, J. Luo, and H. Hu (Editors), Auerbach Publications, CRC Press, to appear.

Presentations

1. S. F. Midkiff, "Information Infrastructure Assurance in an 'Infrastructure-less' Environment," Euro-Atlantic Symposium on Critical Information Infrastructure Assurance, Riva San Vitale, Switzerland, March 23-24, 2006.

Meetings Attended

1. National Science Foundation Global Environment for Networking Innovations (GENI) "Town Hall" Meeting, Arlington, VA, March 10, 2006.

Students supported

Waltemar de Sousa 01/01/06-03/31/06
Unghee Lee, 01/01/06-03/31/06

Faculty supported

Scott F. Midkiff, 01/01/06-03/31/06
Luiz A. DaSilva, 01/01/06-03/31/06
Y. Thomas Hou, 01/01/06-03/31/06

Staff and other personnel supported:

George C. Hadjichristofi, 01/01/06-03/31/06 (post-doctoral associate)
Shiwen Mao, 01/01/06-03/31/06 (post-doctoral associate)

## 2.2 Task 2.2 Real-Time Resource Management, Communications, and Middleware

This report discusses the progress of Task 2.2 during the fifth quarter – January through March, 2006.

### *2.2.1 Task Overview*

The objectives of Task 2.2 include:

(1) Develop time/utility function (TUF)/utility accrual (UA) scheduling algorithms for scheduling Real-Time CORBA 1.2's distributable threads with *assured timeliness properties* under failures. Develop distributable thread maintenance and recovery (TMAR) protocols that are integrated with such scheduling algorithms;

(2) Develop TUF/UA *non-blocking synchronization mechanisms* for synchronizing distributable threads and single-processor threads for concurrently and mutually exclusively accessing shared objects;

(3) Investigate how TUF/UA scheduling algorithms, synchronization mechanisms, and TMAR protocols can co-reside with policy-based network QoS management schemes, and jointly optimize (with network QoS schemes) UA timeliness optimality criteria, as envisaged in Task 2.3; and

(4) Develop the *Distributed Real-Time Specification for Java* (DRTSJ) standard under the auspices of Sun's Java Community Process (JCP)1, incorporating scheduling algorithms, synchronization mechanisms, and TMAR protocols developed in (1) and (2).

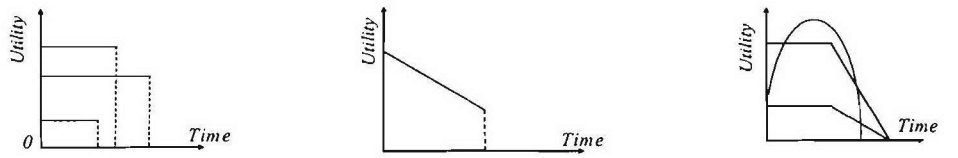
Embedded real-time systems that are emerging in areas such as control systems in the defense domain (e.g., Navy's DD(X), Air Force's AWACS) are fundamentally distinguished by the fact that they operate in environments with dynamically uncertain properties. These uncertainties include transient and sustained resource overloads due to context-dependent activity execution times and arbitrary activity arrival patterns. For example, many DoD combat systems include radar-based tracking subsystems that associate sensor reports to airborne object tracks. When a significantly large number of sensor reports arrives, it exceeds the system processing capacity, causing overloads that can lead to important tracks being undetected.

When resource overloads occur, meeting deadlines of all application activities is impossible as the demand exceeds the supply. The urgency of an activity is typically orthogonal to the relative importance of the activity—e.g., the most urgent activity can be the least important, and vice versa; the most urgent can be the most important, and vice versa. Hence, when overloads occur, completing the most important activities irrespective of activity urgency is often desirable. Thus, a clear distinction has to be made between the urgency and the importance of activities during overloads. (During under-loads, such a distinction need not be made, because deadline-based scheduling algorithms such as EDF are optimal for those situations [hor74]—i.e., they can satisfy all deadlines.)

---

1 The DRTSJ effort is currently ongoing under a JCP called JSR-50. The core members of the DRTSJ team include those from The MITRE Corporation and Virginia Tech.

Deadlines by themselves cannot express both urgency and importance. Thus, we consider the abstraction of time/utility functions (or TUFs) [jlt85] that express the utility of completing an application activity as a function of that activity's completion time. Utility is typically mapped to application-level quality of service (QoS) metrics such as track quality and track importance in a command and control application. We specify deadline as a binary-valued, downward "step" shaped TUF; Figure 2.2-1(a) shows examples. Note that a TUF decouples importance and urgency—i.e., urgency is measured as a deadline on the x-axis, and importance is denoted by utility on the y-axis.




**(a) Step TUFs** **(b) AWACS TUF** **(c) Air Defense TUFs**

**Figure 2.2-1** Example timing requirements specified using Time/Utility Functions.

Many embedded real-time systems also have activities that are subject to *non-deadline* time constraints, such as those where the utility attained for activity completion *varies* (e.g., decreases, increases) with completion time. This is in contrast to deadlines, where a positive utility is accrued for completing the activity anytime before the deadline, after which zero or infinitively negative utility is accrued. Figures 2.2-1(b)—2.2-1(c) show examples with such time constraints from two real applications (see [cjk+99] and the references therein).

When activity time constraints are specified using TUFs, which subsume deadlines, the scheduling criteria are based on accrued utility, such as maximizing sum of the activities' attained utilities. We call such criteria, *utility accrual* (or UA) criteria, and scheduling algorithms that optimize them, as UA scheduling algorithms. UA algorithms that maximize summed utility under downward step TUFs (or deadlines) [loc86, cla90, wrjb04] default to EDF during under-loads, since EDF can satisfy all deadlines during those situations. Consequently, they obtain the maximum total utility during under-loads. When overloads occur, they favor activities that are more important (since more utility can be attained from them), irrespective of their urgency. Thus, UA algorithms' timeliness behavior subsumes the optimal timeliness behavior of deadline scheduling.

The major Task 2.2 accomplishments of this quarter include developing: (1) an optimal multiprocessor real-time scheduling algorithm and (2) a distributable thread integrity protocol with bounded timeliness for recovery operations. We summarize these accomplishments in Section 2.2.2.

### *2.2.2 Task Activities for the Period:*

An Optimal Multiprocessor Real-Time Scheduling Algorithm

LREF Scheduling Algorithm

Model

We consider global scheduling, where task migration is not restricted, on an SMP system with $M$ number of identical processors. We consider the application to consist of a set of tasks, denoted $T=\{T_1, T_2, ..., T_N\}$. Tasks are assumed to arrive periodically at their releasing times $r_i$. Each task $T_i$ has an execution time $c_i$, and a relative deadline $d_i$ which is the same as its period $p_i$. The utilization $u_i$ of a task $T_i$ is defined as $c_i/d_i$ and is assumed to be less than 1. Similar to [da05,abd05], we assume that tasks may be preempted at any time, and are independent, i.e., they do not share resources or have any precedence.

We consider a non-work conserving scheduling policy; thus processors may be idle even when tasks are present in the ready queue. The cost of context switches and task migrations are assumed to be negligible, like in [da05,abd05].

Time and Local Execution Time Plane

In the *fluid* scheduling model, each task executes at a constant rate at all times [ha06]. The quantum-based Pfair scheduling algorithm, the only known optimal algorithm for the problem that we consider here, is based on the fluid scheduling model, as the algorithm constantly tracks the allocated task execution rate through task utilization. Pfair algorithm's success in constructing optimal multiprocessor schedules can be attributed to *fairness* --- informally, all tasks receive a share of the processor time, and thus are able to simultaneously make progress. P-fairness is a strong notion of fairness, which ensures that at any instant, no application is more than one quantum away from its due share (or fluid schedule) [bcpv96,cas01]. The significance of the fairness concept on Pfair's optimality is also supported by the fact that task *urgency*, as represented by the task deadline is not sufficient for constructing optimal schedules, as we observe from the poor performance of global EDF for multiprocessors.

Toward designing an optimal scheduling algorithm, we thus consider the fluid scheduling model and the fairness notion. To avoid Pfair's quantum-based approach, we consider an abstraction called the *Time and Local Execution Time Domain Plane* (or abbreviated as the T-L plane), where tokens representing tasks move over time. The T-L plane is inspired by the L-C plane abstraction introduced by Dertouzos *et al.* in [dm89]. We use the T-L plane to describe fluid schedules, and present a new scheduling algorithm that is able to track the fluid schedule without using time quanta.

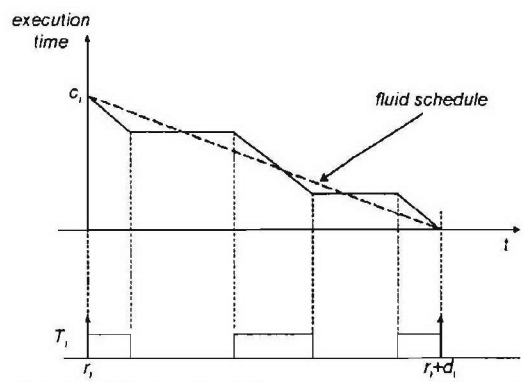



**Figure 2.2.2-1** Fluid schedule versus a practical schedule.

Figure 2.2.2-1 illustrates the fundamental idea behind the T-L plane. For a task $T_i$ with $r_i$, $c_i$ and $d_i$, the figure shows a 2-dimensional plane with time represented on the x-axis and the task remaining execution time represented on the y-axis. If $r_i$ is assumed as the origin, the dotted line

from (0, $c_i$) to ( $d_i$,0) indicates the fluid schedule, the slope of which is $-u_i$. Since the fluid schedule is ideal but practically impossible, the fairness of a scheduling algorithm depends on how much the algorithm approximates the fluid schedule path.

When $T_i$ runs like in Figure 2.2.2-1, for example, its execution can be represented as a broken line between (0, $c_i$) and ($d_i$,0). Note that task execution is represented as a line whose slope is -1 since x and y axes are in the same scale, and the non-execution over time is represented as a line whose slope is zero. It is clear that the Pfair algorithm can also be represented in the T-L plane as a broken line based on time quanta.

When $N$ number of tasks are considered, their fluid schedules can be constructed as shown in Figure 2.2.2-2, and a right isosceles triangle for all tasks is found between every two consecutive scheduling events. We call this as the T-L plane $TL^k$, where $k$ is simply increasing over time. The size of $TL^k$ may change over $k$. The bottom side of the triangle represents time. The left vertical side of the triangle represents a part of tasks' remaining execution time, which we call the *local remaining execution time*, $l_i$, which is supposed to be consumed before each $TL^k$ ends. Fluid schedules for each task can be constructed as overlapped in each $TL^k$ plane, while keeping their slopes.

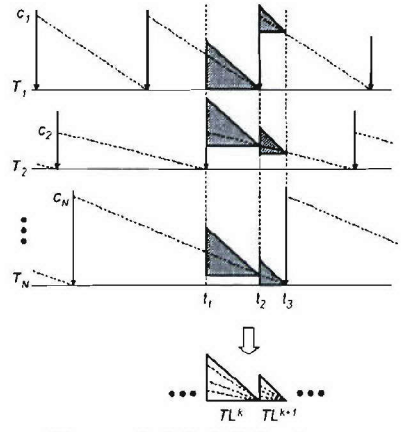



**Figure 2.2.2-2** T-L planes

Scheduling in T-L planes

The abstraction of T-L planes is significantly meaningful in scheduling for multiprocessors, because T-L planes are repeated over time, and a good scheduling algorithm for a single T-L plane is able to schedule tasks for all repeated T-L planes. Here, good scheduling means being able to construct a schedule that allows all tasks' execution in the T-L plane to approximate the fluid schedule as much as possible. Figure 2.2.2.-3 details the $k^{th}$ T-L plane.

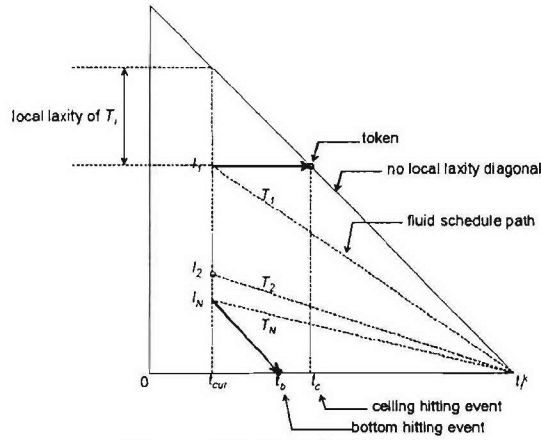



**Figure 2.2.2-3** $k^{th}$ T-L plane.

The status of each task is represented as a *token* in the T-L plane. The token's location describes the current time as a value on the horizontal axis and the task's remaining execution time as a value on the vertical axis. The remaining execution time of a task here means one that must be consumed until the time $t^k_f$, and not the task's deadline. Hence, we call it, *local* remaining execution time.

As scheduling decisions are made over time, each task's token moves in the T-L plane. Although ideal paths of tokens exist as dotted lines in Figure 2.2.2-3, the tokens are only allowed to move in two directions. When the task is selected and executed, the token moves diagonally down, as $T_N$ moves. Otherwise, it moves horizontally, as $T_1$ moves. If $M$ processors are considered, at most $M$ tokens can diagonally move together. The scheduling objective in the $k^{th}$ T-L plane is to make all tokens arrive at the rightmost vertex of the T-L plane---i.e., $t^k_f$ with zero local remaining execution time. We call this successful arrival, *locally feasible*. If all tokens are made locally feasible at each T-L plane, they are possible to be scheduled throughout every consecutive T-L plane over time, approximating all tasks' ideal paths.

For convenience, we define the *local laxity* of a task $T_i$ as $t^k_f - t_{cur} - l_i$, where $t_{cur}$ is the current time. The oblique side of the T-L plane has an important meaning: When a token hits that side, it implies that the task does not have any local laxity. Thus, if it is not selected immediately, then it cannot satisfy the scheduling objective of local feasibility. We call the oblique side of the T-L plane as *no local laxity diagonal* (or NLLD). All tokens are supposed to stay in between the horizontal line and the local laxity diagonal.

We observe that there are two time instants when the scheduling decision has to be made again in the T-L plane. One instant is when the local remaining execution time of a task is completely consumed, and it would be better for the system to run another task instead. When this occurs, the token hits the horizontal line, as $T_N$ does in Figure 2.2.2-3. We call it as the *bottom hitting event* (or event B). The other instant is when the local laxity of a task becomes zero so that the task must be selected immediately. When this occurs, the token hits the NLLD, as $T_1$ does in Figure 2.2.2-3. We call it as the *ceiling hitting event* (or event C). To distinguish these events from traditional scheduling events such as task releases and task departures, we call events B and C as *sub-events*.

To provide local feasibility, $M$ number of *largest remaining local execution time* tasks are selected first (or LREF) for every sub-event. We call this, the LREF scheduling policy. Note that the task having zero local remaining execution time (the token lying on the bottom line in the T-L plane) is not allowed to be selected, which makes our scheduling policy non work-conserving. The tokens for these tasks are called *inactive*, and the others with more than zero remaining local execution time are called *active*. At time $t^k_f$, the time instant for the event of the next task release, the next T-L plane $TL^{k+1}$ starts and LREF remains valid. Thus, the LREF scheduling policy is consistently applied for every event.

Algorithm Properties

A fundamental property of the LREF scheduling algorithm is its scheduling optimality---i.e., the algorithm can meet all task deadlines when the total utilization demand does not exceed the number of processors in the system. In this section, we establish this by proving that LREF guarantees local feasibility in the T-L plane.

Critical Moment

Figure 2.2.2.-4 shows an example of token flow in the T-L plane. All tokens flow from left to right over time. LREF selects $M$ tokens from $N$ active tokens and they flow diagonally down. The others which are not selected, on the other hand, take horizontal paths. When the event C or B happens, denoted by $t_j$ where $0<j<f$, LREF is invoked to make a scheduling decision.

We define the *local utilization* $r_{i,j}$ for a task $T_i$ at time $t_j$ as $l_{i,j}/(t_f-t_j)$, which describes how much processor capacity needs to be utilized for executing $T_i$ within the remaining time until $t_f$. Here, $l_{i,j}$ is the local remaining execution time of task $T_i$ at time $t_j$. When $k$ is cancelled, it implicitly means the current $k^{th}$ T-L plane.

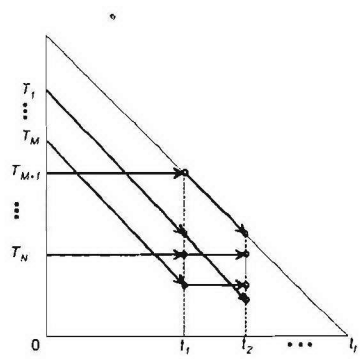



**Figure 2.2.2-4** Example of token flow.

**Theorem 2.2-1** [Initial Local Utilization Value in T-L plane]
Let all tokens arrive at the rightmost vertex in the $(k-1)^{th}$ T-L plane. Then, the initial local utilization value $r_{i,0}= u_i$ for all task $T_i$ in the $k^{th}$ T-L plane.

*proof* We omit the proof due space limits.

Well-controlled tokens, both departing and arriving points of which are the same to those of their fluid schedule lines in the T-L plane (even though their actual paths in the T-L plane are different from their fluid schedule paths), imply that all tokens are locally feasible. Note that we assume $u_i \leq 1$ and $\sum u_i \leq M$.

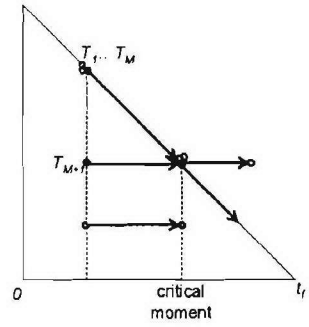



**Figure 2.2.2-5** Critical moment.

We define *critical moment* to describe the sufficient and necessary condition that tokens are not locally feasible. (Local infeasibility of the tokens implies that all tokens do not simultaneously arrive at the rightmost vertex of the T-L plane.) Critical moment is the first sub-event time when more than $M$ number of tokens simultaneously hit the NLLD. Figure 2.2.2-5 shows this. Right after the critical moment, only $M$ tokens from those on the NLLD are selected. The non-selected ones move out of the triangle, and as a result, they will not arrive at the right vertex of the T-L plane. Note that only horizontal and diagonal moves are permitted for tokens in the T-L plane.

**Theorem 2.2-2** [Critical Moment]
At least one critical moment occurs if and only if tokens are not locally feasible in the T-L plane.

*proof* We omit the proof due to space limits.

We define *total local utilization* at the $j^{th}$ sub-event, $S_j$, as $\sum_i^N r_{i,j}$.

**Corollary 2.2-3** [Total Local Utilization at Critical Moment]

At the critical moment which is the $j^{th}$ sub-event, $S_j > M$.

*proof* We omit the proof due to space limits.

From the task perspective, the critical moment is the time when more than $M$ tasks have no local laxity. Thus, the scheduler cannot make them locally feasible with $M$ processors.

Event C

Event C happens when a non-selected token hits the NLLD. Note that selected tokens never hit the NLLD. Event C indicates that the task has no local laxity and hence, should be selected immediately. Figure 2.2.2-6 illustrates this, where event C happens at time $t_c$ when the token $T_{M+1}$ hits the NLLD.

Note that this is under the basic assumption that there are more than $M$ tasks, i.e., $N>M$. This implicit assumption holds in Section Event C and Event B. We will later show the case when $N \leq M$.

For convenience, we give lower index $i$ to the token with higher local utilization, i.e., $r_{i,j} \geq r_{i+1,j}$ where $1 \leq i < N$ and all $j$, as shown Figure 2.2.2-6. Thus, LREF select tasks from $T_1$ to $T_M$ and their tokens move diagonally.

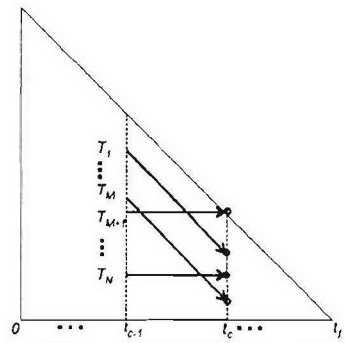



**Figure 2.2.2-6** Event C.

**Lemma 2.2-4** [Condition for Event C]

When $1 - r_{M+1,c-1} \leq r_{M,c-1}$, the event C occurs at time $t_c$, where $r_{i,c-1} \geq r_{i+1,c-1}$, $1 \leq i < N$.

*proof* We omit the proof due to space limits.

**Corollary 2.2-5** [Necessary Condition for Event C]

Event C occurs at time $t_c$ only if $S_{c-1} > M(1 - r_{M+1,c-1})$, where $r_{i,c-1} \geq r_{i+1,c-1}$, $1 \leq i < N$.

*proof* We omit the proof due to space limits.

**Theorem 2.2-6** [Total Local Utilization for Event C]

When event C occurs at $t_c$ and $S_{c-1} \leq M$, then $S_c \leq M$ for all $c$ where $0 < c \leq f$, and $r_{i,c-1} \geq r_{i+1,c-1}$, $1 \leq i < N$.

*proof* We omit the proof due to space limits.

Event B

Event B happens when a selected token hits the bottom side of the T-L plane. Note that non-selected tokens never hit the bottom. Event B indicates that the task has no local remaining execution time so that it would be better to give the processor time to another task for execution.

Event B is illustrated in Figure 2.2.2-6, where it happens at time $t_b$ when the token of $T_M$ hits the bottom. As we do for the analysis of event C, we give lower index $i$ to the token with higher local utilization, i.e., $r_{i,j} \geq r_{i+1,j}$ where $1 \leq i < N$.

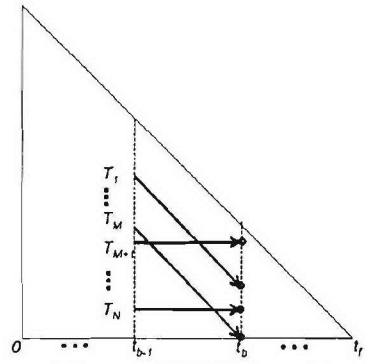


**Figure 2.2.2-7** Event B.

**Theorem 2.2-7** [Condition for Event B]

When 1- $r_{M+1,b-1} \geq r_{M,b-1}$, event B occurs at time $t_b$, where $r_{i,b-1} \geq r_{i+1,b-1}$, $1 \leq i < N$.

*proof* We omit the proof due to space limits.

**Corollary 2.2-8** [Necessary Condition for Event B]

Event B occurs at time $t_b$ only if $S_{b-1} > M\, r_{M,b-1}$, where $r_{i,b-1} \geq r_{i+1,b-1}$, $1 \leq i < N$.

*proof* We omit the proof due to space limits.

**Theorem 2.2-9** [Total Local Utilization for Event B]

When event B occurs at time $t_b$ and $S_{b-1} \leq M$, then $S_b \leq M$, where $r_{i,b-1} \geq r_{i+1,b-1}$, $1 \leq i < N$.

*proof* We omit the proof due to space limits.

Optimality

We now establish LREF's scheduling optimality by proving its local feasibility in the T-L plane based on our previous results. In Section Event C and Event B, we suppose that $N > M$. When less than or equal to $M$ tokens only exist, they are always locally feasible by LREF in the T-L plane.

**Theorem 2.2-10** [Local Feasibility with Small Number of Tokens]

When $N \leq M$, tokens are always locally feasible by LREF.

*proof* We omit the proof due to space limits.

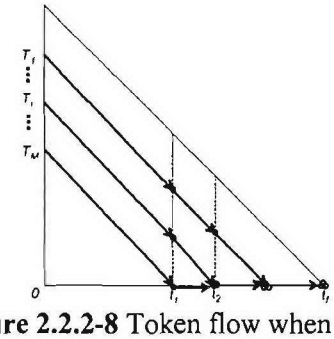


**Figure 2.2.2-8** Token flow when $N \leq M$.

Theorem 2.2-10 is illustrated in Figure 2.2.2-8. When the number of tasks is less than the number of processors, LREF can select all tasks and execute them until their local remaining execution times become zero.

We also observe that at every event B, the number of active tokens is decreasing. In addition, the number of events B in this case is at most $N$, since it cannot exceed the number of tokens. Another observation is that event C never happens when $N \leq M$ since all tokens are selectable and move diagonally.

Now, we discuss the local feasibility when $N>M$.

**Theorem 2.2-11** [Local Feasibility with Large Number of Tokens]

When $N > M$, tokens are locally feasible by LREF if $S_0<M$.

*proof* We omit the proof due to space limits.

When $N$ ($>M$) number of tokens are given in the T-L plane and their $S_0$ is less than $M$, event C and B occur without any critical moment according to Theorem 2.2-11. Whenever event B happens, the number of inactive tokens decreases until there are $M$ remaining tokens. Then, according to Theorem 2.2-10, all tokens are selectable so that they arrive at the rightmost vertex of the T-L plane with consecutive event B's.

Recall that we consider periodically arriving tasks, and the scheduling objective is to complete all tasks before their deadlines. With continuous T-L planes, if the total utilization of tasks $\sum_i^N u_{i,j}$ is less than $M$, then tokens are locally feasible in the first T-L plane based on Theorems 2.2-10 and 2.2-11. The initial $S_0$ for the second consecutive T-L plane is less than $M$ by Theorem 2.2-1 and inductively, LREF guarantees the local feasibility for every T-L plane, which makes all tasks satisfy their deadlines.

Algorithm Overhead

One of the main concerns against global scheduling algorithms (e.g., LREF, global EDF) is their overhead caused by frequent scheduler invocations. In [shab03], Srinivasan *et. al* identify three specific overheads:

> *Scheduling overhead*, which accounts for the time spent by the scheduling algorithm including that for constructing schedules and ready-queue operations;
>
> *Context-switching overhead*, which accounts for the time spent in storing the preempted task's context and loading the selected task's context; and
>
> *Cache-related preemption delay*, which accounts for the time incurred in recovering from cache misses that a task may suffer when it resumes after a preemption.

Note that when a scheduler is invoked, the context-switching overhead and cache-related preemption delay may not happen. Srinivasan *et. al* also show that the number of task preemptions can be bounded by observing that when a task is scheduled (selected) consecutively for execution, it can be allowed to continue its execution on the same processor. This reduces the number of context-switches and possibility of cache misses. They bound the number of task preemptions under Pfair, illustrating how much a task's execution time inflates due to the aforementioned overhead. They show that, for Pfair, the overhead depends on the time quantum size.

In contrast to Pfair, LREF is free from time quanta. However, it is clear that LREF yields more frequent scheduler invocations than global EDF. Note that we use the number of scheduler invocations as a metric for overhead measurement, since it is the scheduler invocation that contributes to all three of the overheads previously discussed. We now derive an upper bound for the scheduler invocations under LREF.

**Theorem 2.2-12** [Upper-bound on Number of Sub-events in T-L plane] When tokens are locally feasible in the T-L plane, the number of events in the plane is bounded within $N$+1.

*proof* We omit the proof due to space limits.

**Theorem 2.2-13** [Upper-bound of LREF Scheduler Invocation over Time] When tasks can be feasibly scheduled by LREF, the upper-bound on the number of scheduler invocations from time $t_s$ to $t_e$ is:

$$(N+1)\cdot\left(1+\sum_{i=1}^{N}\left\lceil\frac{t_e-t_s}{p_i}\right\rceil\right),$$

where $p_i$ is the period of $T_i$.

*proof* We omit the proof due to space limits.

Theorem 2.2-13 shows that the number of scheduler invocations of LREF is primarily dependent on $N$ and each $p_i$ --- i.e., more number of tasks or more frequent releases of tasks results in increased overhead under LREF.

Experimental Evaluation

We conducted simulation-based experimental studies to validate our analytical results on LREF's overhead. We consider an SMP machine with 4 processors. We consider 4 tasks running on the system. Their execution times and periods are given in Table 2.2.2-9 The total utilization is approximately 1.5, which is less than the number of processors. Therefore, LREF can schedule all tasks to meet their deadlines. Note that this task set's $\alpha$ (i.e., $max\{u_i\}$) is 0.818, but it does not affect the performance of LREF, as opposed to that of global EDF.

**Table 2.2.2-9** Task Parameters (4Task Set)

| Tasks | $c_i$ | $p_i$ | $u_i$ |
|---|---|---|---|
| $T_1$ | 9 | 11 | 0.818 |
| $T_2$ | 5 | 25 | 0.2 |
| $T_3$ | 3 | 30 | 0.1 |
| $T_4$ | 5 | 14 | 0.357 |

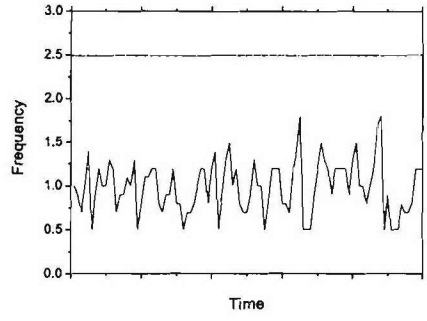



**Figure 2.2.2-10** Scheduler invocation frequency with 4 tasks.

To evaluate LREF's overhead in terms of the number of scheduler invocations, we define the scheduler invocation frequency as the number of scheduler invocations during a time interval $\Delta t$ divided by $\Delta t$. We set $\Delta t$ as 10. According to Theorem 2.2-13, the upper-bound on the number of scheduler invocations in this case is (4+1) $(1+\lceil 10/11 \rceil+\lceil 10/25 \rceil+\lceil 10/30 \rceil+\lceil 10/14 \rceil = 25$. Therefore, the upper-bound on the scheduler invocation frequency is 2.5.

In Figure 2.2.2-10, the upper-bound on the scheduler invocation frequency and the measured frequency are shown as a dotted line and a fluctuating line, respectively. We observe that the actual measured frequency respects the upper-bound.

Thus, our experimental results validate our analytical results on LREF's overhead.

## Distributable Thread Integrity Protocol with Bounded Recovery Time

### Distributed Thread Model

We consider Real Time Corba 2.0/Distributed Real Time Specification for Java's [RTC2/DRTSJ] distributable threads as our programming and scheduling abstraction. Details of this model can be found in [OMG01].

Distributable threads execute in local and remote objects by location-independent invocations and returns. A distributable thread begins its execution by invoking an object operation. The object and the operation are specified when the thread is created. The portion of a thread executing an object operation is called a thread segment. Thus, a thread can be viewed as being composed of a concatenation of thread segments.

A thread's initial segment is called its root and its most recent segment is called its head. The head of a thread is the only segment that is active. A thread can also be viewed as being composed of a

sequence of sections, where a section is a maximal length sequence of contiguous thread segments on a node. The first segment in the section results from an invocation from another node and the last segment in the section performs a remote invocation. Figure 2.2.2-11 cited from [ggcj95] illustrates threads, sections, and segments.

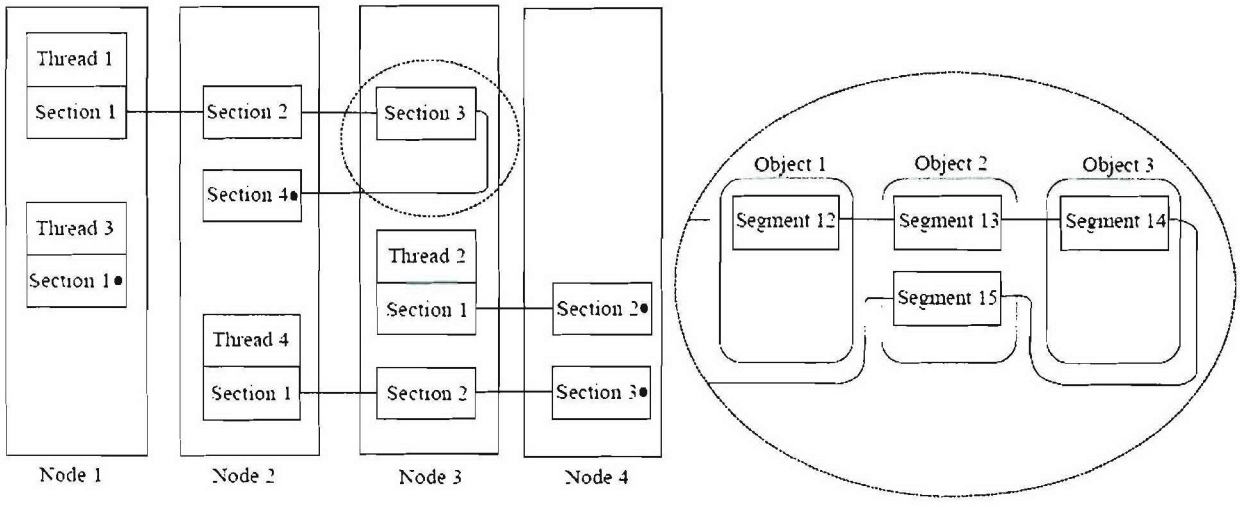



**Figure 2.2.2-11** Distributable threads, segments, and sections.

When nodes transited by distributable threads fail, this can cause threads that span the nodes to break by dividing them into several pieces. Segments of a broken thread that are disconnected from its root node are called orphans or unhealthy. For providing the abstraction of a continuous reliable thread, orphan segments of the thread must be detected and aborted, resources held by them must be released and rolled back to safe states, and a failure exception must be delivered to the farthest execution point of the surviving portion of the thread i.e., the farthest contiguous thread segment from the thread's root.

TP-TR Protocol

Thread Polling

The TP-TR TMAR protocol is largely based on the Alpha TMAR protocol described in [ggcj95]. The TP-TR protocol (referred to simply as the protocol) continually runs a three-phase polling operation, which provides the protocol with a view of the distributed threads within the system. In the first phase, the root node of a given distributed thread (DT) broadcasts a ROOT_ANNOUNCE message to all nodes within the system. In the second phase, all nodes that are hosting segments of that given DT respond to the ROOT_ANNOUNCE with a unicast SEG_ACK message. The root node then waits for a user-specified amount of time before determining the status of the DT (broken or unbroken). This status is based on the information it has received from the SEG_ACK messages. If the DT is determined to be unbroken, the root sends unicast SEG_HEALTH messages to all segments of the DT, refreshing them. If there is a break in the DT, the root node refreshes only the healthy (non-orphan) segments of a DT and spawns a recovery thread to deal with the break.

Recovery

The recovery thread is created so that the protocol can continue performing the three phase polling operation while performing recovery operations. This allows the protocol to recognize and deal with multiple breaks that occur within a system at the same time.

Recovering from a thread break requires at least four steps: pausing the DT and waiting for pause acknowledgement, determining which segment will be the new head, notifying the new head segment that it may continue to execute, and unpausing the distributed thread. In the first step, the recovery thread broadcasts a PAUSE message and waits for the node hosting the current head of the DT to respond with a PAUSE_ACK message. If a PAUSE_ACK is not received within a user-specified amount of time, the recovery thread automatically moves onto the second step of the recovery process. In the second step, the recovery thread analyzes its DT graph and finds the farthest contiguous thread segment from the DT's root. This segment will be the new head. If the old head still exists after this step, the recovery thread must terminate the old head and wait for an acknowledgement that this action has been completed. In the third step, the recovery thread sends a NEW_HEAD message to the node hosting the new head. In the fourth step, the recovery thread broadcasts an UNPAUSE message to all nodes within the system. The recovery thread then terminates. From here, the point of execution is at the new head and it becomes the responsibility of the application programmer to decide what should be done (continue/abort).

Orphan Cleanup

When a segment has not been refreshed for a specified amount of time it is flagged as an orphan and removed during orphan cleanup, which is performed periodically on all nodes within the system. When orphan cleanup is performed, a thread is spawned to determine which locally hosted segments, if any, are orphans. The thread then schedules the respective cleanup code to be run for each orphan and terminates. Orphan cleanup serves to both remove segments that follow a break in the DT (called thread trimming) and remove the entirety of threads that have lost their root.

Abort-assured Utility Accrual algorithm

In order to attain bounded recovery time for distributed threads, it is necessary to have a scheduling algorithm that can guarantee all portions of distributed threads within a system can be recovered from. Without this guarantee, it is possible for a broken thread to leave the system in an unsafe state. In order to facilitate this guarantee, we are developing the AUA scheduling algorithm, described below.

When a task/handler pair is introduced to the system, the scheduler first checks to see if the handler's execution can be guaranteed. If not, the task/handler pair is rejected and no new schedule is created. If a new handler is accepted, its last-chance time (LCT) is calculated by subtracting its WCET from its deadline, giving the scheduler an idea of the last moment the handler can be guaranteed to execute to completion.

When a new task/handler pair is accepted and a new schedule needs to be created, all handlers are first inserted into an EDF-ordered schedule. The normal tasks are then inserted into this schedule using the DASA algorithm. Once the schedule is created, the first entity (either task or handler) in the schedule is chosen for execution.

When a handler's LCT arrives without the handler's task having completed, the scheduler automatically wakes up and schedules the handler, thus guaranteeing that the handler is completed by its deadline.

### *2.2.3 Importance to the Navy*

We believe that the TUF/UA real-time technology developed in this task is directly relevant to DoD's network-centric warfare concept, Navy combatant systems including DD(x), and other DoD systems such as Air Force's next generation command and control aircrafts. In fact, the fundamental aspects of this class of real-time problems include:

(1) Need for transparent programming and scheduling abstractions for distributed computation workflows that are subject to time constraints
(2) Systems that are subject to significant run-time uncertainties that are often manifested in execution and communication times, and event and failure occurrences that are non-deterministically distributed
(3) Systems that are subject to transient and permanent overloads
(4) Need for time-critical and mission-oriented resource management (i.e., timely management of resources in the best interest of the current application mission)
(5) Need for industry/commercial standards- and COTS-based solutions for portability, robustness, and maintainability

All these aspects are directly addressed by Task 2.2 research. In particular, Real-Time CORBA 1.2's and DRTSJ's distributable threads abstraction provides a transparent programming and scheduling abstraction for distributed real-time computation workflows. Further, the class of TUF/UA scheduling algorithms, TMAR protocols, synchronization mechanisms, and policy-based network QoS management schemes target application activities, whose execution/communication latencies and event/failure occurrences are non-deterministically distributed and are subject to overloads. TUF/UA algorithms provide time-critical and mission-oriented resource management by (system-wide) scheduling to maximize system-wide accrued utility, where utility is mapped to application-level QoS. Consequently, utility maximization leads to managing system resources to maximize utility achieved for the users by the system. Furthermore, Task 2.2's work on the DRTSJ industry standard directly promotes industry/commercial standards and COTS-based solutions.

Thus, we believe that Task 2.2 research is directly relevant to Navy systems and other DoD systems.

DD(X) is currently using RTSJ, and is building a distributed real-time infrastructure using RTSJ. The DD(X) team has expressed significant interest in using DRTSJ – in particular, the distributable threads abstraction and end-to-end timing analysis capability. We believe that DD(X) can directly leverage DRTSJ's advanced adaptive time-critical (TUF/UA) resource management techniques, and DRTSJ's synergy with RTSJ.

References


[cla90] R. K. Clark, "Scheduling Dependent Real-Time Activities," PhD thesis, CMU CS Dept., 1990

[cjk+99] R. K. Clark, E. D. Jensen, et al., "An adaptive, distributed airborne tracking system," In *IEEE WPDRTS*, pages 353--362, April 1999

[hor74] W. Horn, "Some Simple Scheduling Algorithms," *Naval Research Logistics Quarterly*, 21:177--185, 1974.

[jlt85] E. D. Jensen, C. D. Locke, and H. Tokuda, "A time-driven scheduling model for real-time systems," In *IEEE RTSS*, pages 112--122, December 1985

[loc86] C. D. Locke, "Best-Effort Decision Making for Real-Time Scheduling," PhD thesis, Carnegie Mellon University, 1986

[wrjb04] H. Wu, B. Ravindran, E. D. Jensen, and U. Balli, "Utility Accrual Scheduling Under Arbitrary Time/Utility Functions and Multiunit Resource Constraints," *IEEE Real-Time Computing Systems and Applications*, April 2004

[srl90] L. Sha, R. Rajkumar, and J P. Lehoczky, "Priority inheritance protocols: An approach to real-time synchronization," *IEEE Trans. Computers*, 39(9):1175--1185, 1990

[kr93] H. Kopetz and J. Reisinger, "The non-blocking write protocol NBW", *IEEE RTSS*, 131--137, 1993

[cb97] J. Chen and A. Burns, "A fully asynchronous reader/writer mechanism for multiprocessor real-time systems," *Technical Report YCS-288*, CS Dept., University of York, May 1997.

[hps02] H. Huang, P. Pillai, and K. G. Shin, "Improving wait-free algorithms for interprocess communication in embedded real-time systems," *USENIX Annual Technical Conference*, pages 303--316, 2002

[arj97] J. H. Anderson, S.~Ramamurthy, and K. Jeffay, "Real-time computing with lock-free shared objects," *ACM TOCS*, 15(2):134--165, 1997

[crj05] H. Cho, B. Ravindran, and E. D. Jensen, "A space-optimal, wait-free real-time synchronization protocol," *IEEE ECRTS*, 2005.

[da05] U. C. Devi and J. Anderson, "Tardiness Bounds for Global EDF Scheduling on a Multiprocessor," *IEEE RTSS*, 2005

[abd05] J. Anderson and V. Bud and U. C. Devi, "An EDF-based Scheduling Algorithm for Multiprocessor Soft Real-Time Systems," *IEEE ECRTS*, 2005

[ha06] P. Holman and J. Anderson, "Adapting Pfair Scheduling for Symmetric Multiprocessors", *Journal of Embedded Computing*, To appear.

[bcpv96] S. Baruah and N. Cohen and C. G. Plaxton and D. Varvel, "Proportionate Progress: A Notion of Fairness in Resource Allocation," *Algorithmica*, 1996

[cas01] Abhishek Chandra and Micah Adler and Prashant Shenoy, "Deadline Fair Scheduling: Bridging the Theory and Practice of Proportionate-Fair Scheduling in Multiprocessor Servers," *Proceedings of the 21st IEEE Real-Time Technology and Applications Symposium*, 2001

[dm89] Michael L. Dertouzos and Aloysius K. Mok, "Multiprocessor On-Line Scheduling of Hard Real-Time Tasks," *IEEE Transactions on Software Engineering*, 1989

[shab03] A. Srinivasan and P. Holman and J. Anderson and S. Baruah, "The Case for Fair Multiprocessor Scheduling," *IEEE International Parallel and Distributed Processing Symposium*, 2003

[ggcj95] J. Goldberg, I. Greenberg, R. K. Clark, E. D. Jensen, K. Kim, and D. M.Wells, \Adaptive fault-resistant systems (chapter 5: Adpative distributed thread integrity)," Tech. Rep. csl-95-02, Computer Science Laboratory, SRI International, Menlo Park, CA., January 1995, http://www.csl.sri.com/papers/sri-csl-95-02/.

[OMG01] OMG, \Real-time corba 2.0: Dynamic scheduling specification," Tech. Rep., Object Management Group, September 2001, OMG Final Adopted Specification, http://www.omg.org/docs/ptc/01-08-34.pdf.

### *2.2.4 Productivity*

Journal publications

(1) H. Cho, B. Ravindran, and E. D. Jensen, "Space-Optimal Wait-Free Real-Time Synchronization," *IEEE Transactions on Computers*, Submitted March/April 2006

(2) P. Li, B. Ravindran, and E. D. Jensen, "Utility Accrual Real-Time Resource Access Protocols with Probabilistically Assured Individual Activity Timeliness Behavior," *IEEE Transactions on Computers*, Submitted March 2006

(3) H. Cho, B. Ravindran, and E. D. Jensen, "On Lock-Free Synchronization for Dynamic Embedded Real-Time Software," *ACM Transactions on Embedded Computing Systems*, Submitted January 2006

Conference publications

(1) C. Na, H. Cho, B. Ravindran, and E. D. Jensen, "Garbage Collector Scheduling in Dynamic, Real-Time Multiprocessor Systems," *2006 IEEE International Conference on Embedded and Real-Time Computing Systems and Applications (RTCSA)*, Submitted March 2006

(2) H. Cho, H. Wu, B. Ravindran, and E. D. Jensen, "On Multiprocessor Utility Accrual Real-Time Scheduling With Statistical Timing Assurances," *2006 IFIP International Conference on Embedded And Ubiquitous Computing (EUC)*, Submitted February 2006

(3) P. Li, B. Ravindran, and E. D. Jensen, "Utility Accrual Real-Time Resource Access Protocols with Assured Individual Activity Timeliness Behavior," *International Conference on Real-Time and Network Systems (RTNS)*, Poitiers, France, May 30-31, 2006, Accepted, to appear

(4) H. Cho, C. Na, B. Ravindran, and E. D. Jensen, "On Scheduling Garbage Collector in Dynamic Real-Time Systems With Statistical Timeliness Assurances," *IEEE International Symposium on Object and component-oriented Real-time distributed Computing (ISORC)*, Gyeongju, Korea, April 24-26, 2006, Accepted, to appear

(5) H. Cho, B. Ravindran, and E. D. Jensen, "Lock-Free Synchronization for Dynamic Embedded Real-Time Systems," *ACM Design, Automation, and Test in Europe (DATE), Real-Time Systems Track*, Munich, Germany, March 6-10, 2006

Students supported

Jonathan Anderson, January 2005 – present
Hyeonjoong Cho, January 2005 – present
Edward Curley, May 2005 – present
Chewoo Na, September 2005 – present

## 2.3 Task 2.3 Network Interoperability and Quality of Service

### *2.3.1 Overview*

Task Goal: The goal of Task 2.3 is to integrate network services (as investigated in Task 2.1) with real-time middleware (as investigated in Task 2.2). Specifically, we will investigate and develop methods and mechanisms to integrate policy-based quality of service (QoS) capabilities at the network level, and perhaps at the link layer, with real-time services offered by middleware.

Organization: This task is managed by Scott Midkiff and involves the following personnel:

Scott F. Midkiff, task director
Luiz A. DaSilva, faculty
Binoy Ravindran, faculty
George C. Hadjichristofi, post-doctoral research associate
Jonathan Anderson, graduate research assistant

Summary: Task 2.3 integrates results from Tasks 2.1 and 2.2. We have reproduced the basic network environment of Task 2.1 and utilized it for testing the components of Task 2.2. Additional components have been developed to support Task 2.2, as described in Subtask 2.1(c). Based on this initial integration we are making adjustments to our integration plans and updating the test bed being developed in Subtask 2.1(e). The following sections summarize subtasks and schedule.

### *2.3.2 Task Activities for the Period*

Task Objective: As stated in Section 2.3.1, the goal of Task 2.3 is to integrate network services (from Task 2.1) with real-time middleware (from Task 2.2).

Accomplishments during reporting period: We continued the application and middleware development for this integrated demonstration. A small test bed similar to the test bed being developed in Subtask 2.1(e) was configured and middleware testing is proceeding. A distributed single-ship version of the Naval Air Defense application has been implemented in Java and installed on the test bed. Current development effort is focused on extending the application to demonstrate a multi-ship scenario. We are also working on modifying the distributed real-time specification for Java (DRTSJ) applications programming interface (API) to support wireless Thread Maintenance and Repair (TMAR) implementations and exploit dynamic network information from Subtask 2.1(c).

Links to other tasks: This task integrates results from Task 2.1 and Task 2.2. It is also potentially synergistic with Task 2.4 (Cross-Layer Optimization) as it may be possible to integrate optimizations at the link and network layer with requirements presented by the real-time middleware.

Schedule: The revised schedule for this task is as follows.

- Plan integration approach (April-November 2005)

- Begin integration based on preliminary results (December 2005-January 2006)
- Integrate cross-layer design features (January-February 2006)
- Integrate protocols using test bed (March-April 2006)
- Refine protocols based on performance evaluation and demonstrations (May-June 2006)

Personnel: The following personnel participated in this subtask during the reporting period.

Scott F. Midkiff, task leader
Binoy Ravindran, faculty
George C. Hadjichristofi, post-doctoral research associate
Jonathan Anderson, graduate research assistant

### *2.3.3 Importance/Relevance*

Many military systems rely on real-time operation, but can often be characterized using "soft" real-time constraints. This work paves the way to providing real-time capabilities, based on time-utility functions (TUFs), in an ad hoc network environment.

### *2.3.4 Productivity*

There are currently no productivity items to report specifically for Task 2.3. Please see descriptions of related tasks.

## 2.4 Task 2.4 Cross-Layer Optimization

### *2.4.1 Overview*

Task Goal: The goal of this task is to investigate and develop methods and metrics to characterize and evaluate the interaction between physical, data link, network and application layer protocols. This will be accomplished through two specific applications (a) position location networks and (b) collaborative radio networks.

Organization: This task is managed by Dr. R. Michael Buehrer and Dr. Scott Midkiff.

Dr. R. Michael Buehrer, faculty
Dr. Scott Midkiff, faculty
Dr. Tom Hou, faculty
Qiao Chen, GRA
Swaroop Venkatesh, GRA
Jeong-Heon Lee, GRA

Summary: This quarter we focused on two subtasks: (a) Cross-layer design for UWB position-location networks and (b) collaborative radio networks. The latter sub-task has been broken down into two studies, the study of collaborative UWB networks and MAC-layer design for UWB networks.

### *2.4.2 Task Activities for the Period*

#### *2.4.2.1 Subtask 2.4.1a* Cross-Layer Design for Ultra-Wideband Position-Location Networks

Introduction: We continued our research efforts [AWIN3], [Venk06], [Venk06b] on the problem of location estimation in the absence of line-of-sight (LOS) between the unlocalized node and location-aware "anchor" nodes. Preliminary models and descriptions can be found in [AWIN3]. In this work, we present simulation results on NLOS mitigation in two-dimensional location estimation, assuming we are able to distinguish between LOS and NLOS range estimates. This assumption is justified in the case of ultra wideband (UWB) TOA-based ranging since LOS and NLOS signals can be identified by observing the delay spread statistics of received multipath profile. The RMS delay spread and mean excess delay can be used to distinguish between LOS and NLOS signal by hypothesis testing as illustrated in Figure 2.4-1.

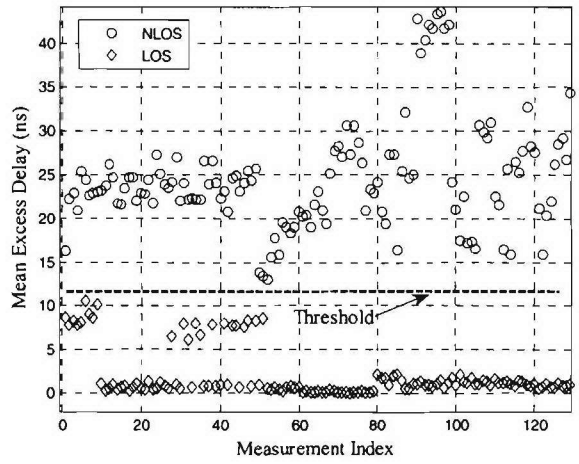



**Figure 2.4-1** Distinguishing between LOS and NLOS range estimates using the delay spread statistics of the received multipath profile. The data corresponds to indoor UWB measurements using Biconical antennas as part of the DARPA-NETEX project.

In the linear programming approach defined in [AWIN3], LOS range information is used to define both the objective function and the feasible region, whereas the NLOS range information is used only to define the feasible region. This allows the NLOS range estimates to "assist" in improving the accuracy of location estimates by limiting the size of the feasible region, but does not allow the NLOS bias errors to adversely affect node localization accuracy, since the NLOS range information plays no part in defining the objective function. The efficacy of the proposed method is demonstrated through simulation results in the following section. The proposed approach [AWIN3] works for any mixture of LOS and NLOS range estimates, provided $m_L \geq 3,\ m_N \geq 0$. We are currently working on extensions for the case where $m_L < 3,\ m_N \geq 1$

Simulation Results

In this section, we present simulation results that demonstrate that the proposed approach mitigates the effect of NLOS bias errors and utilizes the NLOS range information to improve node localization accuracy. In the following, the anchor nodes are randomly distributed over an $L \times L$ area where $L$ = 10 meters. The unknown location of the unlocalized node is $\mathbf{x} = [5 \quad 5]^T$ (meters). We compare the performance of three location-estimation approaches in terms of the mean and standard deviation of the localization error: (i) the proposed LP approach, (ii) the classic least-squares (LS) estimator, utilizing only LOS range estimates, while discarding the NLOS range estimates ("Pure-LOS") and (iii) the LS estimator, utilizing both LOS and NLOS range estimates, without the mitigation of NLOS bias errors ("LOS+NLOS").

For these three methods, the values of $\Omega = \left\|\mathbf{x} - \hat{\mathbf{x}}\right\|^2$ are computed for a large number of realizations of the measurement noise, bias errors and anchor locations. The mean $\mu_\Omega$ and the standard deviation $\sigma_\Omega$ are shown in Figure 2.4-2, for different values of the proportionality constant $K_E$ defined in [AWIN3]. In this simulation, $m_L$ = 3, $m_N$ = 3 and $B_{max}$ = 8 meters. As expected, in all three cases, node localization accuracy degrades as the variance of the range estimates increases (i.e., $K_E$ increases). The proposed LP approach outperforms the other two

schemes in terms of both the mean and standard deviation of the localization error, and therefore, on the average, produces more accurate node location estimates. In general, it was observed that for all three estimation procedures, $\mu_\Omega$ and $\sigma_\Omega$ follow similar trends in terms of their variation with $K_E$:

$$\mu_{\Omega,LP} < \mu_{\Omega,LS-Pure\ LOS} < \mu_{\Omega,LS-(LOS+NLOS)}$$
$$\sigma_{\Omega,LP} < \sigma_{\Omega,LS-Pure\ LOS} < \sigma_{\Omega,LS-(LOS+NLOS)} \qquad (2.4\text{-}1)$$

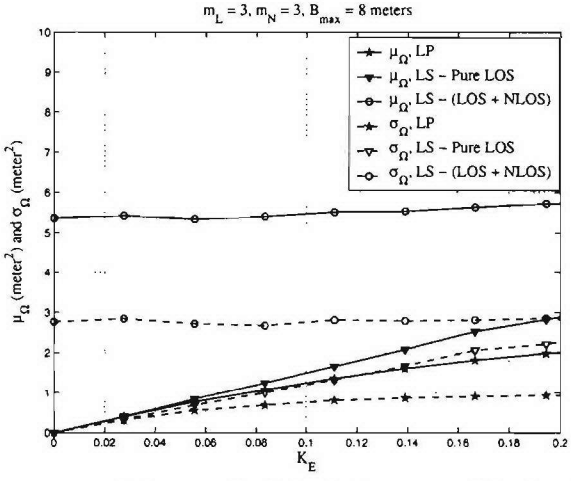



**Figure 2.4-2** The mean $\mu_\Omega$ and the standard deviation $\sigma_\Omega$ of the localization error $\Omega$ are plotted versus $K_E$. Here, $m_L = 3$, $m_N = 3$ and $B_{\max} = 8$ meters.

The variation of the mean localization error $\mu_\Omega$ with $K_E$, while increasing (a) the maximum bias $B_{\max}$, and (b) the number of NLOS range estimates $m_N$, is shown in Figure 2.4- and Figure 2.4- for a specific set of anchor locations. We observe that (a) the LP approach performs better than both the LS approaches and is less sensitive to an increase in the bias error, and (b) the performance of the LP approach improves as $m_N$ increases, whereas the opposite effect is observed with the LS estimator that utilizes LOS and NLOS range estimates without bias error mitigation. The former effect is due to the fact that the NLOS ranges do not contribute to the objective function of the linear program, while the latter is because

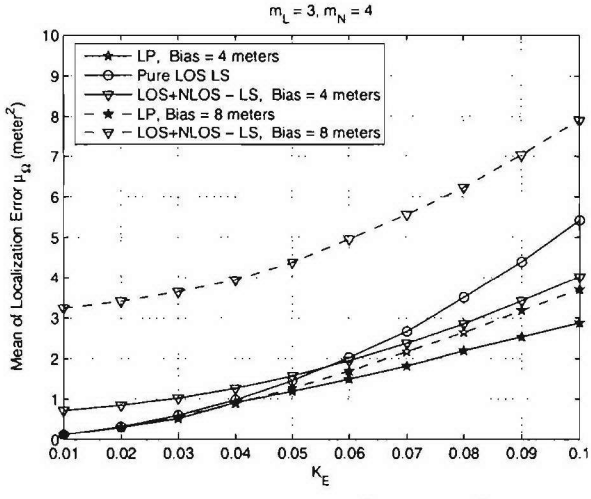



**Figure 2.4-3** Mean $\mu_\Omega$ of the Localization Error $\Omega$, $m_L = 3$, $m_N = 4$. The maximum bias $B_{\max}$ is increased from 4 meters to 8 meters.

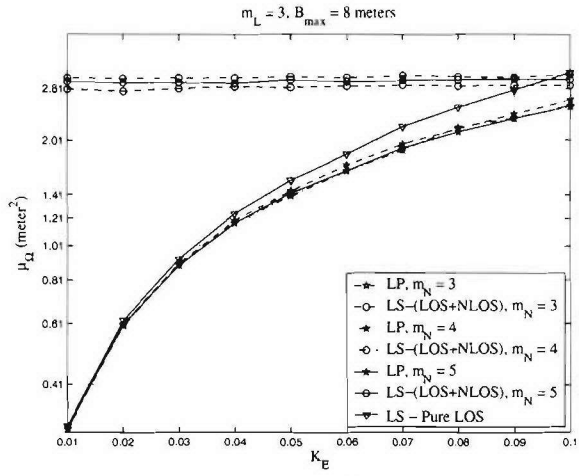



**Figure 2.4-4** Mean of the Localization Error, $m_L = 3$, $B_{\max} = 8$ meters. The number of NLOS range estimates is varied for $m_N = 3$ to $m_N = 5$.

additional NLOS range estimates reduce the size of the feasible region, thereby reducing the maximum possible values of the localization error. The LP approach once again outperforms the LS case that utilizes only LOS range estimates.

Simulation of a UWB PoLoNet

In order to evaluate the performance of the LP-based NLOS mitigation scheme, the accuracy of location estimates in a UWB PoLoNet was simulated. The network comprised $N_R$ = 50 anchors whose locations are known a priori and a single mobile node traveling at a speed $v$ = 5 meters per second. The region of interest is a 100 ×100 meter$^2$ area containing several obstructions as shown in Figure 2.4-5.

The effective received signal-to-noise-ratio (SNR) at the $i$th anchor corresponding to a transmission by the mobile node is modeled by $\xi_i = K_P P_T R_i^{\beta}$, where $P_T$ denotes the (constant) transmit power, $R_i$ is the distance between the mobile node and the $i$th anchor and $K_P$ is a constant that subsumes the effects of other physical layer parameters. Successful "ranging" is assumed to occur between the mobile node and the $i$th anchor when the SNR $\xi_i$ is larger than a threshold SNR $\xi_T$. Depending on the locations of the mobile node, anchors and obstructions, at any instant of time the mobile node may successfully obtain range estimates from both LOS and NLOS anchors. The path loss exponents for the LOS and NLOS cases are assumed to be $\beta_L$ and $\beta_N$ respectively. Therefore, at a given instant of time, the mobile node receives unbiased range estimates from LOS anchors that are within the radius

$$R_{\max,L} = \left(K_P P_T \xi_T^{-1}\right)^{\frac{1}{\beta_L}},$$

and biased range estimates from NLOS anchors that are within the radius

$$R_{\max,N} = \left(K_P P_T \xi_T^{-1}\right)^{\frac{1}{\beta_N}},$$

from the mobile's current location. The range estimates from LOS and NLOS anchors are assumed to be governed by models described in [AWIN3].

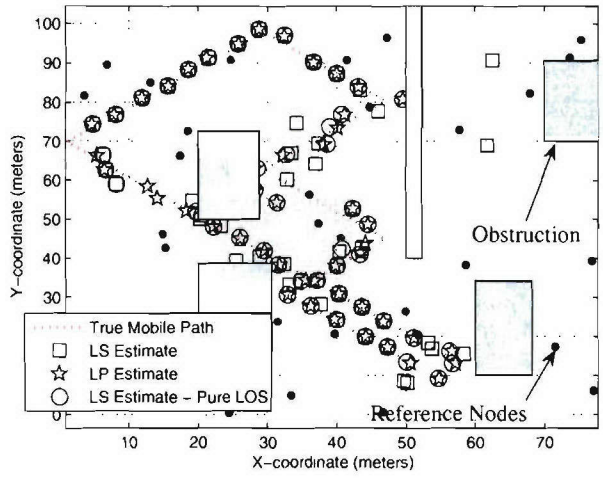



**Figure 2.4-5** Simulation of a UWB PoLoNet in a NLOS environment. The parameters used in this simulation are: $P_T = 1$ mW, $K_P = 10^5$, $\beta_L = 2$, $\beta_N = 2.5$ $K_E = 0.05$, $B_{\max} = 15$ meters. The total number of anchors is $N_R = 80$, and the mobile node moves at a speed of $v = 5$ meters/second through a 100×100 meter$^2$ area.

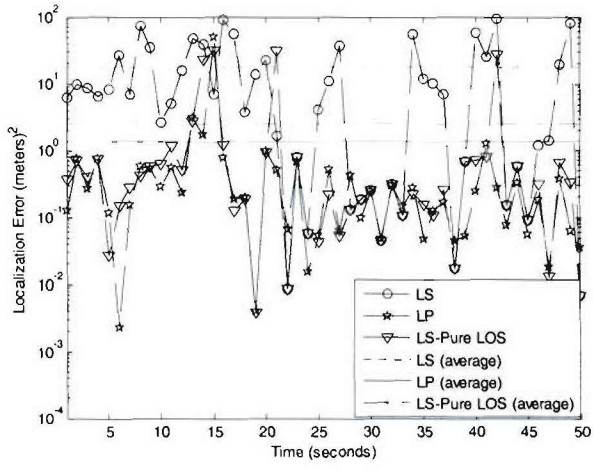



**Figure 2.4-6** A comparison of the LS-(LOS+NLOS), LS-(Pure-LOS) and the LP-based location estimators in terms of the localization error versus time.

Figure 2.4-6 compares the true location of a mobile node at a given instant of time with the location estimates computed using the LS-(Pure-LOS), LS-(LOS+NLOS) and LP approaches. The mobile node estimates its location (using the three estimation approaches) based on range information from anchors every second between $t = 0$ and $t = 50$ seconds. We see that the LP-based NLOS mitigation scheme outperforms the two LS-based schemes. This is also observed in Figure 2.4-6 which compares the localization error achieved by the three approaches versus time. We see that on the average, the LP-based NLOS mitigation scheme achieves higher localization accuracy than the LS based location estimators. In fact, the LP approach achieves approximately

an order of magnitude improvement with average error < $2m^2$ as compared to ~$20m^2$ for the LS technique.

Conclusions

We have investigated a novel linear-programming approach [AWIN3], [Venk06], [Venk06b] for the problem of node localization in NLOS environments. The main motivation for the development of this method is that in typical indoor position-location networks, it is likely that we will be required to compute a node's location using a mixture of LOS and NLOS range estimates. Using the LOS range estimates to define the objective function, and the NLOS range estimates to restrict the feasible region for the linear program, we showed that NLOS range information can be used to improve node localization accuracy without incurring performance degradation due to bias errors. This approach was shown to perform better than the standard LS estimator when a mixture of LOS and NLOS range estimates is provided. Relative to LS estimation, it was found that the proposed approach is less sensitive to an increase in NLOS bias errors and that increasing the number of NLOS range estimates improves node localization accuracy. The efficacy of the proposed method was demonstrated through simulation results for a UWB PoLoNet in a NLOS environment. Further, the proposed approach can be applied to a general three-dimensional location-estimation problem.

References

[AWIN3] Task 2.4, Cross-Layer Optimization, 3rd Quarter AWINN report.

[Venk06] S. Venkatesh and R. M. Buehrer, "A Linear Programming approach to NLOS error mitigation in Sensor Networks", *Proceedings of the Fifth International Conference on Information Processing in Sensor Networks (IPSN '06)*, pp. 301-308, 19th-21st April 2006, Nashville, USA.

[Venk06b] S. Venkatesh and R. M. Buehrer, "NLOS Mitigation In UWB Position Location Networks Using Linear Programming", *Invited Paper, to appear in the Proceedings of the IEE Seminar on Ultra Wideband Systems, Technologies and Applications*, 20th April 2006, London.

### *2.4.1.2 Subtask 2.4.1b* Cross-Layer Design of Cooperative UWB Networks

During this period, based on work from the previous quarter, we focused on how the application of optimal waveform adaptation techniques in the physical layer alleviates the design of the MAC layer. First, for distributed ad-hoc networks, simulation results show that by transmitting the optimal (in an SNR sense) sequence, with the help of an MMSE receiver, it is not necessary to assign an exclusion region to improve total throughput in an ad-hoc network. Second, due to the relationship between a link's SINR and its channel capacity, we derived an SINR expression for a centralized network; for distributed wireless networks, the SINR bound is still under investigation.

Accomplishments during reporting period: Recalling the simulation results from the previous report, waveform adaptation techniques were shown to exhibit the potential to improve overall network throughput when UWB waveforms are used at the physical layer. To better understand the interference mitigation capability of waveform adaptation, standard spreading codes were also investigated assuming the same network topologies for a fair comparison. The goal was to determine the additional advantage that optimal waveform design provides over classic spreading codes with known auto-correlation and cross-correlation properties. Both of these approaches focus on using the physical layer for interference mitigation. Moreover, the concept of the

"exclusion region" is examined where no transmitter can transmit in a certain area, hence alleviating interference via MAC layer design. The details of routing, exclusion region, optimization and optimal waveform adaptation techniques are given below.

MER and DIR Routing Protocols

Current literature for ad-hoc networks focus on setting up a routing table with or without given system loads. Due to the properties of an ad-hoc network, which lacks infrastructure, the steps followed for these routing protocols are as follows. First, the nodes must obtain the system topology, then paths are calculated using shortest-path algorithms. In our simulation, we assume that the geographic location of transmitters and receivers are known. Thus, the shortest path algorithm is the only thing that needs to be considered. Three algorithms were examined: Bellman-Ford, Dijkstra, and Floyd-Warshall algorithms. The first two calculate the path from multiple nodes to the destination, and the last one calculates the path of all nodes to all other nodes. Bellman-Ford obtains its path by iterating on the number of arcs in a path, Dijkstra iterates a path's length, (length has to be nonnegative), and Floyd-Warshall iterates on the set of nodes that are allowed as intermediate nodes on the path. Comparing these three, Dijkstra is the only suitable algorithm for our problem, and in our simulation we used it to obtain the shortest path for the minimum energy routing (MER) protocol. Moreover, the cost function is set according to the path loss model, and multiple hops are allowed for energy efficiency purposes. As a comparison, DIR routing doesn't consider the fading or path loss, instead directly sending the data to the destination in a single hop.

Exclusion Region

The implementation of an exclusion region is a somewhat new idea for wideband wireless systems, and has not been applied in narrowband (NB) systems. Due to the small bandwidth, the spectrum is easily divided into several channels to guarantee the performance of NB systems. However, for ad-hoc networks, multi-access interference is the key issue. Therefore the MAC layer design is extremely important to mitigate interference. For example, TDMA and FDMA mitigate interference by orthogonally assigning channels via different time slots or frequency slots. Furthermore, CDMA uses codes, cells (geographic exclusion region only for frequency reuse purpose) and time slots to solve the multi-access problem.

For applying an exclusion region to UWB, the concept itself is pretty straight forward. Basically, a geographical region is assigned around the receiver where no other transmitters can transmit to reduce the interference seen by that receiver. In our design, our target is to use waveform adaptation as a replacement for exclusion region in an attempt to achieve equal or better network throughput without the complexity of establishing exclusions regions.

Optimization Equations:

By solving the optimization equation sets in (2.4-2), we optimize the usage of time slots and the total network throughput is maximized. When comparing the optimal waveform to standard spreading codes, the only parameter that is different is the assigned waveform. Thus, a higher total network throughput means greater interference mitigation capabilities of that waveform. This is true because the total network throughput is directly a function of each channel's SINR.

$$\begin{aligned} &\text{Max} \quad \sum_{i=1}^{I} \log(f^i) \\ &s.t. Bf^n \le \sum_{n=1}^{L+1} w_n r^n \end{aligned} \tag{2.4-2}$$

$$r_l^n = K * SINR_l^n$$

$$\sum_{n=1}^{L+1} w_n = 1$$

$$\sum_{l:l.src=0} 1_{\{p_l^n>0\}} + \sum_{l:l.des=0} 1_{\{p_l^n>0\}} \le 1$$

$$P_l^n \le P_l^{MAX}$$

Note that in the above equations *n, l,B,f, r* represents the time slot, link, routing matrix, flow and data rate respectively, *w* is the duration of time slots, and *P* is the power of nodes.

Waveform Adaptation

The principle behind the optimal sequence algorithm is to design the transmit sequence based on the channel matrices and observed interference. The optimal *SINR* waveform is designed to mitigate channel interference in multiple access scenarios whereas the optimal *SNR* waveform is designed to maximize the captured energy in a single link. These two waveforms were originally designed for a centralized system which utilized an MMSE receiver. In this work, we have implemented them in a distributed ad-hoc network to combat interference and simplify the design of MAC protocol.

UWB Ad-Hoc Network Simulation Results

In the simulations, we examined the optimal SNR sequence, the SINR sequence and an MMSE receiver at the physical layer. At the MAC layer, we examined both assigning an exclusion region and not assigning an exclusion region. To have a fair comparison, we fixed the topology, routing and scheduling for the ad-hoc network and the spreading gain is set to be 127. For DS-UWB, a Rake receiver with 1- finger is used. Indoor non-line of sight (NLOS) channels are randomly assigned to each link of networks, based on channel impulse responses taken by the Mobile and Portable Radio Research Group (MPRG) at Virginia Tech.

Several techniques are compared and are referred to as algorithms 1 - 7:

1. Transmitters are assigned standard spreading codes (Gold or m-sequences), and Rake receivers with 10 fingers are used at the receiver.
2. Similar to algorithm 1, except that MMSE receivers are used.
3. Optimal SNR sequences are employed at the transmitter, and MMSE receivers are used at the receiver.
4. Similar to algorithm 3, but one of the concurrent flows chooses the optimal *SINR* sequence.
5. Similar to algorithm 4, but one of the concurrent flows chooses the optimal SINR sequence, and its receiver uses the MMSE algorithm.
6. Similar to algorithm 7, except that after one of the concurrent flow chooses the optimal SINR sequence, and its receiver updates the MMSE template, the other receivers update their MMSE templates.

**Table 2.4-1** The total throughput of UWB ad-hoc network ( nodes density 10 )

| Total Utility | Exclusion Region | Non Exclusion Region |
|---|---|---|
| 1.DS-UWB(Rake Receiver) | -5.7553 | -14.1980 |
| 2.DS-UWB(MMSE Receiver) | 2.0847 | 0.7772 |
| 3.SNR Seq. (MMSE Receiver) | 12.5048 | 12.7394 |
| 4.SNR+SINR+Matched filter | 10.9734 | 9.9558 |
| 5.SNR+SINR+MMSE(no update) | 11.7966 | 11.2571 |
| 6.SNR+SINR+MMSE(update) | 12.6095 | 12.9749 |

Conclusion

The simulation examined three techniques for mitigating multi-access interference in UWB ad-hoc networks: waveform design, MAC-layer based exclusion regions, and an MMSE receiver. Several conclusions are drawn as listed below:

- The MAC-layer technique of employing an exclusion region helps increase the total throughput of UWB ad-hoc networks in general. However, in algorithm 3 and algorithm 6, the implementation of an MMSE receiver alleviates the requirement of an exclusion region, and in fact achieved better throughput.
- Testing results in Table 2.4-1 show that an MMSE receiver works better than a Rake receiver in UWB ad-hoc networks as expected regardless of other techniques, with the penalty of implementation complexity.
- Although algorithm 6 provides superior results among all six algorithms, due to the complexity and computational load, algorithm 3 is the most practical since the throughput improvements of algorithm 6 over algorithm 3 are minor. Moreover, algorithm 3 reduces the number of time slots for the receiver to estimate and update multi-access channel interference.

SINR of Algorithm 3 in Centralized Systems

It is shown in Table 2.4-1 that the adoption of waveform optimization techniques improved total network throughput as compared to DS-UW. However, it didn't clearly show the interference mitigation capability of the waveform adaptation itself, without an MMSE receiver. The purpose of this section is to obtain an SIR expression when adopting an MMSE receiver in a centralized UWB system, and move on to the distributed system in the next reporting period.

First, we write the UWB signal model as

$$y(m) = \sum_{k=1}^{K} \mathbf{H_k S_k b_k} \sqrt{\mathbf{p_k}} + n(m) \qquad (2.4\text{-}3)$$

where $k \in \{1,..K\}$ indexes the multiple users, $H_k, S_k$, $b_k$ and $p_k$ are the channel matrix, signature sequence, data symbol, and transmit power of $k^{th}$ user respectively. Applying SVD decomposition, matrix $\boldsymbol{H}$ can be expressed as

$$H = \hat{U}\Lambda^{\frac{1}{2}}V^T; HS = \sqrt{\lambda_{max}}U \tag{2.4-4}$$

where $\lambda_{max}$ is the largest eigenvalue of the positive definite matrix $H^T H$, and $S$ is the corresponding eigenvector, $U$ is the corresponding column matrix of $\hat{U}$. Denoting matrix $P = diag\{P_1, P_2, ..., P_K\}$ and $D = diag\{E_d(U_1U_1^T), E_d(U_2U_2^T), \cdots E_d(U_kU_k^T)\}$, the expectation of $yy^T$ is

$$E_d(yy^T) = \sum_{k=1}^{K} E_d(p_k H_k S_k S_k^T H_k^T) + \sigma^2 I = \sum_{k=1}^{K} p_k \Lambda_k E_d(U_k U_k^T) + \sigma^2 I = \lambda \mathbf{PD} + \sigma^2 I \tag{2.4-5}$$

Without loss of generaltiy, the MMSE receiver for the first user can be written as

$$c = E_d(b_1^* y)E_d(yy^T) = (\lambda \mathbf{PD} + \sigma^2 I)^{-1}\lambda_1 U_1 \sqrt{P_1} \tag{2.4-6}$$

Then the SIR for $m^{th}$ user when adopting an MMSE receiver is

$$SIR_m = p_m S_m^T H_m^T (\sum_{j \neq m} p_j H_j S_j S_j^T H_j^T + \sigma^2 I)^{-1} H_m S_m = \frac{S_m^T H_m^T Z^{-1} H_m S_m p_m}{1 - S_m^T H_m^T Z^{-1} H_m S_m p_n} \tag{2.4-7}$$

where $\mathbf{Z} = \mathbf{HSPS^T H^T} + \sigma^2 \mathbf{I}$ and $\mathbf{H} = [H_1, H_2, ...H_k]$ and $\mathbf{S} = diag\{S_1, S_2, ..., S_k\}$. Using the matrix inversion formula, the inverse of the multi-access interference is

$$\mathbf{Z}^{-1} = \frac{\mathbf{I}}{\sigma^2} - \frac{\mathbf{HS}}{\sigma^4}(\mathbf{P}^{-1} + \frac{\mathbf{S^T H^T H X}}{\sigma^2})^{-1}\mathbf{S^T H^T} \tag{2.4-8}$$

Given the optimal SNR sequence, equation 2.4-7 is simplified into

$$\mathbf{Z}^{-1} = \frac{\mathbf{I}}{\sigma^2} - \frac{\mathbf{HS\Xi S^T H^T}}{\sigma^4} \tag{2.4-9}$$

where $\Xi = diag(\frac{p_1\sigma^2}{p_1\lambda_1 + \sigma^2}, \frac{p_2\sigma^2}{p_2\lambda_2 + \sigma^2}, , \frac{p_K\sigma^2}{p_K\lambda_K + \sigma^2})$. Combining (2.4-7) to (2.4-9), the SIR of $\boldsymbol{m^{th}}$ user is given in equation 2.4-9 and 2.4-10.

$$SIR_m = \frac{\beta_m}{1 - \beta_m} \tag{2.4-10}$$

$$\beta_m = \lambda_m U_m^T \frac{1}{\sigma^2}(I - \sum_{i=1}^{K} \frac{\lambda_i p_i U_i U_i^T}{p_i\lambda_i + \sigma^2})U_m p_m = \frac{p_m \lambda_m}{\sigma^2}(I - \sum_{i=1}^{K} \frac{\lambda_i p_i U_m^T U_i U_i^T U_m}{p_i\lambda_i + \sigma^2}) \tag{2.4-11}$$

Further Directions

In this report we have derived the SINR expression when adopting optimal SNR waveforms and MMSE receivers in centralized scenarios. In the next period, we would like to extend this work to distributed systems to obtain an asymptotic expression for SINR. Furthermore, since the

simulation results show the total network throughput of narrow-band ad-hoc network deceases with an increase in the network node density, while UWB ad-hoc network appear to trend in the opposite direction, we would like to further investigate this topic.

### *2.4.1.3 Subtask 2.4.1c* Cross-Layer Design of UWB Network MAC Layer

Introduction

Recent technological advances in wireless communications and networking have required more sophisticated medium access (MAC) protocols. In particular, for energy-constrained wireless networks, it is crucial to design the MAC scheme such that the unique physical layer (PHY) features of the underlying radio technology are fully exploited to provide an energy-efficient and robust networking infrastructure. In this subtask, we present an initial description of a proposed MAC protocol to efficiently connect distributed wireless sensors on the basis of the underlying impulse radio based ultra-wideband (IR-UWB) PHY. A wireless sensor network (WSN) is an emerging networking technology that enables unprecedented abilities of observing and understanding large-scale real world phenomena with high spatio-temporal resolution. Since most sensors are battery powered and often need to be autonomous and self-configurable in a hostile environment or surveillance area, the network system and protocol design should meet challenging demands such as low energy consumption, scalability, adaptability and reliability. Particularly, energy efficiency is a major protocol design concern since it often acts as a resource bottleneck in WSNs. Interestingly, as can be seen in Fig. 2.4-7, many of the needs can be satisfied by IR-UWB technology with unique PHY features such as precise positioning, resistance to multipath effects, power consumption and simple hardware design. These UWB PHY characteristics are all principal system design and performance criteria for WSNs. A main theme of our MAC design is to build a simple but robust medium access solution for UWB-based WSNs (UWB WSNs) while meeting the challenging demands of WSN applications based on unique UWB PHY attributes. To achieve this goal, we will try to bridge the gap between the underlying PHY issues and higher-level network system design. Through the initial analysis and simulation results, we conjecture that our VT-MAC protocol which relies on an adaptive impulse radio PHY will outperform existing MACs for WSNs in terms of energy efficiency, network throughput and delay. It is expected that the extensive comparative results of VT-MAC and existing WSN MACs will be shown to support our claim in the subsequent report.

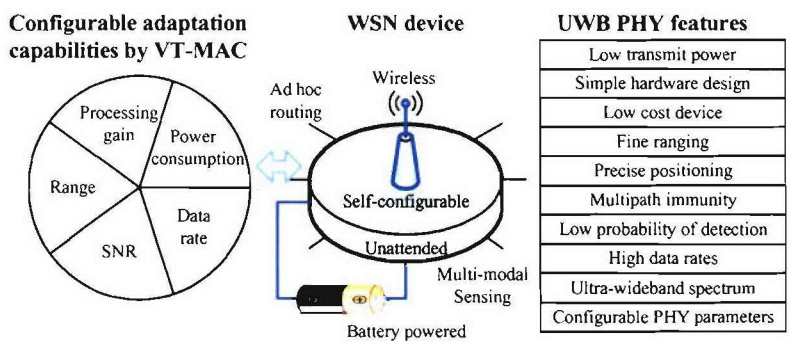



**Figure 2.4-7** WSN demands, UWB features and their matching.

Adaptive Impulse Radio

One of the crucial factors characterizing spread spectrum communication systems is the processing gain. Recently, researchers (particularly in the communications area) have suggested controlling the processing gain to adapt to time-varying channel conditions since a higher processing gain means stronger resistance capability to channel fading effects and interference. This improvement is typically enabled by using a longer PN sequence.

IR-UWB, which is a form of spread spectrum, inherently provides two types of processing gain. The first type is the gain obtained from redundant chips or pulses used for sending one information bit. This processing gain is similar but not identical to the conventional gain. The second type of processing gain is the average number of chip time slots between consecutive pulse transmissions termed the frame size in the UWB literature. The basis of adaptive impulse radio is formed from these two types of processing gain, thus enabling the radio to effectively trade data rate, transmit power and transmission range.

An important but quite unexplored UWB characteristic is configurable PHY system parameters associated with the processing gain, which are exposed to the higher layers. It is seen in a UWB signal model assuming binary time-hopping (TH) impulse radio for a node $k$ in the form

$$s_t^{(k)}(t) = \sqrt{\frac{E_b}{N_s^{(k)}}} \sum_{j=-\infty}^{\infty} \delta d^{(k)}_{\lfloor j/N_s^{(k)} \rfloor} w_t(t - jT_c N_h^{(k)} - c_j^{(k)} T_c) \tag{2.4-12}$$

where $E_b$ is the transmit bit energy, $N_s$ is the number of pulses per information bit $d$, $N_h T_c$ is the hopping frame time $T_f$, $N_h$ is the number of chips per frame, $T_c$ is the chip time slot duration, $c_j$ is the $j$th decimal code, and $\delta$ is the modulation index. IR-UWB, unlike conventional narrow-band and spread spectrum radios, provides more flexible PHY "control knobs" to dynamically trade the data rate, transmit power and radio range by software control.

To better understand the means that each node exploits this tradeoff, let us examine the SNR per bit in AWGN: $E_b^{(k)}/N_0 = P_{av} T_s^{(k)}/N_0 = P_{av} N_s^{(k)} T_f^{(k)}/N_0 = P_{sd} \beta^{(k)}/N_0$ where

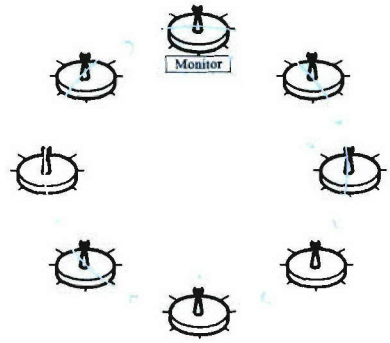



**Figure 2.4-8** Virtual token ring in VT-MAC.

$P_{av} = P_{sd}B_s$, $P_{sd}$ is the power spectral density (PSD) and $B_s$ is the signal bandwidth. $\beta^{(k)}$ is the total processing gain of the node $k$ and expressed as $B_s/R_s^{(k)} = B_s N_s^{(k)} N_h^{(k)} T_c \approx N_s^{(k)} N_h^{(k)}$ where $R_s^{(k)}$ is the symbol rate of the $k$th node. Assuming a fixed signal bandwidth (i.e., the average transmit power is constant due to PSD limits), we can increase the SNR per bit at the receiver, thus extending the range for the same SNR per bit, by augmenting $N_s$, which is the number of pulses per information bit (i.e., the first type of the processing gain). Equivalently, this increase results in a reduced data rate and, possibly, higher interference to adjacent nodes. Another way to increase the total processing gain is to either increase frame size $N_h$ (i.e., the second type of the processing gain), which is the cardinality of the hopping sequence for multiple access or to decrease pulse duration. This does not help to increase SNR but may reduce MAI and multipath effects, resulting in a better SINR. Notice that the processing gain and data rate will be adjusted linearly as $N_s$ or $N_h$ is tuned. In other words, by a simple means, we can adaptively control the underlying operational structures and parameters such as network topology, power consumption, data rate and transmission range according to the network variability. This variability caused by common events in WSNs such as node failures, the addition of new nodes, and location changes significantly impacts the network's reliability and energy consumption.

Due to the nature of spread spectrum signaling and unique PHY properties of UWB radio communications explained above, we believe that it is imperative to take a new approach across protocol layers for UWB-based WSNs. During the next report period, we will further study on these cross-layer adaptation issues of impulse radio which will be incorporated into our MAC design[1].

Virtual Token Ring Medium Access Control

The virtual token ring medium access control (VT-MAC) is proposed for distributed, dynamic and conflict free multi-user channel access for WSNs. The underlying PHY is IR-UWB that promises both reliable communication and multi-modal sensing capabilities as well as other unique PHY features. VT-MAC exploits the spread spectrum signaling nature of IR-UWB to form a logical token ring whereby concurrent packet transmissions by nodes in different rings can be possible. *Virtual* tokens, which represent PN codes for IR-UWB, are immune to critical MAC issues such as the hidden and exposed node problems, highly reducing the overhead of control packets. Moreover, we will incorporate the capability of adaptive impulse radio into VT-MAC to adapt to dynamic changes in network conditions and topology during the next report period.

I. Two Types of Virtual Tokens

Virtual tokens are key underlying components of our MAC protocol named the virtual token ring medium access control (VT-MAC) (see Fig. 2.4-8). Intrinsically, TH impulse radio must use time hopping pseudo-random noise (PN) codes to randomly locate pulses in certain time slots to deliver information while avoiding pulse collisions for multi-user channel access. Such a PN code acts as a virtual token in VT-MAC so that no additional overhead or delay is induced. Moreover, this scheme requires no handshaking control packets that cause high delay, throughput degradation, and energy waste especially in IR-UWB wireless networks due to its long acquisition time.

[1] We plan to include persuasive mathematical derivation and results reflecting the PHY adaptation capabilities of adaptive impulse radio

As seen from Fig. 2.4-9, there are two types of virtual tokens employed in VT-MAC: the virtual ring (VR) and virtual signature (VS) tokens. The VR token is used to identify each ring in which it should be

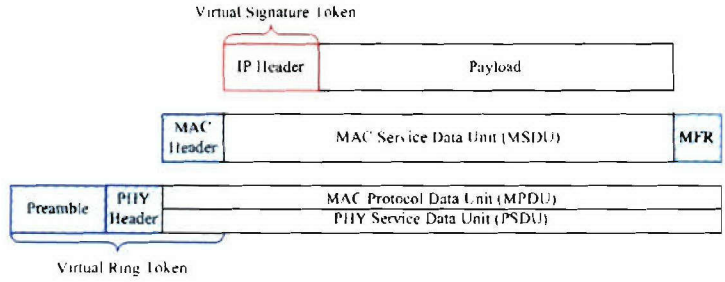



**Figure 2.4-9** Data packet structure including two virtual tokens.

grabbed by each node before the VS token is obtained for data transmission. Therefore, multiple transmissions on the same VS token in different virtual token rings can be possible.

II. Data Packet Structure

The data packet structure is shown in Fig. 2.4-9 where you can see how VR and VS tokens are used. The preamble and PHY header as well as the MAC header and footer (MFR) are spread with the VT token which is unique in each ring or spatially reused. The VS token is used to spread the IP header and thus nodes having both the assigned VT and VS information are allowed to acquire data packets of interest This method can effectively address the hidden and exposed node problems as well as the broadcast nature of the wireless medium. This is because the medium access scheme is conflict free in each ring but allows concurrent packet transmissions by nodes belong to different logical rings due to the spread spectrum PHY.

III. Code Monitor and VRC Packet Structure

A code monitor (CM) is selected by some routing protocol which may represent a parent in a routing tree or a dynamic cluster header. The CM has a role to monitor its ring and handle node failures or additions. It broadcasts the virtual ring control (VRC) packet to assign a PN code (i.e., $N_s$ and $N_h$) to each node involved in its ring formation. The figure is not included herein but we can expect a simple VRC packet structure that is spread with the VR token only, acquired by every node in a ring.

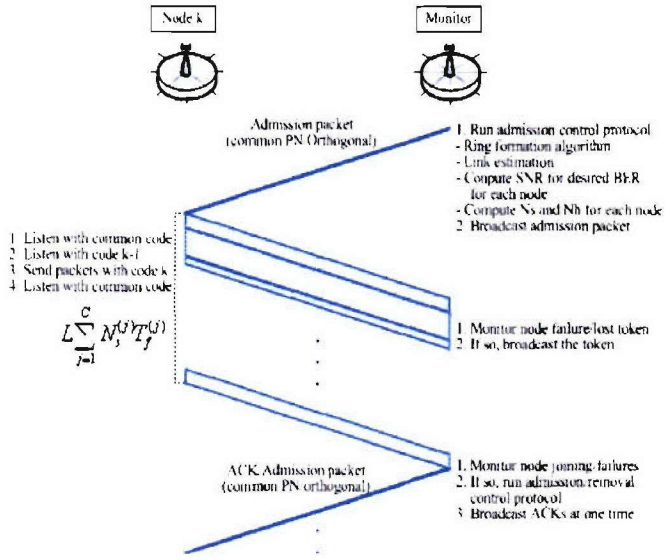



**Figure 2.4-10** Communication between a code monitor (CM) and node k.

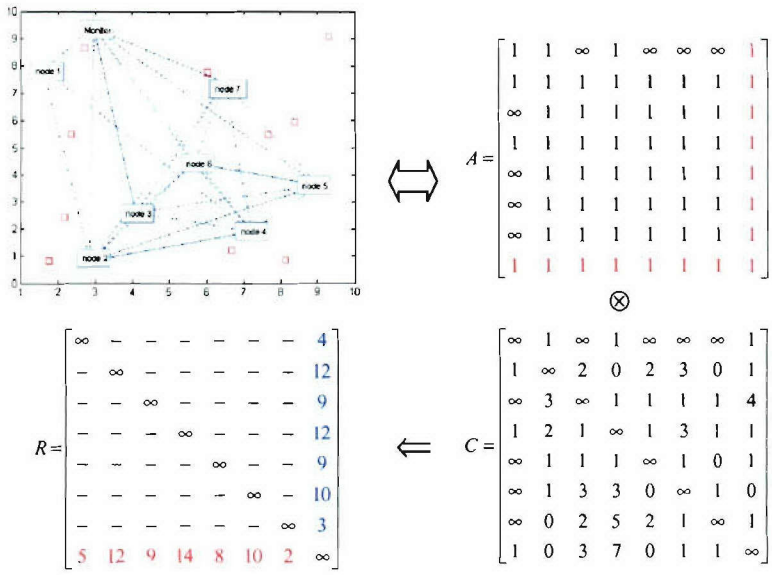
IV. How VT-MAC Works

With respect to wired local area networks (LANs), token-passing MAC protocols have been standardized for wired token-bus LANs (i.e., IEEE 802.4) and token-ring LANs (i.e., IEEE 802.5). Particularly, the token-ring MAC protocol was successful until high-speed switched Ethernet was developed in the early 1990s. It was known to be decentralized with a high efficiency. However, a physical token passing protocol inherently encounters critical issues such as additional overhead and delay, problems due to node failure and the multiple/lost token problems. In addition to these token-related problems, its wireless counterpart has been generally ignored due to the broadcast nature of the radio channel and highly unreliable link quality. Ergen et al. proposed a wireless token ring protocol (WTRP), where the token is a special control packet in 2002 and improved it in 2004 [Ergen04]. Despite their efforts of showing WTRP works by some analysis and simulation, it needs rather complex algorithms to resolve multiple and lost token problems as in the IEEE 802.5 as well as additional issues caused by the inherent characteristics of the radio channel. Even with this burden, their performance results show a little improvement over the IEEE 802.11 MAC.

In VT-MAC, virtual tokens (i.e., PN codes) are used, thus eliminating the token-related issues. Moreover, a node *k* only needs to acquire the predecessor's packet spread with a PN code *k-1* as a token. Thus, the token passing mechanism can be simply implemented and each node only needs to obtain the information about three PN codes dynamically: the common VR token code and two different VS token codes. Its data payload is spread with its default PN code, which is fixed during its entire operation. Figure 2.4-10 shows how nodes can communicate with the CM, and receive and then pass their tokens.

V. Ring Formation Algorithm and Cross-Layer Design

The core of VT-MAC is the ring formation algorithm which correctly forms a virtual ring. We will first show why the mechanism is distributed and reliable, and in subsequent work will prove that the algorithm is *correct*. For virtual ring formation, each node only needs to retain its local connectivity graph, which is easily obtained from the network layer. Nodes perform simple linear matrix multiplication of a local adjacency matrix and channel estimate matrix to produce a *ring formation matrix R* as



The resulting matrix is appropriately filtered to obtain a final ring vector used to configure the UWB PHY parameters (see Fig. 2.4-11). The values are determined to minimize transmit power as long as the application's requirements for BER and delay bounds are satisfied[3]. The cross-layer design plays a key role herein and the application needs to collaborate with the lower layers to achieve a desired QoS. In this connection, VT-MAC operating on adaptive impulse radio can provide the application layer a dynamic delay and throughput tradeoff curve over which an application can seek the optimal point. We will study this further in future work.

Performance Metrics for MAC Design

We introduce key performance metrics for MAC design with a particular emphasis on energy constraints. In the recent past, technological advances in wireless communications and networking have required more sophisticated medium access protocols, thus bringing a range of new approaches.

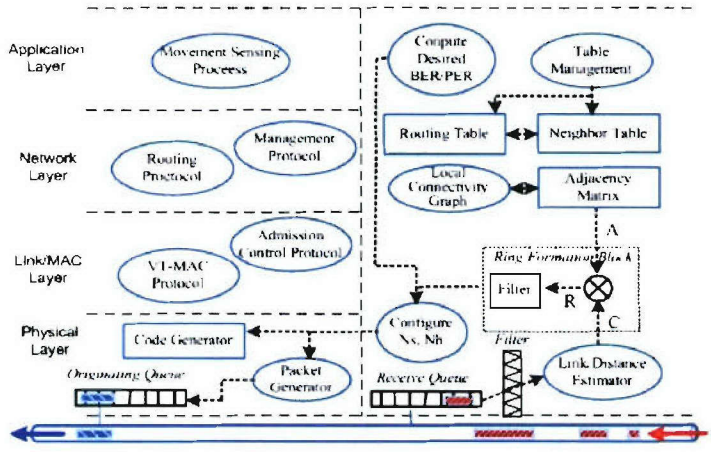



**Figure 2.4-11** Overall network protocol stack.

Especially with the minimum dependence on coordinators, the role of managing and controlling common network resources should be distributed to every node in a network. Therefore, a well-designed MAC protocol is too critical to increase the overall system performance while minimizing resource consumption.

The performance metrics used for MAC design in our investigation are: energy efficiency, network lifetime, aggregate data rate (or throughput), average data rate (or throughput), packet reception rate (or bit error rate), fairness, delay, and QoS provision in terms of a latency or throughput bound. Also their roles in enabling a network to be adaptable, self-configurable, flexible, and scalable are important design criteria. Through continuing analysis and simulations, we will show that VT-MAC can achieve the above metrics very closely for future work. In the following, we show some of the analysis and simulation results in the early evaluate stage.

Analysis and Simulation Results in the Early Evaluation Stage

Assuming fixed data packet size $L$=50 bytes and control packet size $L_c$=5 bytes, we get a channel capacity (i.e., maximum throughput) as

$$S_{\max}^{(\zeta)} = \frac{T^{(\zeta)}}{T^{(\zeta)} + \tau} = \frac{L/R_s^{(\zeta)}}{(L + L_c)/R_s^{(\zeta)}} \tag{2.4-13}$$

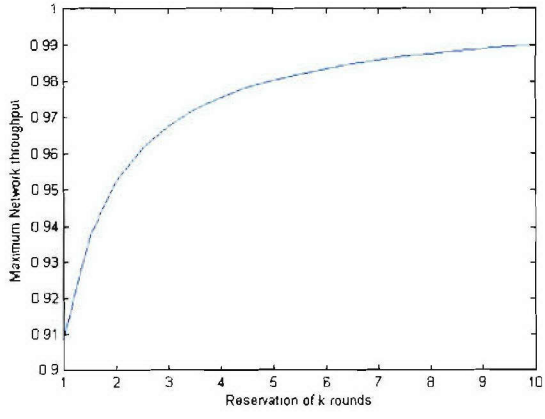



**Figure 2.4-12** Maximum network throughput vs. k rounds.

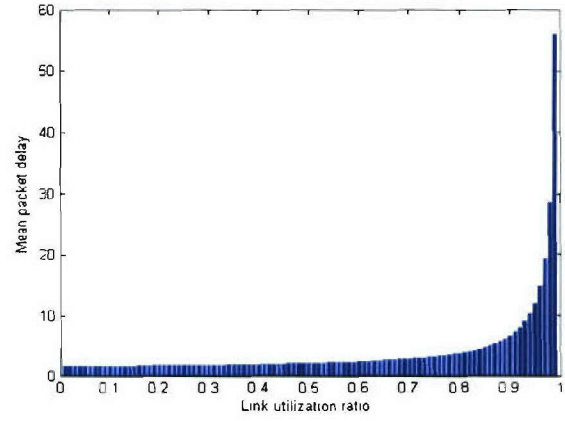



**Figure 2.4-13** Mean packet delay vs. link utilization rate.

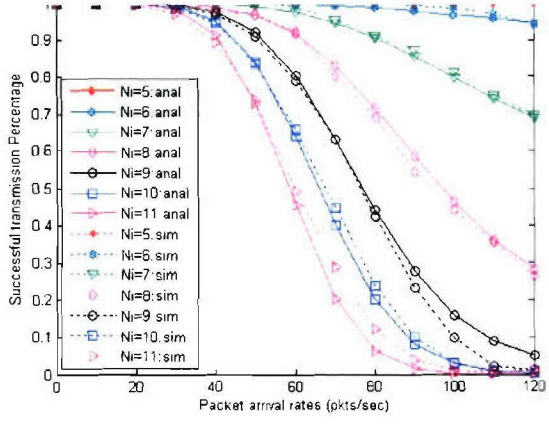



**Figure 2.4-14** Packet generation rates vs. packet reception rates.

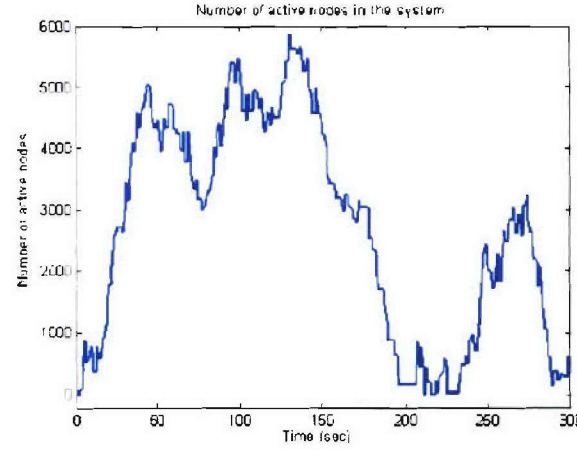



**Figure 2.4-15** Random number of active nodes in different rings but with overlapping transmission range, achieving almost perfect packet reception rates.

where $T^{(\zeta)}$ is the packet transmission time of a node $\zeta$. Recall that $R_s^{(\zeta)} = 1/N_s^{(\zeta)} N_h^{(\zeta)} T_c$. When the channel and network conditions are good, we may use the $k$ packet reservation scheme (i.e., $k$ runs over the entire ring without the controlling intervention by CM) and we have

$$S_{\max}^{(\zeta)} = \frac{kT^{(\zeta)}}{kT^{(\zeta)} + \tau} = \frac{kL/R_s^{(\zeta)}}{(kL + L_c)/R_s^{(\zeta)}} \tag{2.4.14}$$

The mean packet delay is computed as [Bert92]

$$\bar{D} = \frac{D}{T^{(\zeta)}} = (1+\alpha)\left[1 + \frac{1}{2(1-\rho^{(\zeta)})}\right] \tag{2.4-15}$$

where $\alpha = \tau/T$ and $\rho^{(\zeta)} = \lambda/\mu = L\lambda^{(\zeta)}/R_s^{(\zeta)}$, $\lambda^{(\zeta)}$ is the packet generation rate of the node $\zeta$. The above results are shown in Fig. 2.4-12 and Fig. 2.4-13. Figure 2.4-14 shows how many virtual rings can overlap without any packet error under near-worst cast scenarios with fixed values of $N_s$ and $N_h$. This MAI can be significantly reduced by adapting the impulse radio parameters to interference as shown in Fig. 2.4-15, where nodes are forced to be active at random but packet reception rates remain almost perfect throughout the simulation (not shown herein). This result implies that VT-MAC will be able to overcome co-ring interference by adaptively configuring the PHY parameters of impulse radio. We will also include more adaptation capabilities of impulse radio in the network variability such as dynamic changes in the network topology and channel condition.

Conclusion and Future Work

In this quarterly report, we presented a preliminary report on VT-MAC, a distributed, dynamic and conflict free multi-user channel access protocol for IR-UWB wireless sensor networks. VT-MAC uses two types of virtual tokens, VR and VS tokens, to spread data and VTC packets. The virtual tokens do not require any additional overhead and delay as well as token-related problems that we encounter in physical token passing protocols. We showed how VT-MAC resolves the hidden and exposed node problems, which appear inherently in the wireless medium. Traditionally, we addressed these issues by employing control packets such as RTS and CTS for contention-based MAC protocols or fixed scheduling time slots assigned centrally by a master node for conflict free MAC protocols. VT-MAC is distributed so that a dynamically chosen controller having the identical functionality (called the code monitor herein) needs to have minimal involvement in the virtual token passing.

We also introduced the concept of adaptive impulse radio and its role for MAC design. More detailed introduction and mathematical analysis demonstrating how impulse radio can adapt to dynamic link conditions and network topology will be done in future work. It is expected that we will show that the adaptive radio can optimize network lifetime and throughput by configuring its unique PHY parameters. We will also perform extensive analysis and simulations, and compare the results to existing MAC protocols proposed for WSNs, as well as developing crucial MAC mechanisms such as sleep scheduling.

References

[Scholtz97] R.A. Scholtz and M. Z. Win, "Impulse radio," in IEEE PIMRC'97, Helsinki, Finland, 1997.

[Win00] M. Z. Win and R. A. Scholtz, "Ultra-wide bandwidth time-hopping spread-spectrum impulse radio for wireless multiple access communications," IEEE Trans. Commun., vol. 48, no. 4, pp. 679–691, April 2000.

[Ergen04] M. Ergen, D Lee, R Sengupta, and P Varaiya, "WTRP - Wireless token ring protocol," IEEE Transactions on Vehicular Technology. 53 (6), pp. 1863-1881, 2004.

[Bert92] D. Bertsekas and R. Gallager, *Data Networks*, 2nd ed., 1992.

### *2.4.4 Productivity*

Journal publications

1. J. Ibrahim and R.M. Buehrer, "Two-Stage Acquisition for UWB in Dense Multipath," paper accepted, *IEEE Journal on Selected Areas in Communications*, Issue on Ultra Wideband Wireless Communications -- Theory and Applications, vol. 24, no. 4, pp. 801-807, April 2006.
2. J. Ibrahim, R. Menon, and R.M. Buehrer, "UWB Signal Detection Based on Sequence Optimization for Dense Multipath Channels," *IEEE Communications Letters*, vol 10, no. 4, pp. 228-230, April 2006.
3. J. Ibrahim and R.M. Buehrer, "NBI Mitigation for UWB Systems Using Multiple Antenna Selection Diversity," accepted for publication in *IEEE Transactions on Vehicular Technology*, April 2006.

Conference publications

1. J. Ibrahim and R.M. Buehrer, "A UWB Multiple Antenna System for NBI Mitigation under Rayleigh and Ricean Fading," paper accepted, *IEEE International Conference on Communication*, ICC 2006, June 2006.
2. J. Ibrahim and R.M. Buehrer, "A Modified Tracking Algorithm for UWB Pilot-Assisted Receivers," submitted to *International Conference on Ultra Wideband, ICUWB 2006.*
3. J. Ibrahim and R.M. Buehrer, "A Novel NBI Suppression Scheme for UWB Communications Using Multiple Receive Antennas," *IEEE Radio and Wireless Symposium, RWS 2006*, pp. 507 – 510, January 2006.
4. S. Ventkatesh, N. Kumar, and R.M. Buehrer, "A Spread-Spectrum MAC Protocol for Impulse-Radio Networks," *IEEE Vehicular Technology Conference*, September 2005.
5. S. Venkatesh and R. M. Buehrer, "Power-Control for UWB Position-Location Networks", accepted for publication, 2006 IEEE International Conference on Communications (ICC 2006), 11-15 June 2006, Istanbul, Turkey.
6. S. Venkatesh and R. M. Buehrer, "Multiple-Access Design for UWB Position-Location Networks", accepted for publication, 2006 IEEE Wireless Communications and Networking Conference (WCNC 2006), 3-6 April 2006, Las Vegas, USA.
7. S. Venkatesh and R. M. Buehrer, "A Linear Programming approach to NLOS error mitigation in Sensor Networks", accepted for publication, Fifth International Conference on Information Processing in Sensor Networks (IPSN '06), 19th-21st April 2006, Nashville, USA.

8. S.Venkatesh and R. M. Buehrer, "Multiple-Access Design for UWB Position-Location Networks", *Proceedings of the 2006 IEEEWireless Communications and Networking Conference* (WCNC 2006), 3-6 April 2006, Las Vegas, USA.
9. S. Venkatesh and R. M. Buehrer, "Power-Control for UWB Position-Location Networks", to appear in the Proceedings of the 2006 IEEE International Conference on Communications (ICC 2006), 11-15 June 2006, Istanbul, Turkey.
10. S. Venkatesh and R. M. Buehrer, "A Linear Programming approach to NLOS error mitigation in Sensor Networks", Proceedings of the Fifth International Conference on Information Processing in Sensor Networks (IPSN '06), pp. 301-308, 19th-21st April 2006, Nashville, USA.
11. S. Venkatesh and R. M. Buehrer, NLOS Mitigation in UWB Position Location Networks Using Linear Programming", Invited Paper, *Proceedings of the IEE Seminar on Ultra Wideband Systems, Technologies and Applications*, 20th April 2006, London, UK.
12. S. Venkatesh and R. M. Buehrer "Multiple-Access Insights from Bounds on Sensor Localization", to appear in the *Proceedings of the IEEE International Symposium on a World of Wireless, Mobile and Multimedia Networks*, Niagara-Falls, Buffalo-NY, 26th-29th June 2006.

Students supported

Qiao Chen, January. 1, 2005 – present
Swaroop Venkatesh, January. 1, 2005 – present
Jihad Ibrahim, January. 1, 2005 – present
Jeongheon Lee January 1, 2006-present

Faculty supported

R. Michael Buehrer, Jan. 1, 2005 – present
Scott Midkiff, Jan 1, 2005 - present

# 3. TASK 3 Visualization of Wireless Technology and Ad Hoc Networks

## 3.1 Overview

Task Objective: The objective of this task is to identify and investigate AWINN enabling technologies for the Close-in Sea Basing.

Organization: The task is directed by Ali Nayfeh and Rick Habayeb. The personnel list follows.

Rick Habayeb, faculty
Ali Nayfeh, faculty

Summary: The main activity during this period is the installation of the crane controller on a Shanghai Zenhua Port Machinery (ZPMC) quay-side container crane at Jeddah Port, Saudi Arabia. This will provide the bridge to transition the UWB ranging technology into the Sea Basing environment.

## 3.2 Task Activities for the period

During this quarter we had a golden opportunity to establish a potential transition path for the AWINN technologies into the Sea Basing environment. We successfully installed the VT controller on a Shanghai Zenhua Port Machinery (ZPMC) quay-side container crane at Jeddah Port, Saudi Arabia. The crane has a useable track of 100 meters, with a maximum trolley speed of 4.0 meters per second. The trolley is 45 meters above the pier. The hoist capacity is a maximum of 45 tons of cargo—the spreader bar is 15 tons—for a total of 60 tons, from -20 meters—into a ship-hatch below the pier—to 35 meters above the pier with a maximum hoist speed of 2 meters per second. The crane can lift either a single 8x8x40 ft container or two 8x8x20 ft containers at one time.

The controller has more than doubled the throughput of the average operator from approximately 25 containers per hour to 60 containers per hour. Considering a typical Panamax class container vessel has on the order of 4600 containers, this is a huge increase in performance.

The VT anti-sway controller is a feedback control system designed to reduce spreader-bar/container sway during and at the end of cargo transfer maneuvers. For the control system to work, the "sway angle" or the "pendulation angle" of the container must be accurately measured and fed-back to the control algorithm. Using these measurements, the controller modifies and corrects the operator joystick commands to the trolley motors. In a live, full-scale implementation on a quay-side container crane, a "contact" sway sensor must be rugged and able to withstand very large forces from multiple sources. In the Jeddah installation, cable rider-type sway sensors were used to monitor the spreader-bar/container sway at all times. These "contact" sway sensors measure the cable angles through mechanical linkages attached to the crane hoist cables.

Figure 3-1 shows the VT anti-sway controller installed on the quay-side container crane. The "Main CPU" houses the processing unit: a solid-state computer and power supply. The "Operator Panel" provides an interface to the operator.




**Figure 3-1** The "Main CPU" and "Operator Panels" mounted inside of the trolley cabin on the quay-side container crane at Jeddah Port.

The current generation of sensors is cable-rider type as seen in Figure 3-2. They utilize a drop arm attached to an absolute encoder for angle measurements. Due to the fact that the hoist cables are braided steel cables, there is tremendous wear-and-tear on the sensors. There is a pair of sensors per crane.

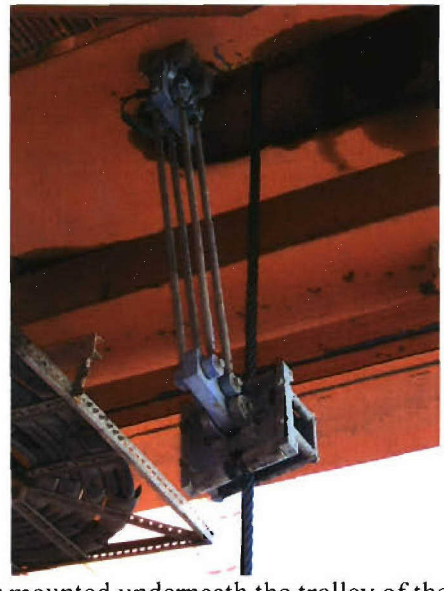


**Figure 3-2** A sway sensor mounted underneath the trolley of the quay-side container crane with hoist cable.

The hoist cable is threaded between spring-loaded pulleys seen in Figure 3-3. The pulleys are parts (1) and (2). Due to the abrasive nature of the braided hoist cable, the pulleys are supported by stainless steel plates at (3) and (4).

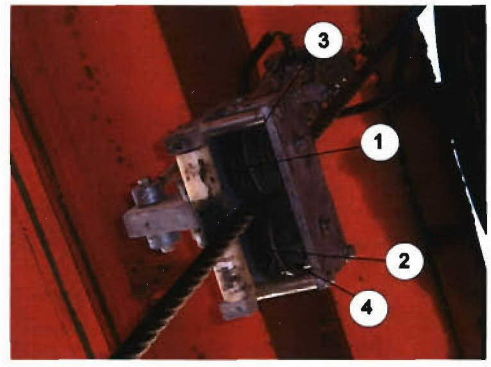



**Figure 3-3** A close up view of the sway sensor rider assembly showing the hoist cable and spring-loaded pulleys.

The wear-and-tear is clearly visible in Figure 3-4. The two nylon rollers (4) and (5) are used to keep proper alignment for the sensor-to-cable. Careful examination of (4) shows a deep gouge where the cable has eaten away at the roller. The expected lifetime of each roller is approximately 3 months. The process of replacing the roller requires a person to stand on top of the crane spreaderbar, suspended 45 meters above the ground. Then, nuts at (1) and (2) are removed. Part (3) is then removed. Parts (4) and (5) can now be replaced. Then part (3) is returned and rebolted with nuts (1) and (2).

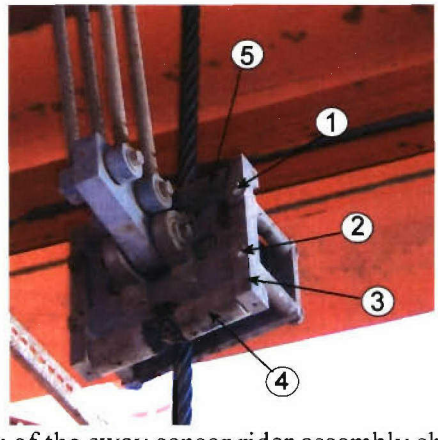



**Figure 3-4** A close up view of the sway sensor rider assembly showing the wear-and-tear on the rollers.

### 3.3 Importance/Relevance

ForceNet is the Navy implementation plan for Network Centric transformation. There are three fundamental concepts in ForceNet: Sea Shield, Sea Strike, Sea Basing. Sea Basing is projecting joint operational independence. There several technological challenges associated with the Navy vision for Sea Basing. The first major challenge is the Close-in command, control, and communication (C3). Currently, ship-to-ship Close-in C3 during UNREP is tedious, time consuming, archaic, and labor intensive. This project will explore, develop, visualize, and integrate the high payoff enabling AWINN technologies for the close-in sea basing environment.

### 3.4 Productivity

Publications

1. Z. N. Masoud, A. H. Nayfeh, and N. A. Nayfeh, "Sway Reduction on Quay-Side Container Cranes Using Delayed Feedback Controller: Simulations and Experiments," Journal of Vibration and Control. Vol. 11, No. 8, 1103-1122 (2005).

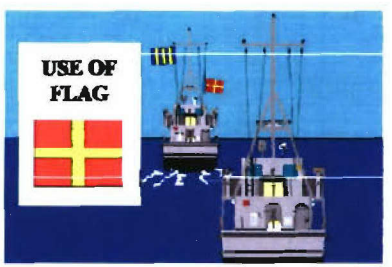
Students Supported

N. Nayfeh- January 25, 2005 to present
M.Daqaq – January 25, 2005 to present
O. Marzouk- January 25, 2005 to present

*Summary Quad Chart*

# AWINN Task 3 - Visualization of Wireless Technology and Network

- Day Time Communication




Technical Significance

To design and develop C3 using UWB sensors and Ad Hoc mesh networks

*Perform close-in ranging of cargo, ranging of ships during maneuver, and netting distributed sensors of a cluster of ships

•The close-in C3 will rely on the AWINN enabling technologies

Major Performers

Virginia Polytechnic Inst. and St. U.,
Dr. Rick Habayeb
Dr. Ali Nayfeh

Accomplishments and Approach

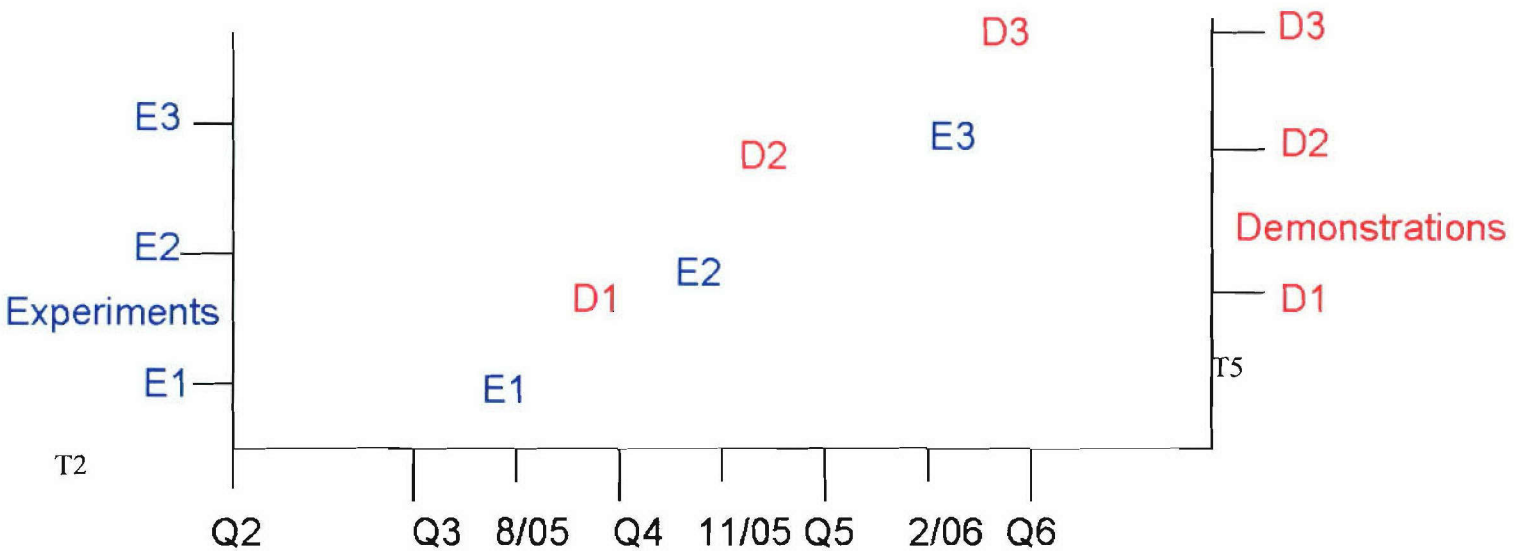
* Design and develop close-in C3
* Design and develop UWB cargo ranging sensors for soft pickup and landing of containers
*Design and develop UWB ship ranging Sensors and network
* Leverage and integrate AWINN wireless technologies and sensor networks to support the close-in Sea Basing missions

Impact

* Sea Basing missions require close-in C3 to transfer cargo and provide communication links. The AWINN provides the enabling technologies for the close-in sea basing missions.

*Timeline Chart*

## Task 3 - Visualization of Wireless Technologies in Sea Basing Environment




E1: Sensor fixed, Target moving

E2: Target and sensor moving

E3: 6 DOF Ranging

D1: Ranging technology

D2: Moving platform integration

D3: Crane integration

# 4. TASK 4 Testing and Demonstrations

## 4.1 TIP #1 Distributed MIMO UWB sensor networks incorporating software radio

Cooperative communication in energy-constrained networks is a topic of emerging interest in recent years especially for sensor network applications. We consider cooperative transmission from a cluster of nodes to a remote receiver. The transmission protocol used is randomized orthogonal space-time block coding (OSTBC) [1], which allow each node to randomly transmit one column of a given space-time code matrix. Previous work in [1] has shown that the scheme can achieve maximum possible diversity order for a given SNR as the number of cooperating nodes increases. Investigations in [2]-[5] looked at performance improvements in terms of capacity, energy efficiency, and average bit error rate (ABER) for several cooperative relaying strategies. However, all of the above-mentioned studies have ignored the effects of time synchronization errors which are inherent in practical systems. Simulations in [6] have shown that a distributed Alamouti system with 60% timing error can perform better than a perfectly synchronized SISO system under Rayleigh fading. In this paper, we examine the range improvement achievable under realistic conditions accounting for time synchronization errors. We use Gaussian approximation to evaluate the SINR at the receiver and then evaluate the corresponding range improvement. We show that the scaling of range as the number of nodes increase is not linear. It reaches a limit where increasing the number of nodes does not improve range.

A distributed MISO system is studied in this paper, where a group of nodes cooperate to form a transmit cluster. We assume perfect inter-cluster communication as the focus is on timing errors from distributed transmitters. A source transmits information to other nodes within the transmit cluster which then encode the symbols using STBC scheme and relay them to the receiver. The randomized STBC scheme is explained as follows. Assume an orthogonal space-time block code matrix $G$ with dimensions $p \times M$ where $p$ is the number of time slots used during transmission of the code block and $M$ is the number of columns. Let $N_T$ be the total number of cooperating nodes in the transmit cluster then, a group of $N_m$ nodes may choose to transmit the $m^{th}$ column of $G$ where $\sum_{m=1}^{M} N_m = N_T$. Orthogonal code matrix is chosen since it allows the code to maintain diversity benefits even when one of the columns is not transmitted.

Time synchronization errors in a distributed system can arise from multiple factors like lack of common reference driving the local oscillators of distributed transmitters, lack of tracking at the receiver for all the cooperative links and lack of compensation for propagation delays due to imperfect location prediction. Apart from these use of pulse shaping filters creates ISI when symbols are sampled incorrectly which in turn reduces the effective received signal power reducing the range improvement. In the following we briefly describe the system model and the analysis.

A BPSK system is considered where the received signal at the destination can be written as

$$\mathbf{r} = G\mathbf{h} + \mathbf{n} \qquad (4.1\text{-}1)$$

where $\mathbf{h} = [h_1 h_2 \ldots h_M]^T$ and

$$h_m = \sum_{i=1}^{N_m} h_{m,i} \qquad (4.1\text{-}2)$$

corresponds to the equivalent channel coefficient seen by the receiver corresponding to $m^{th}$ column of code matrix transmitted by $N_m$ nodes. It is also assumed that the channels between the distributed transmitters and the receiver are independent and undergo slow frequency non-selective fading. $\mathbf{n} \sim CN(0, N_0\mathbf{I})$ is AWGN noise at the receiver. To enhance the understanding of the effect of pulse shaping on the performance of range, we limit our analysis to the Alamouti scheme.

Due to symmetry considerations of the BPSK system considered, it will suffice to calculate one of the decision statistics at the output of the linear STBC decoder. The decision statistic $\hat{X}_1$ in expanded form is expressed as

$$\left[\hat{X}_1\right] = \Re\left\{\begin{bmatrix} h_{k,1}^* & -h_{k,2} \end{bmatrix}\begin{bmatrix} \sum_{m=1}^{2} h_{k,m}b_{k,m} + \sum_{j=1}^{N_T}\sum_{\substack{l=-\infty \\ l\neq k}}^{\infty} h_{l,j}b_{l,j}g_{k-l,j} + n_k \\ -\sum_{m=1}^{2} h_{k,m}^* b_{k+1,m} - \sum_{j=1}^{N_T}\sum_{\substack{l=-\infty \\ l\neq k+1}}^{\infty} h_{l+1,j}^* b_{l+1,j}g_{k-l-1,j} - n_{k+1} \end{bmatrix}\right\} \tag{4.1-3}$$

where $b_l$ is an independent random variable that represents transmitted binary data sequence taking values $\{1,-1\}$ with equal probabilities. $g_l$, representing $g(t)$ is the output at the receiver of the pulse shaped waveform used for symbol transmission. The subscripts $k$ and $l$ represent the symbol sampling time. $h_{k,m}$ represents $h_m$, the equivalent channel coefficient, at the $k^{th}$ symbol duration as defined in (4.1-1). $h_{l,j}$ is the channel coefficient corresponding to the $l^{th}$ time duration transmitted from $j^{th}$ transmit antenna. Now decoding the OSTBC block transmitted for $k^{th}$ symbol time duration (4.1-3) can be written as in (4.1-4); where $A$ is the desired part, $Z_1 \approx 0$, $Z_2$ and $Z_3$ are ISI terms and $\eta$ corresponds to the receiver noise at the decoder output. Next we evaluate the SINR due to ISI resulting from timing errors by applying Gaussian approximation. $\eta$ is a Gaussian random variable whose mean is zero and variance is given in (4.1-5):

$$\begin{aligned}\hat{X}_1 &= \left(|h_{k,1}|^2 + |h_{k,2}|^2\right)b_{k,1} + \Re\left\{\left(h_{k,1}^* h_{k,2} - h_{k,2}h_{k,1}^*\right)b_{k,2}\right\} \\ &\quad + \Re\left\{h_{k,1}^* \sum_{j=1}^{N_T}\sum_{\substack{l=-\infty \\ l\neq k}}^{\infty} h_{l,j}b_{l,j}g_{k-l,j}\right\} + \Re\left\{h_{k,2}\sum_{j=1}^{N_T}\sum_{\substack{l=-\infty \\ l\neq k+1}}^{\infty} h_{l+1,j}^* b_{l+1,j}g_{k-l-1,j}\right\} + \Re\left\{h_{k,2}n_k + h_{k,1}^* n_{k+1}\right\} \\ &= A + Z_1 + Z_2 + Z_3 + \eta\end{aligned} \tag{4.1-4}$$

$$\sigma_\eta^2 = \frac{\sum_{m=1}^{2} E\left\{\alpha_{k,m}^2\right\}}{2} = \frac{\sum_{i=1}^{N_T}\overline{\gamma}_i}{2} \tag{4.1-5}$$

where $\alpha_{k,m}$ is the amplitude process corresponding to $h_{k,m}$. From (4.1-2) the PDF of $h_{k,m}$ can be approximated as $CN\left(0,\sigma_i^2\right)$ for large values of $N_m$ where $\sigma_i^2 = \sum_{i=1}^{N_m}\overline{\gamma}_i$ and $\overline{\gamma}_i$ is the average received channel SNR for signal transmitted from $i^{th}$ node.

$Z_2$ can be expressed as

$$Z_2 = \alpha_{k,1} \sum_{j=1}^{N_T} \sum_{\substack{l=-\infty \\ l \neq k}}^{\infty} \alpha_{k,j} \cos\left(\theta_{l,j} - \theta_{k,1}\right) b_{l,j} g_{k-l,j} \quad (4.1\text{-}6)$$

$Z_3$ has a similar expression and is not shown here. From (4.1-6) it can be seen that the expected values of $Z_2$. Hence, the mean for all the ISI terms are zero. The variance of $Z_2$ can be calculated as follows:

$$\begin{aligned} \sigma_{Z_2}^2 &= E\left\{\left(\alpha_{k,1}\right)^2\right\} \sum_{j=1}^{N_T} \sum_{\substack{l=-\infty \\ l \neq k}}^{\infty} E\left\{\left(\alpha_{l,j}\right)^2\right\} E\left\{\left(\cos\left(\theta'_{l,j}\right)\right)^2\right\} E\left\{\left(b_{l,j}\right)^2\right\} E\left\{\left(g_{k-l,j}\right)^2\right\} \\ &= \Omega_{k,1} \sum_{j=1}^{N_T} \sum_{\substack{l=-\infty \\ l \neq k}}^{\infty} \Omega_{l,j} \frac{1}{2} \frac{1}{\tau} \int_{lT}^{lT+\tau} g^2(-t) dt = \left( \sum_{i=1}^{N_m} \overline{\gamma}_i \right) \sum_{j=1}^{N_T} \sum_{\substack{l=-\infty \\ l \neq k}}^{\infty} \Omega_{l,j} \frac{1}{2} \frac{1}{\tau} \int_{lT}^{lT+\tau} g^2(-t) dt \end{aligned} \quad (4.1\text{-}7)$$

Similarly the variance of $Z_3$ can also be computed. Adding the variances computed for noise term, $Z_2$ and $Z_3$ the SINR at the receiver for randomized space-time block coding scheme can be computed as

$$SINR = \frac{\left( E\left\{ \sum_{m=1}^{2} \alpha_{k,m}^2 \right\} \right)^2}{\sigma_{Z_2}^2 + \sigma_{Z_3}^2 + \sigma_\eta^2} = \frac{\left( \sum_{i=1}^{N_T} \overline{\gamma}_i \right)^2}{\sigma_{Z_2}^2 + \sigma_{Z_3}^2 + \sigma_\eta^2} \quad (4.1\text{-}8)$$

Based on the SINR derived above we next show the range improvement achieved by describing an example. It is assumed that the nodes transmit with equal power so that the average channel SNR experienced on each link is the same. The carrier frequency $f_c = 2GHz$ , transmission bandwidth is considered to be BW = 10 MHz. A node transmits with a power level $P_T$=-10 dBm. To achieve a minimum SNR= 10 dB at the receiver with a receiver noise figure of 6 dB, the signal power required at the receiver is $P_R$=-88 dBm. Using Friis path loss model $P_R = P_T \frac{G_1 G_2 \lambda^2}{16\pi^2 r^2}$ and assuming $G_1$=3 dB, $G_2$=3 dB, the achievable range for a single node is $y$ = 189 m. By substituting the SINR in path loss formula as $P_T$=-10 dBm + SINR, one can now calculate the improvement in range achieved. The results in terms of SINR improvement due to diversity and corresponding improvement in range are shown in Figure 4.1-1 and Figure 4.1-2. From the figures it can be seen that for a given timing error the SINR saturates after a certain number of nodes also limiting the improvement in range. This is due to the presence of ISI which does not allow a linear increase in SINR. It is observed that when the timing error is limited to 20% of the symbol duration, an maximum SINR improvement of 9 dB is achieved and a 2.6x improvement in range with a minimum of 50 nodes. For timing error greater than 50%, the SINR is less than 10 dB and hence achieves a range less than a perfectly synchronized SISO system.

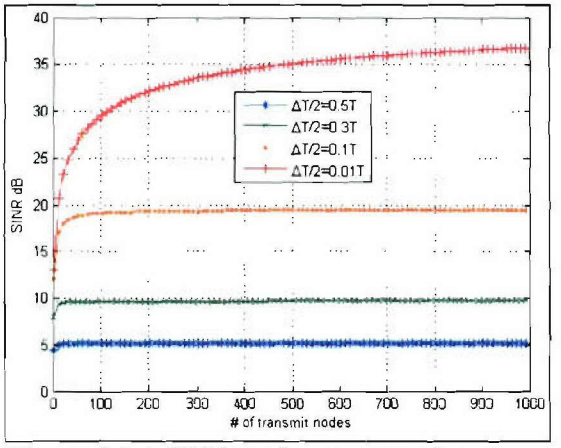



**Figure 4.1-1** SINR performance as the number of cooperating transmitter nodes is increased.

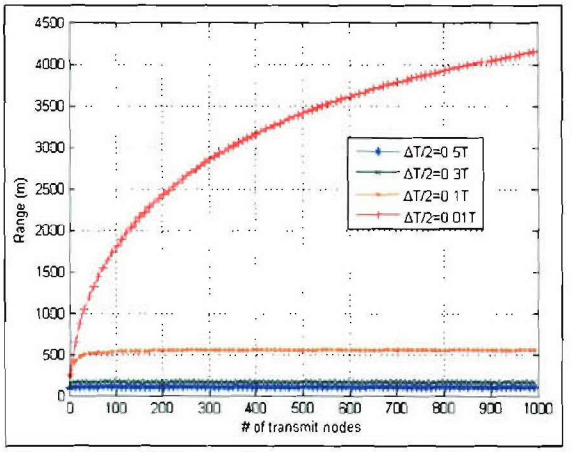



**Figure 4.1-2** Range improvement as the number of cooperating transmitter nodes is increased.

References

[1] B. Sirkeci-Mergen, A. Scaglione, "Randomized distributed space-time coding for cooperative communication in self organized networks," IEEE SPAWC, pp. 500 – 504, June 2005.

[2] J.N. Laneman, and G.W. Wornell, "Distributed space-time-coded protocols for exploiting cooperative diversity in wireless networks," IEEE Trans Inform. Theory, vol. 49, no. 10, pp. 2415 – 2425, Oct. 2003.

[3] Shuguang Cui, A.J. Goldsmith, A. Bahai, "Energy-efficiency of MIMO and cooperative MIMO techniques in sensor networks," IEEE JSAC, vol. 22, pp.1089 – 1098, Aug. 2004.

[4] P.A. Anghel, M. Kaveh, "Exact symbol error probability of a Cooperative network in a Rayleigh-fading environment," IEEE Trans. Wireless Commun, vol. 3, pp. 1416 – 1421 Sept. 2004.

[5] A. Ribeiro, X. Cai, G.B. Giannakis, "Symbol Error Probabilities for General Cooperative Links," IEEE Trans. Wireless Commun., vol. 4, pp. 1264 – 1273, May 2005.

[6] S. Jagannathan, H. Aghajan, A. Goldsmith, "The effect of time synchronization errors on the performance of cooperative MISO systems," IEEE GlobeCom, pp.102 - 107, Nov 2004.

[7] R. Chembil Palat, A. Annamalai, J.H. Reed, "Upper bound on bit error rate for time synchronization errors in bandlimited distributed MIMO networks," IEEE WCNC, proceedings, Apr 2006.

Schedule:

- January-Summer 2005
  - Develop UWB MIMO Algorithms
  - Summer-Fall 2005
  - Simulate performance of UWB MIMO Algorithms
- Spring 2006
  - Begin Work on testing algorithms on Advanced SDR Reciver

Personnel:

Ramesh C. Palat

## 4.2 TIP #2 Close-in UWB wireless application to Sea Basing

Task objective: The objective of this subtask is to develop algorithms that allow UWB technology to provide precision position location, precision ranging, and imaging. With a low duty cycle and wide bandwidth, UWB is naturally suitable to radar and ranging applications. As the time duration of a pulse decreases, it provides finer resolution of reflected signals, such that the system can resolve distances with sub-centimeter accuracy using simple signal processing algorithms.

Accomplishments during reporting period: After last quarter's successful demo a second demo is being considered. This second demo aims to address a different problem with a different kind of crane. The second crane is a horizontally moving crane on parallel tracks as shown in Figure 4.2-1.

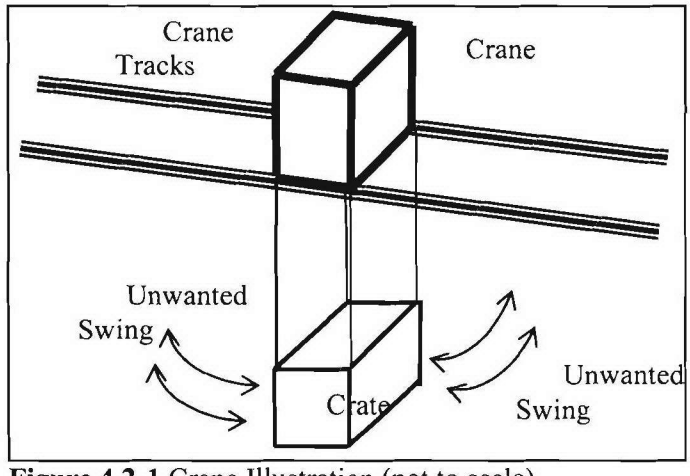



**Figure 4.2-1** Crane Illustration (not to scale).

As the crane moves the crate which is hanging below sways back and forth. The crate's oscillation is unwanted because of the danger that it might hit something, and because the operator cannot unload the crate unless it is fully still. An automatic crane controller can eliminate the sway if the exact position of the crate is known. Therefore, an electronic system needs to be designed to estimate the location of the crate. An initial idea is to have transmitters on the top of the crate and receivers on the bottom of the crane. The receivers will obtain ranging information from the known transmitting points and by mathematically manipulating the ranging information to obtain the location of the crate (Figure 4.2-2). The transmitters can be replaced by transceivers that will transmit after receiving a trigger signal from a transmitter on the crane system.

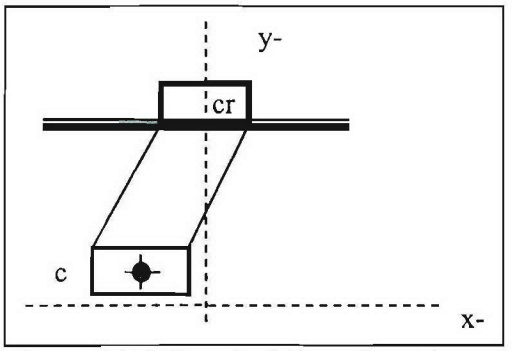


**Figure 4.2-2** Required Crane Location

The major swaying occurs along the direction of the track, and any sway that happens in the other direction (perpendicular to the tracks) for the time being it is assumed to be negligible.

*Proposed Demonstration Setup*

It is desired to have an initial demonstration for a proof of concept. The equipment that are currently available are a two Channel Digital Signal Oscilloscope (Tektronix CSA8000B) and a 30ps Pulser made by Geozandas. A setup with a transmit point and two receive points can be made with the available equipment. The flexibility of the movements will be determined by the antennas used for this demo. If common available large UWB antennas are used the ability of the system to estimate the position can be demonstrated but the motions might be limited.

*Operation Description*

Again, it is assumed that the crate moves only in one plane. A transmitter is placed on the crate that will send an UWB pulse. There will be two receiving positions on the crane. From the time needed for the signal to travel from the transmitting position to the receiving positions the distance between each of the receiving positions to the transmitting point will be estimated. Then the exact position of the transmitting point will be estimated by simple trigonometry. In an operational system the transmitter can be replaced with a transceiver that will send the pulse when signaled. More transceivers and receivers can be added for additional accuracy and 3D information.

*Transmit Location Estimation*

This section describes demonstrates how the transmit location can be estimated by knowing the location of the two receive points and their distances from the transmit location as illustrated in Figure 4.2-3 below.

Let

r1: The distance from Rx1 to Tx
r2: The distance from Rx2 to Tx
d: The distance between Rx1 and Rx2
$\vartheta$: The angle between the line Rx1-Rx2 and the line Rx1-Tx

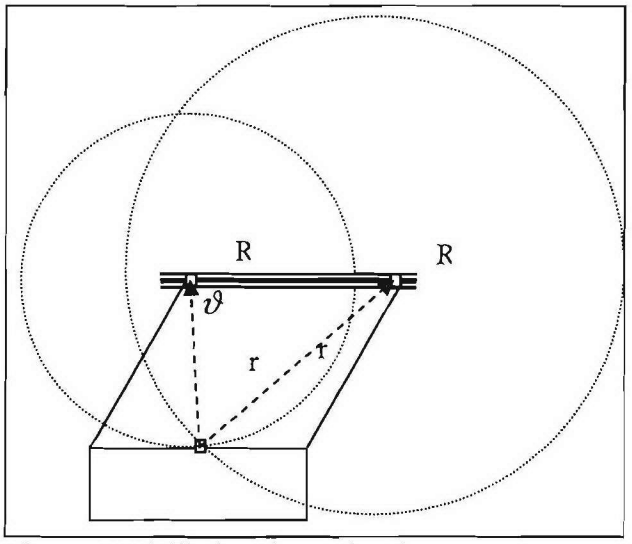



**Figure 4.2-3** Tx location estimation.

Then, it can be shown that the Tx coordinates are given by the following equations:

$$a = \frac{r_1^2 - r_2^2 + d^2}{2d}$$

$$\vartheta = \arccos\left(\frac{a}{r_1}\right)$$

$$x_{tx} = x_{Rx_1} + r_1 \cos(\vartheta)$$

$$y_{tx} = y_{Rx_1} - r_1 \sin(\vartheta)$$

*Future Development*

The first demo will determine how much accuracy and movement flexibility is required. That will help in determining if existing available antennas can be used or if it is desired to obtain new antennas are needed for a demo.

## 4.3 TIP #3: Secure Ad Hoc Networks

### *4.3.1 Project Description*

The testing and demonstration of secure ad hoc networks involves integration and testing along three related tracks. Each of these will lead to a separate demonstration (or coupled set of demonstrations) using a common hardware and software base, as implemented in our test bed network (see discussion of Task 2.1).

(a) Activities within Task 2.1 (Ad Hoc Networks) that support core network services will be integrated, tested, and demonstrated. Capabilities to be integrated include policy-based quality of service (QoS), security based on distributed certificate authorities (DCAs) for key management and trust grading, and mobile ad hoc network (MANET) routing support for QoS and security functionality and as a means to demonstrate cross-layer design. Cross-layer design techniques from Task 2.4 will be reviewed and incorporated as appropriate. Capabilities will be shown operating with Internet Protocol version 4 (IPv4) and, where feasible within the level of effort possible, Internet Protocol version 6 (IPv6).

(b) A cross-layer approach to transporting multiple description (MD) video in ad hoc networks, also a part of Task 2.1, will be integrated, tested, and demonstrated. This task will utilize application-level routing to use application-specific optimal routes. It will integrate with the MANET routing effort of Task 2.1, e.g., with Open Shortest Path First-Multiple Connected Dominating Sets (OSPF-MCDS), to utilize the topology information efficiently obtained by the MANET routing protocol.

(c) We will integrate real-time middleware from Task 2.2 with the combined QoS, security, and routing as discussed above and as investigated in Task 2.3. Specifically, we will investigate and develop methods and mechanisms to integrate policy-based quality of service (QoS) capabilities at the network level, and perhaps at the link layer, with real-time services offered by middleware.

### *4.3.2 Demonstration Description*

Table 4.3-1 lists the themes, components, and leaders for the three demonstrations. Demonstration (a) focuses on core network services. Demonstration (b) involves network support for a video application. Demonstration (c) relates directly to Task 2.3 and involves the integration of network services with an application based on the time-utility function real-time middleware. We will adjust plans based on results from related tasks.

The components of the different demonstrations listed in Table 4.3-1 are currently envisioned to be the same except for the application – or application plus middleware in the case of Demonstration (b) – being supported. The security, QoS, and routing components are discussed further in this report in association with Task 2.1. Note that OSPF-MCDS-MC or, more simply, OMM, is a multi-channel version of the Open Shortest Path First with Minimum Connected Dominating Sets (OSPF-MCDS) MANET routing protocol. OLSR-MC is a multi-channel version of the Optimized Link State Routing (OLSR) MANET routing protocol. The topology viewer (TopoView) and topology emulation tools are carried over from the previous NAVCIITI

project but have been modified to support new functions in the network and to work in an IPv6 environment as described in Subsection 2.1(f). It is envisioned that additional performance monitoring and configuration control tools will be developed as part of Subtask 2.1(e) and used in the demonstrations.

**Table 4.3-1** Demonstration Components and Leaders for the Three Demonstrations

| Demonstration | Key Components | Leaders |
|---|---|---|
| a) Core network services | • Security and key management system<br>• Policy-based quality of service<br>• OSPF-MCDS-MC and/or OLSR-MC routing<br>• TopoView network monitoring<br>• Performance monitoring tools<br>• Topology emulation | • Scott Midkiff<br>• Luiz DaSilva |
| b) Cross-layer approach to MD video routing | • OSPF-MCDS and/or OLSR routing<br>• TopoView network monitoring<br>• Performance monitoring tools<br>• Topology emulation | • Tom Hou<br>• Scott Midkiff |
| c) Real-time middleware in an ad hoc network | • Real-time middleware<br>• Security and key management system<br>• Policy-based quality of service<br>• OSPF-MCDS-MC and/or OLSR-MC routing<br>• TopoView network monitoring<br>• Performance monitoring tools<br>• Topology emulation | • Scott Midkiff<br>• Luiz DaSilva<br>• Binoy Ravindran |

### *4.3.3 Cooperative AWINN Elements*

This test and demonstration requires the inputs from AWINN tasks as specified in Table 4.3-2.

**Table 4.3-2** Inputs from Cooperative AWINN Elements

| Task (Subtask) | Inputs |
|---|---|
| 2.1(a) | Prototype implementation of a policy-based QoS scheme |
| 2.1(b) | Prototype implementation of MANET security and key management scheme |
| 2.1(c) | Optimized prototype implementation of a MANET routing, specifically OSPF-MCDS-MC and/or OLSR-MC |
| 2.1(f) | Performance monitoring tools; enhanced TopoView; enhanced topology emulation |
| 2.1(d) | Video sensor application and test bed components |
| 2.2 | Real-time middleware |
| 2.4 | Cross-layer optimization elements that can be integrated into the test bed for testing and demonstration purposes. |

### *4.3.4 Cooperative Non-AWINN Elements*

At this time, no non-AWINN components are required (except for tools and equipment carried over from the NAVCIITI project).

### *4.3.5 Schedule of Activities*

A general schedule listing major milestones is provided in Table 4.3-3. Note that the schedule is divided into four phases. The emphasis of Phase I was on core network services of Demonstration (a) running with IPv4 and, as much as possible, with IPv6. During Phase II, the emphasis was on core network services of Demonstration (a) running with both IPv4 and IPv6. Both Phases I and II have been completed and were successfully demonstrated on December 8, 2005. During Phase III, the emphasis was on the initial integration of the MD video and real-time applications of Demonstrations (b) and (c), respectively. In Phase IV, the emphasis is on final demonstration of the MD video and real-time applications of Demonstrations (b) and (c), respectively.

**Table 4.3-3** Schedule of Activities

| ***Activity*** | ***Date*** |
|---|---|
| Phase I: Demonstrate core services using IPv4 | 4Q2005 |
| Phase II: Demonstrate core services using IPv6 | 4Q2005 |
| Phase III (b): Initial MD video integration | 1Q2006 |
| Phase III (c): Initial real-time middleware integration | 1Q2006 |
| Phase IV (b): Final demonstration of MD video | 2Q2006 |
| Phase IV (c): Final demonstration of real-time middleware | 2Q2006 |

## 4.4 TIP #4 Integration of Close-in UWB wireless with ESM crane for Sea Basing applications

Task Objective: The goal of this task is to demonstrate the usefulness of UWB in close-in communications, ship-to-ship cargo transfer for sea-basing operations, and cargo transfer from ship-to-shore and vice versa.

Organization: This task is managed by Dr. A. H. Nayfeh

Dr. A.H. Nayfeh, Faculty

N.A. Nayfeh, GRA

Accomplishments During Reporting Period: Having fielded the VT controller on a full-scale container crane at the Jeddah Port in Saudi Arabia, extensive coordination activities with the TIP#2 team have positioned us to demonstrate the usefulness of UWB systems for container cranes. Once the UWB set up for container cranes is ready, we will demonstrate it on our 1/10 scale model of a 65-ton crane shown in Figure 4.4-1.



**Figure 4.4-1** The VT 1/10 scale model of a 65-ton container crane.

*Importance/Relevance*

The proposed work has the potential of being very useful to the Navy's Transformational Sea-Basing System. The success of Sea Basing depends on the ability to sustain logistic operations with significantly reduced reliance on land bases. This requires the development of a high capacity, high reliability at-sea capability to transfer fuel, cargo, vehicle, and personnel in rough seas while underway from commercial container ships to large sea basing ships and then to smaller ships. The wave-induced motion of the crane ship can produce large pendulations of the cargo being hoisted and cause the operations to be suspended.

Personnel:

N.A. Nayfeh, January, 2005-present

## 5. FINANCIAL REPORT

